AD-A066 577   AIR FORCE ROCKET PROPULSION LAB EDWARDS AFB CALIF   F/G 21/9.2

AN ANALYSIS OF CLIP STRAIN GAGE/SOLID PROPELLANT INTERACTION.(U)

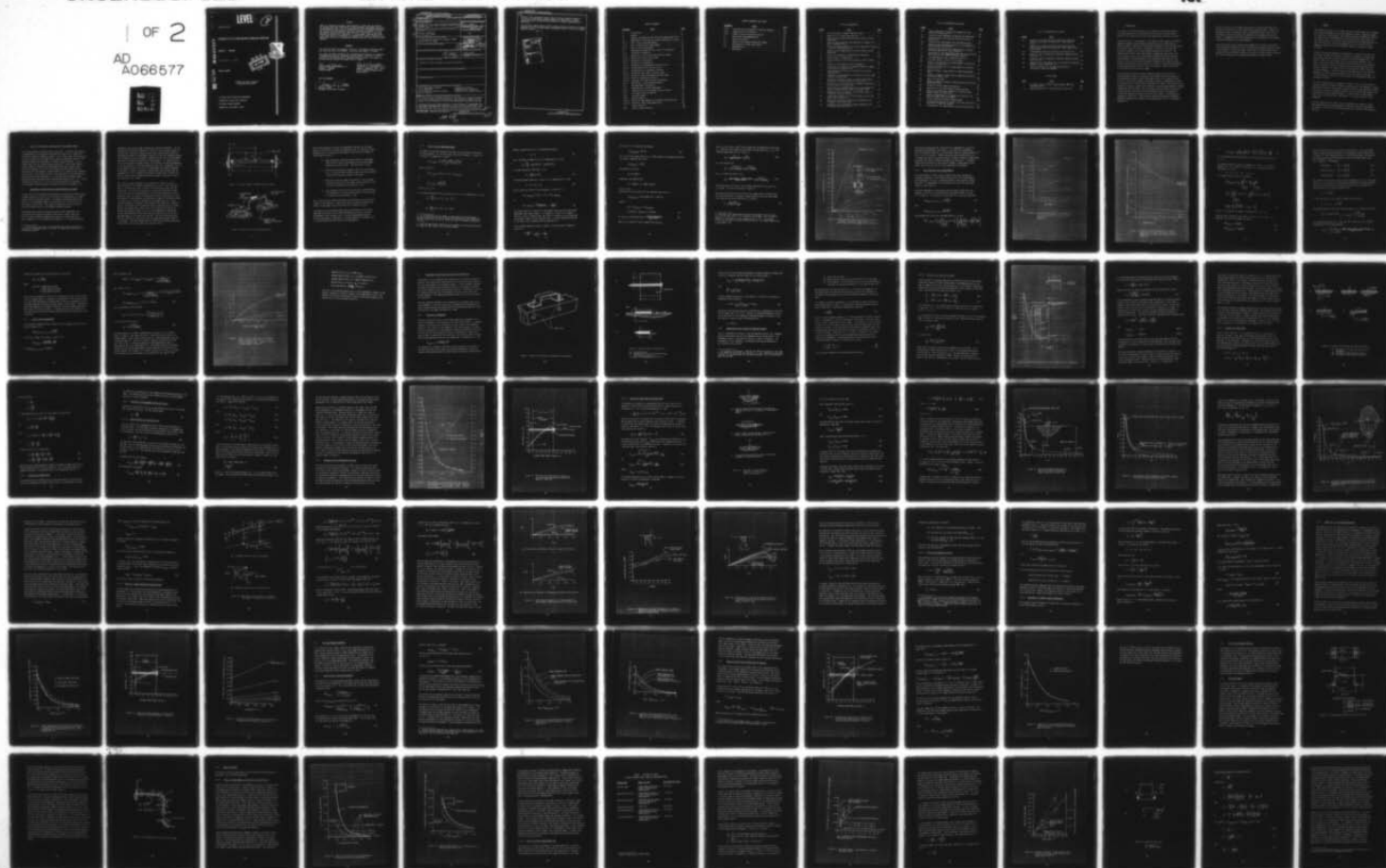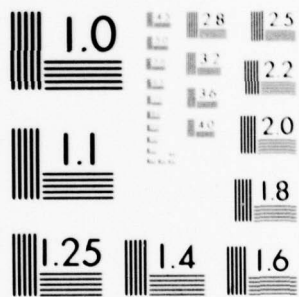OCT 78   D I THRASHER

UNCLASSIFIED   AFRPL-TR-77-22   NL

1 OF 2

AD
A066577

MICROCOPY RESOLUTION TEST CHART

NATIONAL BUREAU OF STANDARDS 1963 A

LEVEL

AFRPL-TR-77-22

AN ANALYSIS OF CLIP STRAIN GAGE/SOLID PROPELLANT INTERACTION

DURWOOD I. THRASHER

OCTOBER 1978

SPECIAL REPORT

DDC
MAR 30 1979
C

APPROVED FOR PUBLIC RELEASE;
DISTRIBUTION UNLIMITED

AIR FORCE ROCKET PROPULSION LABORATORY

DIRECTOR OF SCIENCE AND TECHNOLOGY

AIR FORCE SYSTEMS COMMAND
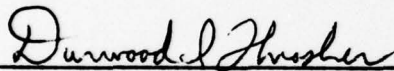
EDWARDS AFB, CALIFORNIA 93523

NOTICES

"When U.S. Government drawings, specifications, or other data are used for any purpose other than a definitely related government procurement operation, the Government thereby incurs no responsibility nor any obligation whatsoever, and the fact that the Government may have formulated, furnished, or in any way supplied the said drawings, specifications or other data, is not to be regarded by implication or otherwise, or in any manner licensing the holder or any other person or corporation, or conveying any rights or permission to manufacture, use or sell any patented invention that may in any way be related thereto."

FOREWORD

This Technical Report was prepared by the Air Force Rocket Propulsion Laboratory under Job Order No. 573013GL. The author was Durwood I. Thrasher.

This report has been reviewed by the Information Office/XOJ and is releasable to the National Technical Information Service (NTIS). At NTIS it will be available to the general public, including foreign nations. This report is unclassified and suitable for general public release.

DURWOOD I. THRASHER
Project Manager

ROBERT R. MIDDLETON, CAPT., USAF
Chief, Mechanical Behavior and
Aging Section

FOR THE COMMANDER

CHARLES R. COOKE
Director, Solid Rocket Division

REPORT DOCUMENTATION PAGE		READ INSTRUCTIONS BEFORE COMPLETING FORM
1. REPORT NUMBER AFRPL-TR-77-22	2. GOVT ACCESSION NO.	3. RECIPIENT'S CATALOG NUMBER
4. TITLE (and Subtitle) AN ANALYSIS OF CLIP STRAIN GAGE/SOLID PROPELLANT INTERACTION		5. TYPE OF REPORT & PERIOD COVERED Special Report
		6. PERFORMING ORG. REPORT NUMBER
7. AUTHOR(s) Durwood I. Thrasher		8. CONTRACT OR GRANT NUMBER(s) N/A
9. PERFORMING ORGANIZATION NAME AND ADDRESS Air Force Rocket Propulsion Laboratory (MKPB) Edwards AFB, CA 93523		10. PROGRAM ELEMENT, PROJECT, TASK AREA & WORK UNIT NUMBERS Program Element 62302F Project 5730, Task 13 JON: 573013GL
11. CONTROLLING OFFICE NAME AND ADDRESS		12. REPORT DATE OCTOBER 1978
		13. NUMBER OF PAGES 123
14. MONITORING AGENCY NAME & ADDRESS(if different from Controlling Office)	126p.	15. SECURITY CLASS. (of this report) Unclassified
		15a. DECLASSIFICATION/DOWNGRADING SCHEDULE

16. DISTRIBUTION STATEMENT (of this Report)

Approved for public release; distribution unlimited.

17. DISTRIBUTION STATEMENT (of the abstract entered in Block 20, if different from Report)

18. SUPPLEMENTARY NOTES

19. KEY WORDS (Continue on reverse side if necessary and identify by block number)

Strain Measurement Accuracy
Clip Strain Gage
Solid Propellant Mechanical Behavior
Elastic Analysis
Viscoelastic Analysis
Gage/Propellant Interaction
TEXGAP-3D Finite Element Analysis

20. ABSTRACT (Continue on reverse side if necessary and identify by block number)

This report covers a detailed analysis of the mechanical interaction between a clip strain gage and a solid propellant uniaxial tensile sample, and the effects of this interaction on the strain measurement provided by the gage.

Prototype clip strain gages developed by Thiokol/Huntsville under AFRPL contract F04611-76-C-0041 were analyzed and found to produce significant strain measurement bias (original prototype 16 percent bias at 500 psi propellant

DD FORM 1473 EDITION OF 1 NOV 65 IS OBSOLETE
1 JAN 73

modulus, final prototype 6 percent bias at 500 psi propellant modulus).
Possible clip gage design changes (geometry and materials) to reduce
measurement bias are discussed and potentially feasible approaches are
identified.

The analytical models used are shown to agree closely with 3D finite element
analyses and also with experimental measurements made by Thiokol on a gaged
propellant sample.

ACCESSION for

NTIS	White Section
BDC	Buff Section
UNANNOUNCED	
JUSTIFICATION	

BY
DISTRIBUTION/AVAILABILITY CODES

Dist.	AVAIL and/or SPECIAL
A	

TABLE OF CONTENTS

TABLE OF CONTENTS (Continued)

LIST OF ILLUSTRATIONS

LIST OF ILLUSTRATIONS (Continued)

LIST OF TABLES

1.   INTRODUCTION.

This report is a detailed analysis of the mechanical interaction between a
clip strain gage and a solid propellant uniaxial tensile sample and the
effects of this interaction on the strain measurement provided by the gage.

The analysis was first undertaken in the summer of 1976 to assess an apparent
potential technical problem which was then developing on AFRPL Contract
F04611-76-C-0041, "Improved Solid Propellant Mechanical Properties Measurement
for Structural Analysis Input" (hereinafter referred to as the Improved
Properties program), with Thiokol Corporation/Huntsville Division.   The
planned testing effort under that program included high rate tensile tests
with a closed, liquid-filled pressurization chamber enclosing the sample.
A key mechanical response parameter to be determined from these tests was
Poisson's ratio; the contractor intended to determine this property, under
dynamic pressurization and straining of the sample, from separate measurements
of axial and transverse strain in the test specimens.   These strains were
to be measured using clip strain gages.

Believing the fabrication of highly compliant gages to be a relatively
straightforward problem, the contractor had planned no detailed analysis of
the measurement problem to define acceptable values for the gage stiffness.
As the Air Force Project Manager, the author decided to independently analyze
the problem so that criteria would be available if needed.   The results of this
rudimentary analysis, together with laboratory tests of gaged propellant samples
conducted by the contractor, led to the mutual conclusion that the high pre-
cision required for Poisson's ratio determination could not be achieved
(within the resources available) with clip strain cages.   The approach was
abandoned at that point.   (The contractor eventually devised an acceptable
alternate technique for Poisson's ratio determination, which is discussed in
Reference 1.)

-6-

The early analysis results agreed qualitatively with the gaged sample test results, but substantially over-predicted the measurement bias. Some of the assumptions used in the analysis were re-examined and found to be in error. The analysis was corrected and close agreement was obtained with the test results. A comparison with check problems using the TEXGAP-3D finite element code also confirmed the revised assumptions.

Since the results of this analysis were judged to be of value to the solid rocket propulsion community at large, the decision was made to publish a report. In the process of writing the report, many areas of further analysis were pursued, both to strengthen the basic structure of the analysis and to explore the overall propellant strain measurement problem in greater detail.

2.   SUMMARY.

The analyses described in this report provide an overall model for the mechani-
cal interaction between a clip strain gage and a uniaxial propellant sample
of a particular configuration. The interaction analysis separately considers
the effects due to "beam deformation" of the propellant sample under the
clip gage resisting force and the local deformation of the gage mounting pins
under the same force. These two components of the interaction are then
combined to determine the net interaction effects as a function of gage
stiffness.

Typical clip gage configurations are analyzed in a parametric fashion, and
the effects of gage design factors (geometry and materials) on gage output
and (through the gage stiffness) on relative strain measurement bias. The
analysis shows that the original Thiokol prototype gage produces a very
large strain bias (roughly 16 percent of the applied strain at a propellant
modulus of 500 psi) and that the final Thiokol prototype gage shows a sub-
stantial improvement (to about 6 percent of the applied strain at 500 psi
propellant modulus). Since this level of measurement bias is not desirable,
approaches to reducing the measurement bias are discussed and analyzed. It
is shown that major reductions in bias (without sacrificing gage output) are
potentially feasible.

The elastic analyses used to accomplish the above results is then extended to
include viscoelastic propellant behavior, obtaining the time dependent clip gage
response to a series of step strain increments applied to the propellant sample.
These results are shown to compare extremely well with actual measurements made
by Thiokol on a gaged propellant sample. A limited study of gage response
under strain cycling and short time effects of clip gage prestrain is also
presented.

The final conclusions are that clip gage improvements are needed to reduce
measurement bias due to gage-propellant interaction, that such improvements
are possible, and that the interaction problem can be analyzed with acceptable
accuracy.

3.   ANALYSIS OF MECHANICAL CONTRIBUTIONS TO MEASUREMENT ERROR.

This section comprises the main body of the report. The major contributions
to measurement error produced by the mechanical behavior of a system con-
sisting of a uniaxial propellant sample , a clip strain gage, and the mounting
pins which connect the clip gage to the sample are analyzed in detail. The
analyses reported here developed in a rather unplanned fashion. It was
evident that the first simple analyses (section 3.1, which treats the pro-
pellant sample as a beam with a superimposed axial load, and 3.4, which
consists of analyses of the clip strain gage structural behavior and its
interaction with the sample as characterized in 3.1) ignored a very important
souce of error. This source of error, local deflection of the mounting pins,
was therefore analyzed separately in 3.2 and the combined effects (beam
deformation plus local deflection) were obtained as described in 3.3. Finally,
the elastic analyses of 3.1, 3.2, and 3.3 were modified to incorporate
time-dependent propellant modulus to produce the results discussed in 3.5.

3.1   Gage-Sample Interaction Due to Beam Deformation of Sample.

The analyses in this subsection were conducted to estimate the direct effects
of gage stiffness on the bias[1] of strain and force measurements on a gaged
uniaxial tensile propellant sample. The sample configuration used in the
analysis is an end-bonded sample, 4 inches long, with a 1/2-inch by 1/2-
inch square cross section. This sample configuration is the one used for
high rate uniaxial tests in the Improved Properties program.

The analyses which follow are based on simple elastic beam theory and
include all the assumptions thereof (plane sections remain plane, etc.).
By far the most important assumption, of course, is linear elasticity.
While propellant is not a linear elastic material, it is often successfully

---

1. In this context, zero bias in attained when the stress and strain dis-
tributions in the gaged sample are identical to those which would occur if
the gage were absent.

treated as such by using "quasi-viscoelastic" analysis procedures. For the purposes of the present investigation, the use of elastic theory appears to be justified. The elastic modulus values used in the analyses should be considered as effective instantaneous values of either the relaxation modulus or the constant strain rate modulus, depending on the test being considered; both types of loading are planned for these samples. It is obvious that a linear elastic analysis cannot account for any effects of modulus dependence on strain; therefore, since most propellants show strain dependence, the use of the analysis results to correct for measurement bias would be somewhat questionable. However, the analysis should become more accurate when the perturbations to the "ungaged" sample behavior become small; therefore the analysis results can be reasonably applied to specify conditions for controlling bias to low levels.

The structural model analyzed in this subsection is shown in Figure 1. While the ends of the propellant specimen are not truly fixed, the fixed ends of the model more nearly simulate the true end constraints than do pinned ends. The effect of the loads P is statically equivalent to that of two loads of the same magnitude acting at the sample centerline (axial load) plus a pair of moments of opposing directions of magnitude $M_o = Ph/2$. (The effect of load application at some height e above the surface, as shown in Figure 2, is to increase the moments by an amount $\Delta M_o = Pe$.) These forces and moments are assumed to be uniformly distributed over transverse sections of the beam which include the points of application of the loads P, so that simple beam theory can be used. This assumption introduces an unknown (but hopefully small) error, since the gage/sample interactions involve local deformations near the mounting surface as well as the average deformations of the beam cross sections. The local deformations become less important as the area of the clip gage mounting pads (Figure 2) is increased. (The local deflections for a different mounting system using straight pins piercing the sample are analyzed in 3.2).

-10-
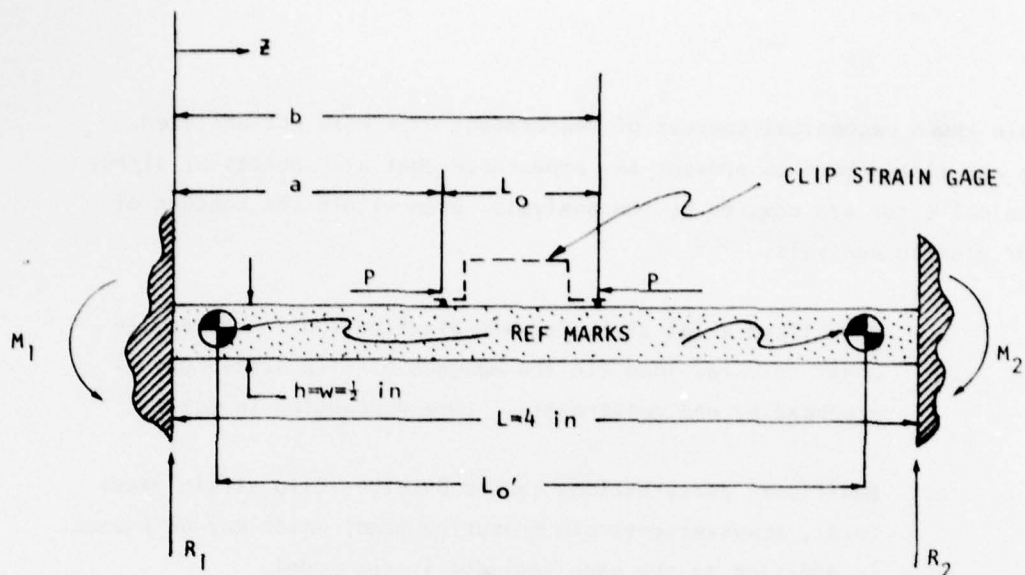
Figure 1. Structural Model of Gaged Propellant Sample
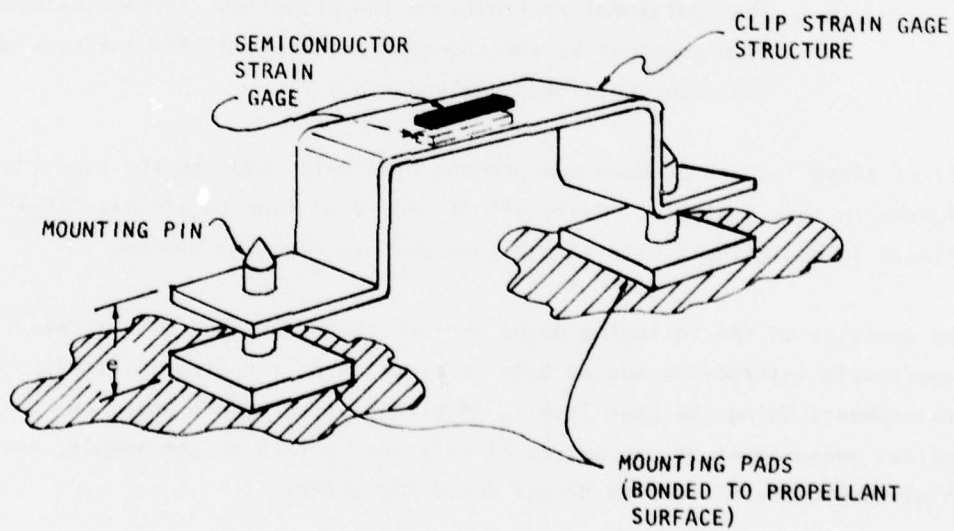
Figure 2. Details of Clip Strain Gage Mounting

Certain known mechanical sources of measurement bias were not analyzed.
These are listed here to prevent any appearance that all sources of direct
mechanical error are covered by the analysis, even within the context of
linear elastic analysis:

a. Nonuniform axial stress/strain distribution in the sample
    under uniaxial load (in the absence of clip strain gages)
    produced by end constraints. (See discussion in 3.5.)

b. Additional perturbations caused by other clip strain gages
    (e.g., transverse-strain measuring gage) which may be present
    in addition to the gage included in the model.

c. Deviations from the assumed distribution of the clip gage
    restraining force across the sample surface (except for the
    straight pin mounting system analyzed in 3.2).

d. The additional restraint on the propellant surface deforma-
    tion produced by the mounting pads (except for the straight
    pin mounting system analyzed in 3.2).

All of these factors produce measurement bias which adds to the bias con-
sidered in this analysis. Every effort should be made to minimize their
effects in designing a clip strain gage and its mounting system.

The analyses on the following pages explore the effects of clip strain
gage/sample interaction due to beam deformation on the bias in strain
measurements using the gage itself, in strain measurements based on
optical measurement of the motion of reference points on the sample, and
in stresses determined from direct force measurements.

-12-

3.1.1   Bias in Strain Gage Measurement.

The effects of the axial load and the moment will be considered separately and then combined. For the axial load, the stress[2] between $z = a$ and $z = b$ in Figure 2 is (Reference 1, p. 82):

$$(\Delta\sigma_z)_{\text{axial}} = \frac{P}{A}\left(\frac{\ell/2 - L_o/2}{\ell/2}\right) = \frac{P}{A}\left(\frac{P-L_o}{\ell}\right) \tag{1}$$

and the strain[2] is

$$(\Delta\epsilon_z)_{\text{axial}} = \frac{1}{E}(\Delta\sigma_z + \nu\Delta\sigma_x + \nu\Delta\sigma_y)_{\text{axial}}$$

or

$$(\Delta\epsilon_z)_{\text{axial}} = \frac{P}{AE}\left(\frac{\ell-L_o}{\ell}\right) \tag{2}$$

since $\Delta\sigma_x = \Delta\sigma_y = 0$.

For the applied moments[3], the reaction force at $z = 0$ is (Reference 2, p. 113):

$$R_1 = \frac{-6M_o}{\ell^3}[(a\ell - a^2) - (b\ell - b^2)]$$

or

$$R_1 = \frac{-3Ph}{\ell^3}[(a\ell - a^2) - (b\ell - b^2)].$$

---

2. It is understood that the sample is under some yet-to-be-determined stress and strain as a result of the applied deformation at the sample ends and that these stress and strain values are additive components produced by P and M_o.

3. Note that beam-column interactions are ignored in the ensuing disccusion. The impact of this omission has not been examined.

-13-

However, substitution of $b = \ell - a$ produces the result

$$R_1 \equiv 0 \qquad (3)$$

Also, the reaction moment at $z = 0$ is (Reference 2, p. 113):

$$M_1 = \frac{-M_o}{\ell^2} \left[(4\ell a - 3a^2 - \ell^2) - (4\ell b - 3b^2 - \ell^2) \right]$$

or, substituting $M_o = Ph/2$ and $b = \ell - a$,

$$M_1 = \frac{-Ph}{2\ell^2} \left[2\ell a - \ell^2 \right]. \qquad (4)$$

The bending moment between $z = a$ and $z = b$ is (Reference 2, p. 113):

$$M = -M_1 + R_1 z + M_o \qquad (5)$$

and the resulting flexural strain between $z = a$ and $z = b$ is

$$(\Delta\epsilon_z)_{bending} = \frac{1}{E} (\Delta\sigma_z + \nu\Delta\sigma_x + \nu\Delta\sigma_y)_{bending}$$

so

$$(\Delta\epsilon_z)_{bending} = \frac{(\Delta\sigma_z)_{bending}}{E} = \frac{M(h/2)}{EI}. \qquad (6)$$

The actual quantity of interest is the average strain over the strain gage measurement base (gage length), i.e. between $z = a$ and $z = b$. However, since R_1 is zero in Equation (5), the strain is constant in this region and the average is equal to this constant value. A similar observation applies to the axial strain component given by Equation (2).

For the sample dimensions given in Figure 1, the cross section moment of inertia is

$$I = \frac{(h)h^3}{12} = \frac{1}{12(2)^4} = \frac{1}{192}$$

-14-

and, with h = 1/2, Equation (6) becomes

$$(\Delta\epsilon_z)_{bending} = 48 \ M/E. \tag{6a}$$

For a clip strain gage length of $L_o = 0.400$ inches and the sample dimensions of Figure 1, Equation (2) yields

$$(\Delta\epsilon_z)_{axial} = 3.60 \ \frac{P}{E}$$

and Equation (4) yields

$$M_1 = +0.0250 \ P.$$

Therefore, from Equation (5),

$$M = -0.0250 \ P + 0 + \frac{Ph}{2} = 0.2250 \ P$$

since h = 0.5.

Substitution of this value of M into Equation (6a) results in

$$(\Delta\epsilon_z)_{bending} = 48 \ (0.2250) \ P/E = 10.80 \ P/E.$$

Finally,

$$\Delta\epsilon_z = (\Delta\epsilon_z)_{axial} + (\Delta\epsilon_z)_{bending}$$

$$= 3.60 \ P/E + 10.80 \ P/E = 14.40 \ P/E \tag{7}$$

$$\text{or} \ (\Delta\epsilon_x)/\epsilon_o = (14.40 \ P_o)/(\epsilon_o E) = \frac{\text{strain attenuation}}{\text{gage strain}} \tag{8}$$

where ϵ_o is a specific value of gage strain ($\Delta L_o/L_o$)

-15-

and P_o is the reaction force[4] at each gage foot corresponding to the strain ε_o. Since the local sample strain without the gage would be $\varepsilon_o + \Delta\varepsilon_z$, the relative measurement bias for strain is

$$e_{R\varepsilon} = \frac{-\Delta\varepsilon_z}{\text{sample strain}} = \frac{-\Delta\varepsilon_z}{\varepsilon_o + \Delta\varepsilon_z} \tag{9a}$$

or, from Equation (8),

$$e_{R\varepsilon} = \frac{-14.40\ P_o/E}{\varepsilon_o + 14.40\ P_o/E} = \frac{-14.40\ P_o}{E\varepsilon_o + 14.40\ P_o}.$$

For $\varepsilon_o = 0.040$ in/0.400 in $= 0.1$,

$$e_{R\varepsilon} = \frac{\text{gage strain} - \text{sample strain}}{\text{sample strain}} = \frac{-14.40\ P_o}{0.1\ E + 14.40\ P_o} \tag{9b}$$

Calculations were carried out for different combinations of P_o and E for $L_o = 0.400$. The results are shown in Figure 3.

The above calculations were carried out for a gage length of 0.400 inches. To examine the effects of changes in gage length on the strain measurement bias, Equation (9) can be solved for P_o, yielding

$$P_o = \frac{-e_{R\varepsilon}\ (E\varepsilon_o)}{14.40\ (1 + e_{R\varepsilon})} \tag{10}$$

---

4. Note that if the gage preload (force at zero sample strain) is zero, P_o/ε_o for any gage strain ε_o is a constant for the gage. Zero preload was assumed for the analyses in this subsection and in 3.3. If a preload exists, P_o/ε_o becomes a function of applied strain. This added complication is addressed in 3.5.

-16-
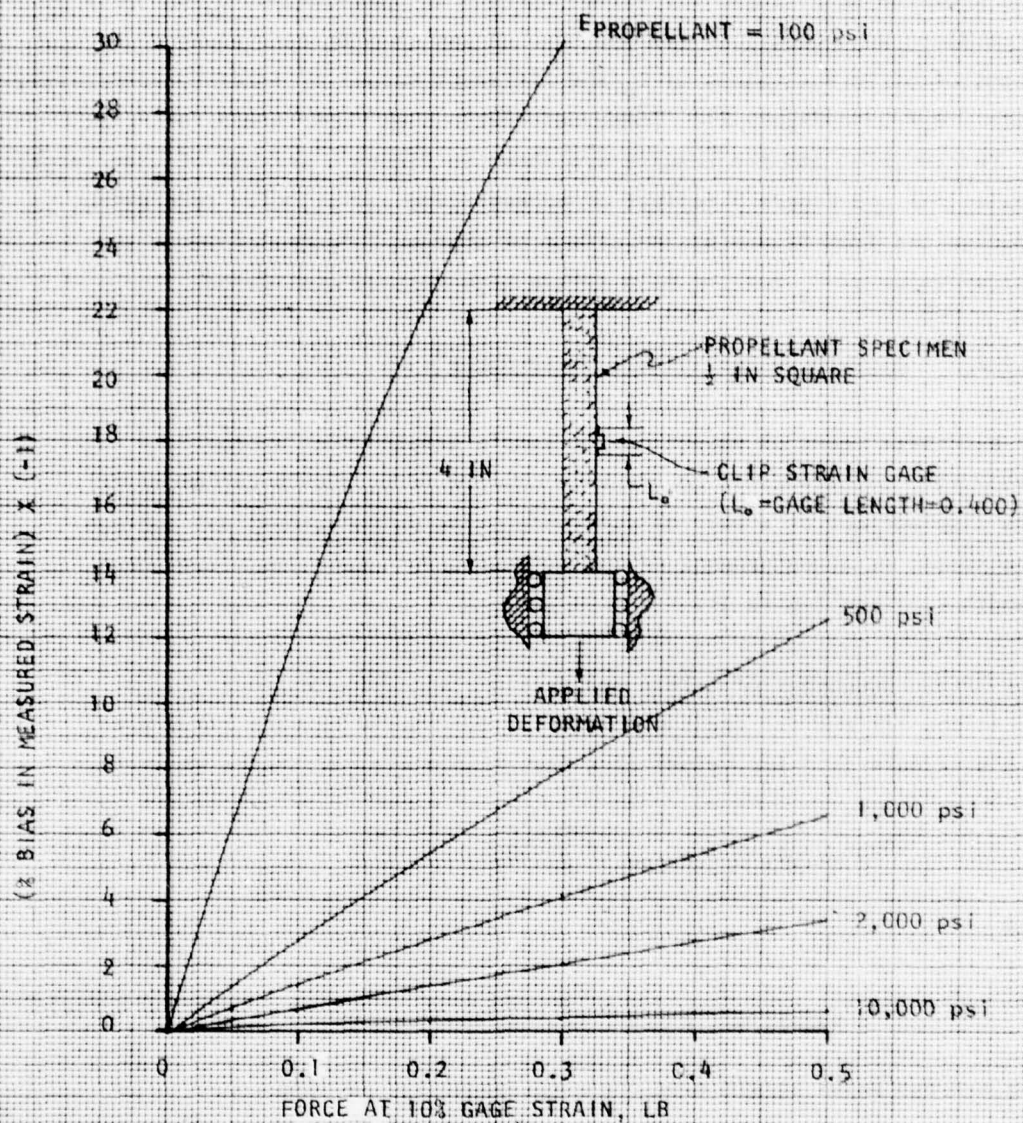
Figure 3. Effect of Strain Gage Resisting Force on Bias in (Strain Gage) Strain Measurement for a Gaged Tensile Specimen (Gage Length = 0.400 in.)

and K can be substituted for 14.40, where K is dependent on L_o and M in accordance with Equations (2) and (6). K can then be re-evaluated in terms of different values of L_o and different values of loading eccentricity (i.e., $e \neq 0$ in Figure 2). These calculations were performed for P_o at -1 percent bias and the results are shown in Figure 4 (effect of gage length variation) and Figure 5 (effect of eccentricity variation). In drawing conclusions from Figure 4, the effect of changes in gage length on the actual value of P_o for the clip strain gage must be considered.

3.1.2   Bias in Optical Strain Measurements.

An alternate means of measuring the sample strain under appropriate laboratory conditions is to visually observe (e.g. with a cathetometer) the displacement of a pair of reference marks on the propellant surface. The result is a measurement of the average strain over the visual gage length L_o' (see Figure 1).

The axial components of stress and strain are given, respectively, by Equations (1) and (2) for the portion of the sample between $z = a$ and $z = b$ (Figure 1). For values of z less than $z = a$, it can be shown that

$$\left(\Delta \sigma_z \right)_{\text{axial, } 0 \leq z \leq a} = \frac{P}{A} \left(\frac{L_o}{\ell} \right). \tag{11}$$

and

$$\left(\Delta \epsilon_z \right)_{\text{axial, } 0 \leq z \leq a} = \frac{P}{AE} \left(\frac{L_o}{\ell} \right). \tag{12}$$

The average axial strain over the gage length L_o' is then

$$\left(\overline{\Delta \epsilon}_z \right)_{\text{axial}} = \frac{2}{L_o'} \int_{\left(\frac{\ell - L_o'}{2} \right)}^{\ell/2} \left(\epsilon_z \right)_{\text{axial}} dz = \frac{2}{L_o'} \left[\int_{\left(\frac{\ell - L_o'}{2} \right)}^{a} \frac{P}{AE} \left(\frac{L_o}{\ell} \right) dz + \int_{a}^{\ell/2} \frac{P}{AE} \left(\frac{L_o}{\ell} \right) dz \right]$$

-18-
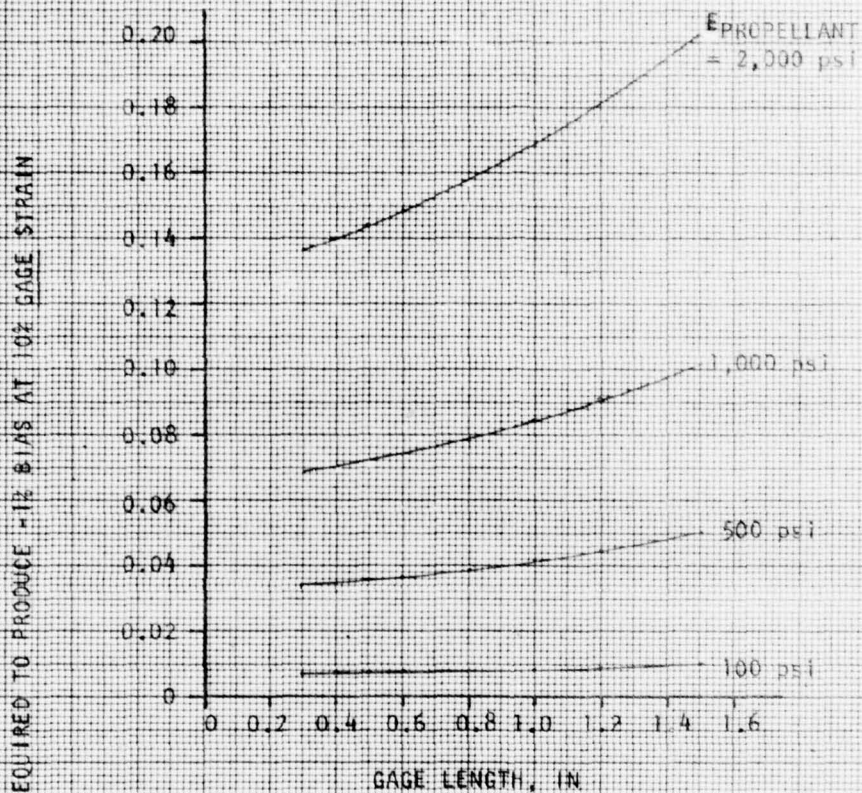
Figure 4. Effect of Gage Length on Force Required to Produce a -1% Bias in (Strain Gage) Measured Strain for a Gaged Tensile Specimen.
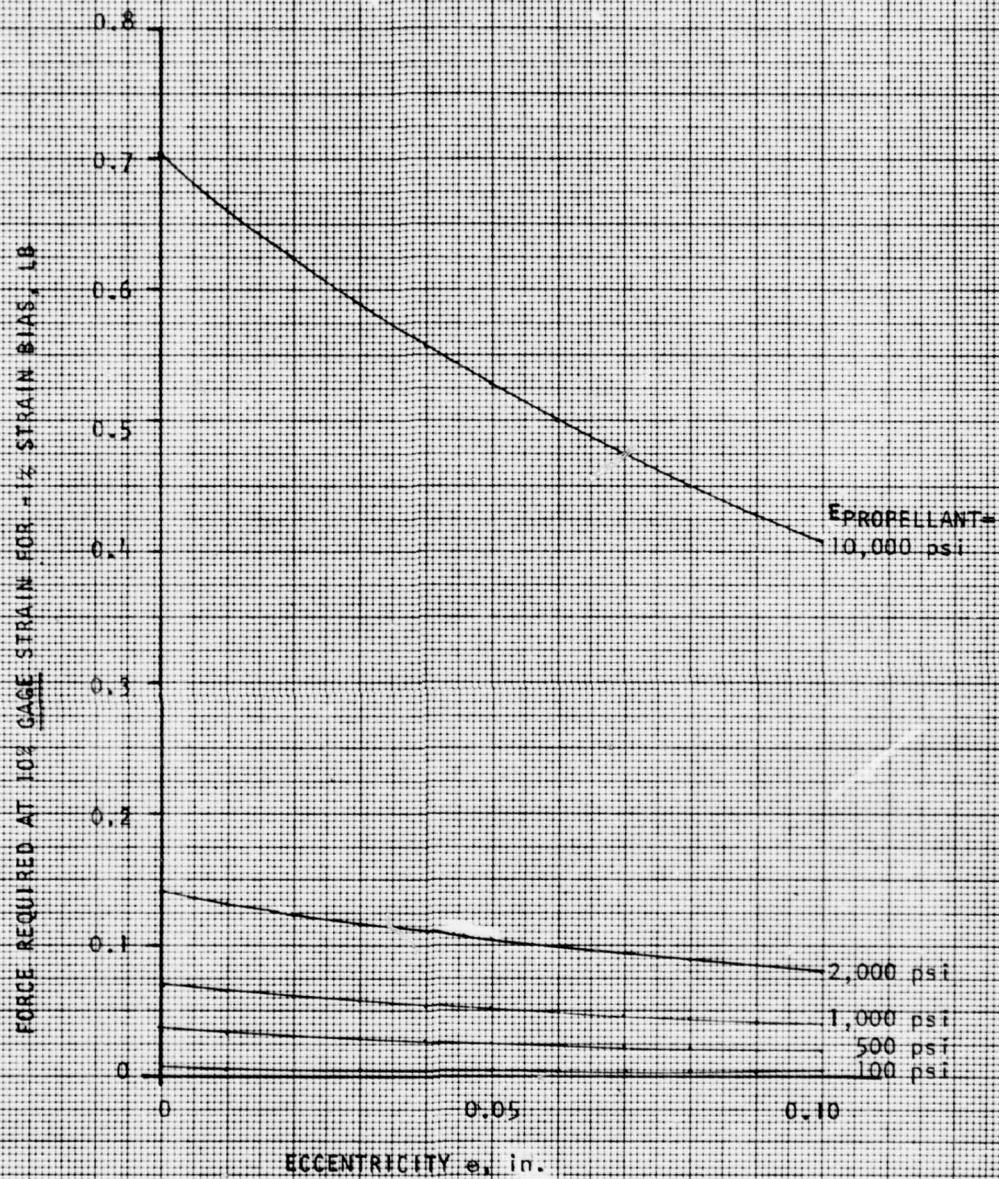
Figure 5. Effect of Loading Eccentricity on Force Required to Produce a -1% Bias in (Strain Gage) Measured Strain for a Gaged Tensile Specimen.

or

$$(\Delta\epsilon_z)_{axial} = \frac{2P}{L_o{}'AE} \left\{ \frac{L_o}{\ell} \left[a - \frac{\ell - L_o{}'}{2} \right] + \left[\frac{\ell - L_o}{\ell} \left(\frac{\ell}{2} - a \right) \right] \right\}. \quad (13)$$

It can be demonstrated that Equation (13) reduces to Equation (12) for $L_o{}' = L_o$.

The bending moment for values of z between $z = a$ and $z = b$ is given by Equation (5). For values of z less than $z = a$, the bending moment is (Reference 2, p. 113):

$$M = -M_1 + R_1 X = -M_1, \quad 0 \le z \le a.$$

The average flexural strain is therefore

$$(\overline{\Delta\epsilon}_z)_{bending} = \frac{2}{L_o{}'} \int_{\left(\frac{\ell - L_o{}'}{2}\right)}^{\ell/2} \frac{Mc}{EI} dz = \frac{2c}{L_o{}'EI} \int_{\left(\frac{\ell - L_o{}'}{2}\right)}^{\ell/2} M dz$$

$$= \frac{2c}{L_o{}'EI} \left[\int_{\left(\frac{\ell - L_o{}'}{2}\right)}^{a} \frac{Ph}{2\ell^2}(2\ell a - \ell^2) \, dz + \int_{a}^{\ell/2} \left[\frac{Ph}{2\ell^2}(2\ell a - \ell^2) + \frac{Ph}{2} \right] dz \right]$$

$$= \frac{C}{EIL_o{}'} \frac{Ph}{\ell^2} \left[\frac{\ell^2(\ell - L_o{}')}{2} + \ell a L_o - \ell^2 a \right] \quad (14)$$

For $L_o{}' = L_o$, Equation 14 reduces to Equation (4) if $c = h/2$.

Substitution of dimensions from Figure (1), with $L_o{}' = 3$ inches, into Equations (13) and (14) produces the results:

$$(\overline{\Delta\epsilon}_z)_{axial} = 0.8267 \frac{P}{E} \quad (15)$$

$$(\overline{\Delta\epsilon}_z)_{bending} = 1.6000 \frac{Pc}{E}. \quad (16)$$

-21-

The most likely values for C are +h/2, 0, and -h/2 (i.e., the top surface, neutral surface, and bottom surface of the specimen as shown, respectively, in Figure 1). Using these values for C, the following results are obtained for the average total surface strain over the 3-inch gage length, where

$$\overline{\Delta\epsilon}_z = (\overline{\Delta\epsilon}_z)_{axial} + (\overline{\Delta\epsilon}_z)_{bending}:$$

Top Surface $\qquad\qquad \overline{\Delta\epsilon}_z = 1.2667 \, \frac{P}{E}$ $\qquad\qquad\qquad$ (17)

Neutral Surface $\qquad\quad \overline{\Delta\epsilon}_z = 0.8267 \, \frac{P}{E}$ $\qquad\qquad\qquad$ (18)

Bottom Surface $\qquad\quad \overline{\Delta\epsilon}_z = 0.4267 \, \frac{P}{E}$. $\qquad\qquad\qquad$ (19)

Now consider the effect of a load P_o which corresponds to a clip strain gage strain ϵ_o. For the specific (strain gage) gage length and sample dimensions used in deriving Equations (17) through (19), the strain attenuation was previously shown to be given by Equation (7):

$$\Delta\epsilon_z = 14.40 \, \frac{P_o}{E}$$

so that the sample strain without the gage present would be

$$\epsilon_o + \Delta\epsilon_z = \epsilon_o + 14.40 \, \frac{P_o}{E} .$$

The strain measurement bias over the gage length $L_o' = 3$ inches is therefore

$$e'_{R\epsilon} = \text{relative bias} \bigg|_{L_o' = 3 \text{ inches}} = \frac{-\overline{\Delta\epsilon}_z}{\epsilon_o + 14.40 \, \frac{P_o}{E}}$$

or, expressing Equations (17), (18), and (19) in the form $\Delta\epsilon_z = K_c \, \frac{P_o}{E}$ and substituting into the above equation,

$$\epsilon'_{R\epsilon} = \frac{K_c \, \frac{P_o}{E}}{\epsilon_o E + 14.40 \, \frac{P_o}{E}} = \frac{\text{gage length strain - sample strain}}{\text{sample strain}} \qquad (20)$$

Comparison of Equation (20) with Equation (9) shows that

$$e'_{R\epsilon} = e_{R\epsilon} \frac{K_c}{14.40} \tag{21}$$

where

$$K_c/14.40 = 0.0880 \text{ (Top Surface)}$$
$$= 0.0574 \text{ (Neutral Surface)}$$
$$= 0.0296 \text{ (Bottom Surface)}$$

Thus the bias introduced in the strain as measured by direct visual observation of the gage length L_o' (because of the presence of the clip strain gage) will vary from 2.96 percent to 8.80 percent of the bias introduced into the clip gage measurements themselves (gage length = 0.400 inches). The specific proportion depends on the location chosen for the optical gage length marks (top, bottom, or neutral surface). It appears that the best location for the marks would be the bottom surface since the least bias would result from that choice.

3.1.3   Bias in Stress Measurement.

The increment in measured stress caused by the clip gage resisting force P is given by Equation (11):

$$(\Delta\sigma_z)_{axial, \; 0 \leq z \leq a} = \frac{P}{A}\left(\frac{L_o}{\ell}\right)$$

or, for $L_o = 0.400$, $\ell = 4$, and $A = (1/2)^2 = 1/4$:

$$(\Delta\sigma_z)_{axial} = 4P\left[\frac{0.400}{4}\right] = \frac{0.400}{P}$$

or $(\Delta\sigma_z)_{axial, \; \epsilon_o = 0.1} = 0.400 \; P_o \tag{22}$

-23-

Now from Equation (9),

$$(\text{sample strain})_{ungaged} = (\varepsilon_z)_{ungaged} = \frac{\varepsilon_o}{1 - \dfrac{14.40\ P_o}{0.1\ E + 14.40\ P_o}}$$

and, since $\sigma_z = E\varepsilon_z$,

$$(\sigma_z)_{ungaged}\bigg|\ \varepsilon_o = 0.1 = \frac{0.1\ E}{1 - \dfrac{14.40\ P_o}{0.1\ E + 14.40\ P_o}} = \frac{0.1\ E\ (0.1\ E + 14.40\ P_o)}{0.1\ E}$$

or

$$(\Delta\sigma_z)_{ungaged}\bigg|\ \varepsilon_o = 0.1 = 0.1\ E + 14.40\ P_o \tag{23}$$

and, using Equations (22) and (23):

$$e_{R\sigma} = \text{relative stress bias} = \frac{(\Delta\sigma_z)_{axial,\ \varepsilon_o = 0.1}}{(\sigma_z)_{ungaged}\bigg|\ \varepsilon_o = 0.1}$$

so the relative stress bias is

$$e_{R\sigma} = \frac{0.400\ P_o}{0.1\ E + 14.40\ P_o}\ . \tag{24}$$

The bias produced by different combinations of P_o and E for $L_o = 0.400$ is shown in Figure 6. Note that this bias in stress (relative to stress in an ungaged sample) is much smaller than the bias in strain measurement using the clip gage (Figure 3). The bias in values of modulus determined from stress and strain values is therefore dominated by (and approximately equal in magnitude to) the strain measurement bias. The modulus based on uncorrected stress and strain measurements would be higher than the true effective propellant modulus; for instance, if $E = 500$ psi and $P_o = 0.1$ lb (at $\varepsilon_o = 0.100$), the following results are obtained, using Equation (7) and Equation (24):

-24-
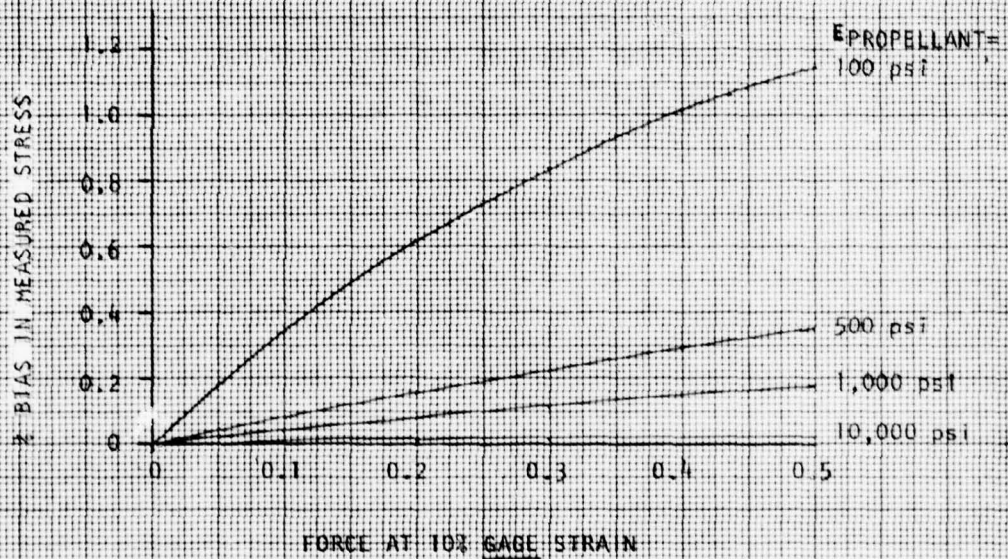
FIGURE 6. Effect of Strain Gage Resisting Force on Bias in Stress Measurement for a Gaged Tensile Specimen (Same Specimen as Figure 5; Gage Length = 0.400 in.)

Measured Strain $= \varepsilon_o = 0.1000$ in/in

Ungaged Sample Strain $= \varepsilon_o + 14.40 \dfrac{P_o}{E} = 0.1029$ in/in

Ungaged Sample Force $= E\varepsilon = (500)(0.1029) = 51.45$ lb

Measured Force $= 51.45 (1 + e_{R\sigma}) = 51.49$ lb

Calculated Modulus $= \dfrac{51.49}{0.1000} = 514.9$ psi.

The bias in the measured modulus value is (514.9-500)/500 = 0.298 or +2.98 percent; inspection of Figure 3 shows a strain measurement bias of -2.8 percent for the specified values of E and P_o, which would produce a +2.9 percent error in the calculated value of E.

3.2   Gage-Sample Interaction Due to Local Pin Deflection.

The analyses in this subsection were undertaken to estimate the added bias caused by local deflections associated with an alternate method of mounting the clip strain gage to the propellant sample. In this alternate approach, the mounting pad/mounting pin system of Figure 2 is replaced by straight steel pins inserted through the propellant sample as illustrated in Figure 7. This mounting technique was of considerable interest, since it was the favored approach in the ongoing contractual effort at the time this analysis was undertaken.

The basic approach followed in this subsection is to consider the pins as beams embedded in a semi-infinite elastic foundation (the propellant) and then to examine whether the deflections thus calculated are additive to the deflections of the sample considered as a beam.

3.2.1   Stiffness of Foundation.

Consider the mounting pins to act as beams supported by (embedded in) an elastic foundation of infinite extent, as shown in Figure 8(b). A necessary parameter for analyzing the deflections of such a beam is the foundation modulus $k = q/w$, where q is the load per linear inch exerted on the foundation by the beam and w is the foundation deformation produced by this load. For the case of a uniform bearing pressure p exerted over a square area having sides of length 2b at the surface of a semi-infinite uniform elastic body, the average deflection over the loaded area is (Reference 2, p. 323)

$$\overline{w}_{semi-inf} = \frac{1.90 \ pb \ (1-\nu^2)}{E}.$$

For the case of a pressure p exerted on a plane surface at the center of an infinite uniform elastic body, an attractive assumption is that the pressure load would be equally divided between the two semi-infinite bodies

-27-

STEEL PINS
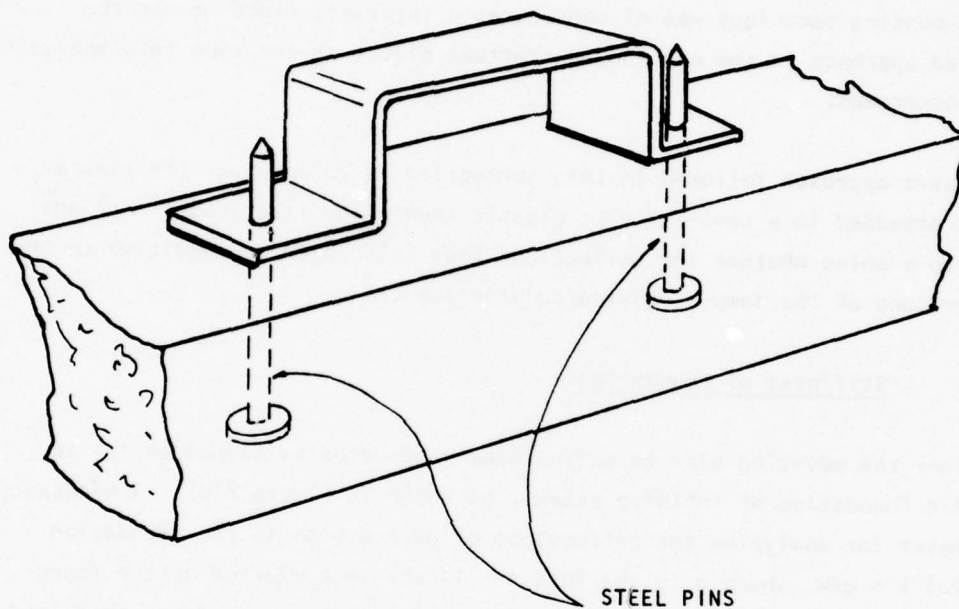
Figure 7.   Details of Alternate Clip Gage Mounting Technique

(a)

(b)

(c)

PROPELLANT

$M = Pe$

P

h

∞

$-x, -\beta x$

$M = Pe$
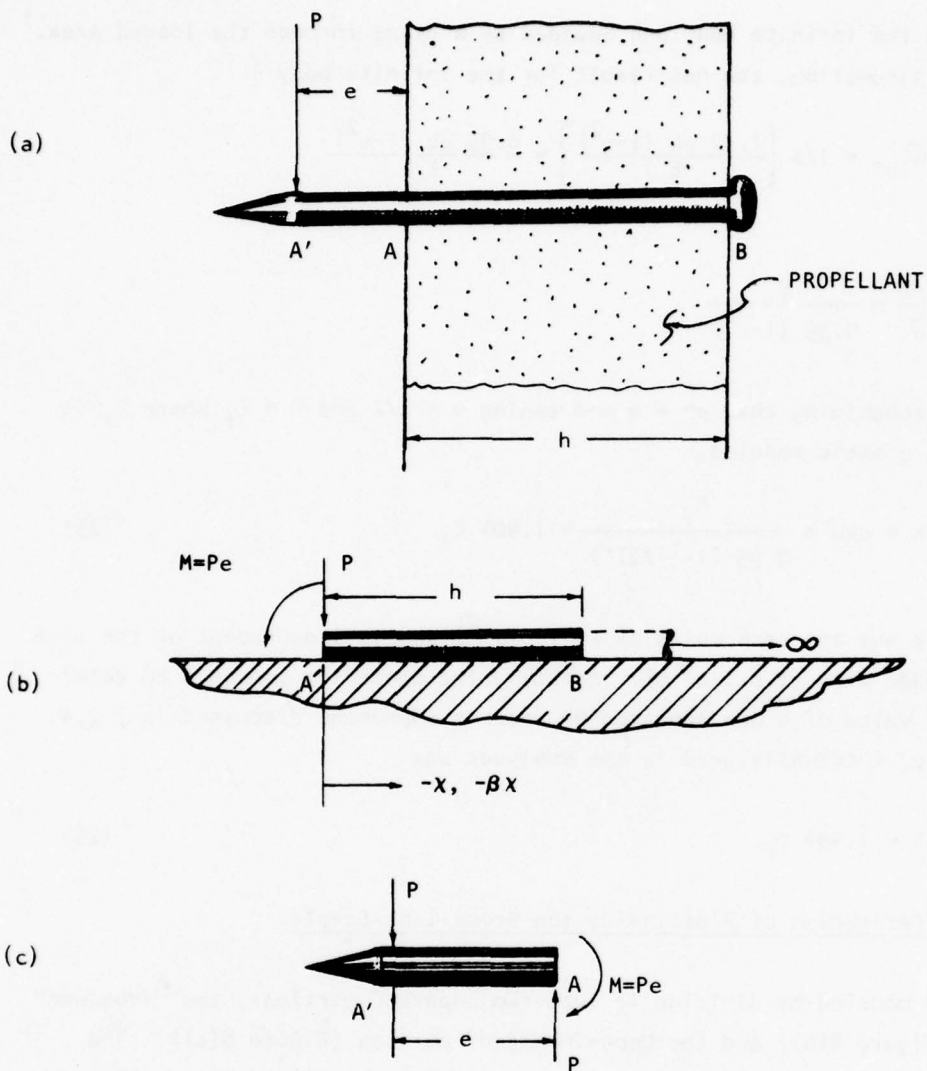
Figure 8. Analysis Model for Mounting Pin:

(a) Actual Situation;
(b) Imbedded Portion of Pin Treated as Beam
    on an Elastic Foundation;
(c) Model of Nonimbedded Portion of Pin

-29-

comprising the infinite body and bounded by a plane through the loaded area.[1]
With this assumption, the net result for the infinite body is

$$\bar{w}_{inf} = 1/2 \left[\frac{1.90 \text{ pb } (1-\nu^2)}{E} \right] = \frac{0.95 \text{ pb } (1-\nu^2)}{E}$$

and

$$\frac{pb}{\bar{w}} = \frac{E}{0.95 (1-\nu^2)}$$

Finally, recognizing that pb = q and taking $\nu = 1/2$ and $E = E_f$ where E_f is
foundation elastic modulus,

$$k = q/\bar{w} = \frac{E_f}{0.95 [1-(1/2)^2]} = 1.404 \; E_f. \tag{25}$$

Note that k has the same units as E_f (lb/in^2) and is independent of the size
of the loaded area (i.e., of b). Actually the preceding approach to deter-
mining the value of k was replaced by another approach, discussed in 3.2.4.
The value of k actually used in the analyses was

$$k = 1.494 \; E_f. \tag{26}$$

3.2.2   Deflection of Pins Inside the Propellant Sample.

The pin is modeled by dividing it into two separate portions, the "imbedded"
portion (Figure 8(b)) and the "non-imbedded" portion (Figure 8(c)). The
"imbedded" portion is analyzed as a beam on an elastic foundation. The
assumptions in this treatment, as discussed by Den Hartog (Reference 5,
pp. 144-145) are as follows:

---

1. As discussed in Reference 3, page 58, the shearing tractions in the plane
of the loaded surface vanish for the case of $\nu = 1/2$. Vanishing of the shear
tractions in this plane makes the indicated assumption valid (see Reference 4,
pages 392 and 399).

-30-

(1) Deflections are small.

(2) Plane sections remain plane under deflection (for the beam).

(3) The foundation's resisting force at a point on the beam depends only upon the transverse deflection of the beam at that point.

Den Hartog points out that assumption (3) is violated by the behavior of a continuous elastic foundation, but states that the excellent agreement of the theory with experience shows that the assumption produces no significant error.

For a beam on an elastic foundation, it is convenient to work with the non-dimensional distance $\beta\chi$ where χ is the physical distance measured along the beam's length and β is defined by (Reference 5, page 143)

$$\beta = \sqrt[4]{\frac{k}{4 \ EI}} \qquad (27)$$

where k is the "foundation modulus," E is the beam material's elastic modulus, and I is the moment of inertia of the beam's cross section. The basic theory treats of semi-infinite and infinite length. If the beam has a finite length h, then if βh is sufficiently large, the semi-infinite theory holds for small values of $\beta\chi$; that is, for the semi-infinite results to accurately model the deflection and slope of the left end of the beam in Figure 8(b), the value of βh must be "large." Conversely, if $\beta\ell$ is "small," the beam will act essentially as a rigid body, with its displacement governed by the resisting forces in the foundation. Den Hartog provides the following criteria for "large" and "small" values of $\beta\ell$ (Reference 5, p. 161).

$$\beta\ell \text{ large: } \beta h > 3 \qquad (28)$$
$$\beta\ell \text{ small: } \beta h < 1. \qquad (29)$$

The two types of behavior are discussed separately below.

-31-

3.2.2.1 Deflection of Semi-Infinite Beam.

Since the load P is actually applied to the portion of the pin that extends beyond the propellant surface (Figure 8(a)), the imbedded portion of the beam is loaded by the force P and the moment M = Pe, as shown in Figure 8(b). Superposing the results given by Den Hartog for P and M treated as individual loads, the deflection and slope at any point χ are

$$\left[\delta_\chi = \frac{2\ \beta P}{k}\ F_4(\beta\chi) + \frac{2\beta^2 M}{k}\ F_3\ (\beta\chi) \right]\Big|_\chi \tag{30}$$

$$\left[\theta_\chi = \frac{2\beta^2 P}{k}\ F_1(\beta\chi) + \frac{4\beta^3}{k}\ MF_4\ (\beta\chi) \right]\Big|_\chi \tag{31}$$

with the values of F_1, F_3, and F_4 given as tabular functions of $\beta\chi$ (Reference 5, page 146). For $\chi = 0$, $\beta\chi = 0$, and, as it turns out, $F_1(\beta\chi) = F_2(\beta\chi) = F_3(\beta\chi) = 1$ at $\beta\chi = 0$.

Let us examine the effect of the gage standoff distance e on the pin's deflected shape. Consider the normalized deflection δ_χ/δ_A. Making the proper substitutions into Equation (30),

$$\frac{\delta_\chi}{\delta_A} = \frac{F_4(\beta\chi) + \frac{\beta M}{P} F_3(\beta\chi)}{1 + \frac{\beta M}{P}}$$

or, since M = Pe,

$$\frac{\delta_\chi}{\delta_A} = \frac{F_4(\beta\chi) + \beta e\ F_3(\beta\chi)}{1 + \beta e} \tag{32}$$

Recall that the beam has thus far been regarded as semi-infinite. It is enlightening to choose the particular value $\chi = h$ and examine the effects of variations in β and e on $(\delta_\chi/\delta_A)\big|_{\chi=h}$. This has been done in Figure 9, utilizing Den Hartog's tabulated F_i values. Before discussing Figure 9, however, some numerical computations are in order. The pins used at Thiokol

-32-
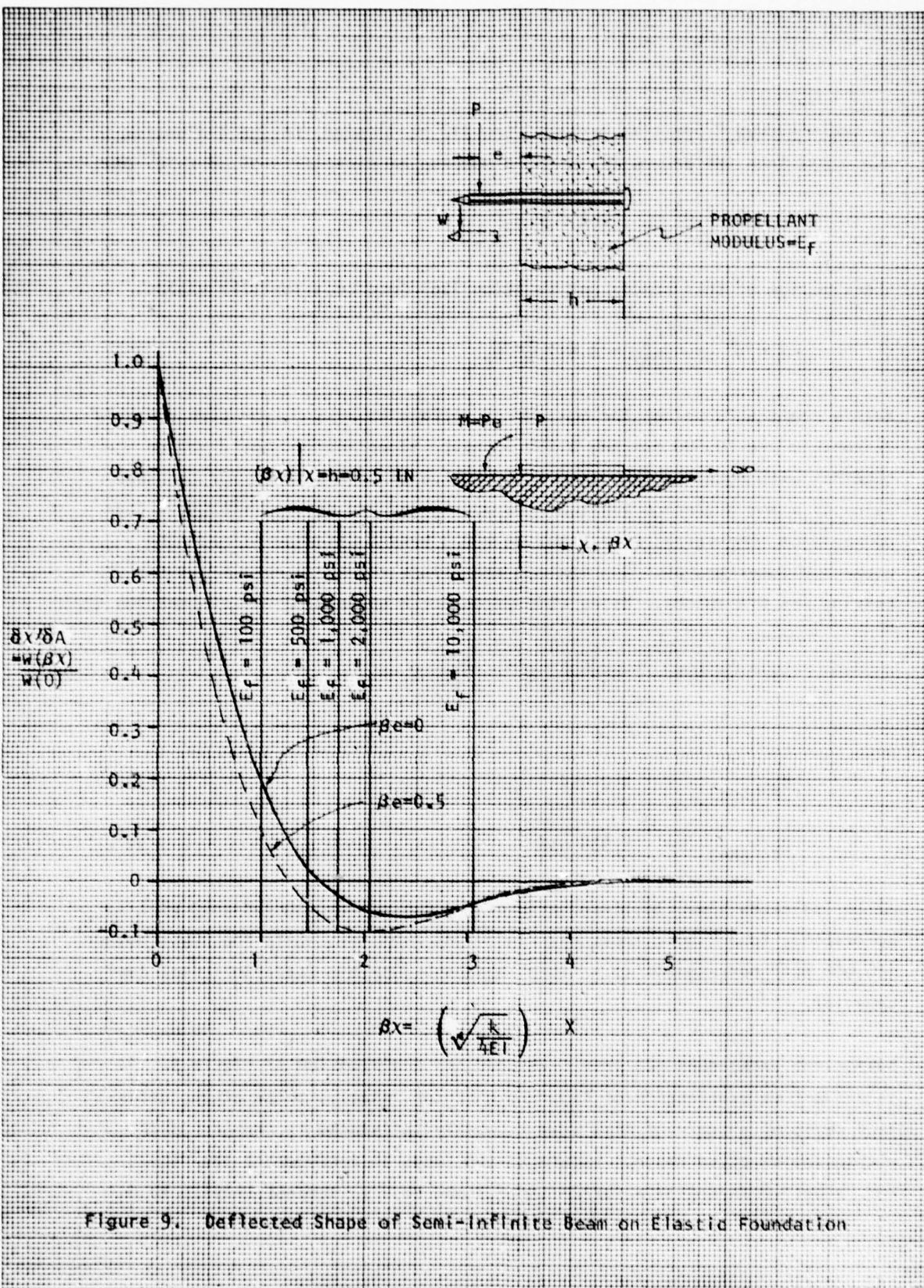
Figure 9. Deflected Shape of Semi-Infinite Beam on Elastic Foundation

in the Improved Properties program were #17 steel pins, having a diameter $d = 0.037$ inch (Reference 6). Using a modulus of elasticity of 28×10^6 psi,

$$EI = E\left(\frac{\pi d^4}{64}\right) = 2.576 \quad \text{lb-in}^2.$$

Substitution of this result and Equation (26) into Equation (27) yields

$$\beta = \sqrt[4]{\frac{1.494 E_f}{4(2.576)}} = 0.617 \sqrt[4]{E_f} \tag{33}$$

Fairly reasonable values for maximum propellant modulus E_f and gage standoff distance e are 10,000 psi and 0.050 inches, respectively. These values together with Equation (33) result in a value of $\beta e = 0.309$. For the same value of e and a minimum limit of the modulus of 100 psi, $\beta e = 0.098$. For convenience, the values $\beta e = 0$ and $\beta e = 0.5$ were considered as absolute upper and lower bounds. The maximum propellant thickness considered for testing was 0.5 inches. Using this value for h and making use of Equation (33),

$$E_f = \left(\frac{\beta}{0.617}\right)^4 = \frac{(\beta h)^4}{(0.617 \ell)^4} = \frac{(\beta h)^4}{(0.309)^4}$$

and

$$E_f \bigg|_{\beta h = 1} = 110 \text{ psi} \tag{34(a)}$$

$$E_f \bigg|_{\beta h = 3} = 8,938 \text{ psi} \tag{34(b)}$$

which indicates that the lower bound of the propellant modulus (100 psi) corresponds to a "short" beam and rigid beam behavior, while the upper bound (10,000 psi) corresponds to a "long" beam and flexible (semi-infinite) beam behavior.

Sufficient background has been developed for a discussion of Figure 9. It is evident on examination of Figure 9 that the relative shape of the deflection curve of a semi-infinite beam is weakly influenced by changes in βe within the expected range. Figure 9 also tends to corroborate the "long" and "short" beam criteria for βh ($\beta h > 3$ and $\beta h < 1$, respectively). In

-34-

particular (following Den Hartog's rationale) for $\beta\chi > 3$, bending deflections (hence bending moment and shear) damp out rapidly, and if the beam were truncated at a point in this region, the bending moments and shear forces thus "destroyed" would have a negligible influence on the beam deflection curve for small values of $\beta\chi$; then the deflection curve of Figure 9 would apply with good accuracy to the finite beam. On the other hand, it is obvious that truncation of the beam at $\beta\chi < 1$ would drastically change the constraints on the left-hand portion of the beam; both bending moment and shear force would be significant in this region. For the latter case, the deflections of the finite beam are dominated by the foundation stiffness rather than the beam stiffness, and the beam itself acts essentially as a rigid body (Reference 5, p. 161).

The foregoing discussion indicates that there are two rather clear-cut regions in $\beta\chi$ for which distinctly different models apply. Unfortunately, the area of interest is the muddy region in between. Den Hartog points out (Reference 5, p. 161) that for this region, "In many practical cases a good approximation is obtained by using either the stiff-beam theory ($\beta h < 1$) or the long-beam theory ($\beta h > 3$) or by interpolating in between." Further discussion of this point is deferred to a later part of this subsection of the report.

3.2.2.2 Deflection of Short Beam.

Since a "short" beam ($\beta h < 1$) is considered to act as a rigid body, its analysis is simple. Given that the foundation obeys Equation (26), the reaction load of the foundation due to a beam deflection at a point is proportional to the deflection. The analysis is most easily done by applying the superposition principle as in Figure 10(a). Static equilibrium equations for the individual free-body diagrams of Figure 10(b) and 10(c) result in the following equations:

$$\Sigma F y = P - q_1 h = P - k\delta_1 = 0$$

$$\Sigma M = M_o - 2 \int_o^{\ell/2} q_2 \left(x - \frac{h}{2}\right) d\left(x - \frac{h}{2}\right) = M_o - \frac{k\delta_2 h^2}{6} = 0$$

-35-
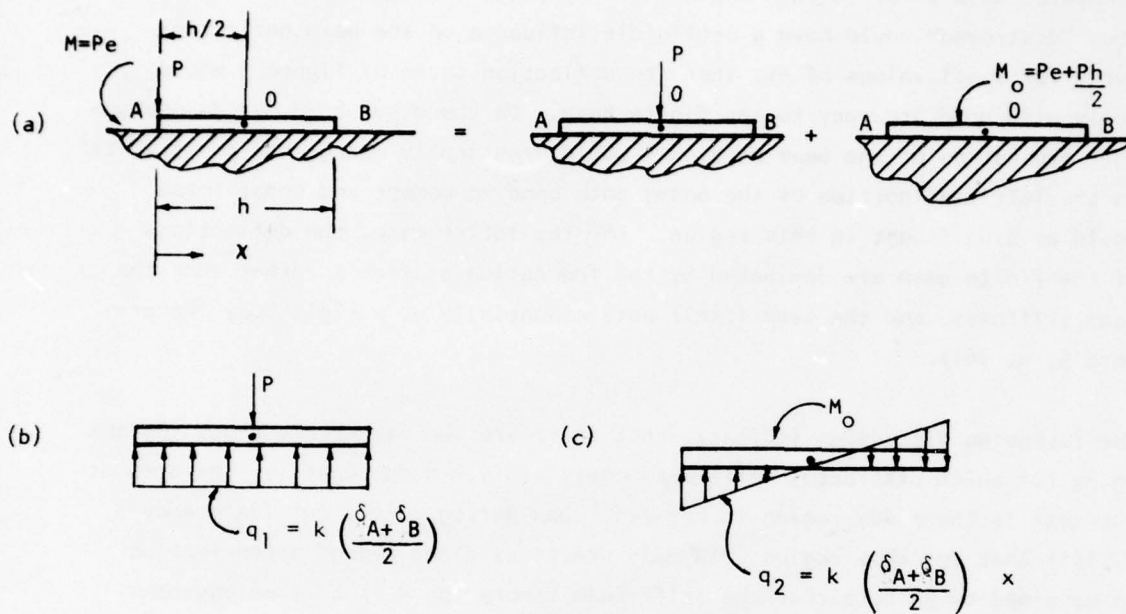
Figure 10. Analysis of Rigid Beam on Elastic Foundation:

    (a) Decomposition of Load into Central Force
          and Moment;
    (b) Free Body for Beam Loaded by Force P;
    (c) Free Body for Beam Loaded by Moment M_o.

-36-

with the results:

$$\delta_1 = \frac{P}{kh}$$

$$\delta_2 = \frac{6\,M_o}{kh^2} \; .$$

If the substitution $M_o = Ph/2 + M$ is now made, the results are

$$\delta_A = \delta_1 + \delta_2 = \frac{P}{kh} + \left(\frac{Ph}{2} + M\right)\left(\frac{6}{kh^2}\right)$$

or

$$\delta_A = \frac{4P}{kh} + \frac{6M}{kh^2}$$

and

$$\theta_A = \text{slope at A} = \frac{\delta 2}{\ell/2} = \frac{2}{h}\left[\frac{Ph}{2} + M\right]\frac{6}{kh^2}$$

or

$$\theta_A = \frac{6P}{kh^2} + \frac{12M}{kh^3}$$

Finally, when $M = Pe$ is substituted,

$$\delta_A = \frac{4P}{kh} + \frac{6Pe}{kh^2} = \frac{P}{kh}\left(4 + \frac{6e}{h}\right) \tag{35}$$

$$\theta_A = \frac{6P}{kh^2} + \frac{12Pe}{kh^3} = \frac{P}{kh}\left(\frac{6}{h} + \frac{12e}{h^2}\right) \tag{36}$$

Notice that the foregoing analysis ignores the effect of beam flexure on the slope and deflection of the pins at point A. This is consistent with the argument discussed in the preceding part of this subsection for $\beta h < 1$.

3.2.3   Deflection of Complete Pin.

The deflections of the complete pin (or more specifically, of certain locations on the complete pin, namely points A and A' in Figure 8(a)) are found

-37-

by combining the deflections of the imbedded and nonimbedded portions of the beam. The imbedded portion has been treated previously; the nonimbedded portion will now be discussed.

3.2.3.1 Deflection of Nonimbedded Portion of the Pin.

Referring to Figure 8(c), let $\delta'_{A'}$ be the deflection at point A' for a beam cantilevered from point A. For the loading shown,

$$\delta'_{A'} = \frac{Pe^2}{2EI} \tag{37}$$

3.2.3.2 Combined Results for the Entire Pin.

In 3.2.3.1 above, the nonimbedded portion of the pin was considered as a cantilever beam. Since the beam is actually connected to the imbedded portion of the pin, the vertical motion (δ_A) and rotation (θ_A) of point A must be incorporated. The final result for the deflection at point A' is

$$\delta_{A'} = \frac{Pe^2}{2EI} + \theta_A\, e + \delta_A \tag{38}$$

For the short (rigid) beam case, δ_A and θ_A are calculated from Equations (35) and (36). For the long beam case, δ_A and θ_A are calculated from Equations (30) and (31) with $\chi = 0$ (as noted earlier, this results in $F_1(\beta\chi) = F_2(\beta\chi) = F_3(\beta\chi) = F_4(\beta\chi) = 1$). The complete results are summarized in Equations (39) and (40):

Long Beam Case ("infinite beam"):

$$\delta_{A'\,inf} = \frac{Pe^2}{2EI} + \left(\frac{2\beta^2 h^2 P}{kh^2} + \frac{4\beta^3 h^2 Pe}{kh^2}\right) e + \left(\frac{2\beta hP}{kh} + \frac{2\beta h^2 Pe}{kh^2}\right) \tag{39}$$

Short Beam Case (rigid beam):

$$\delta_{A'\,rigid} = \frac{Pe^2}{2EI} + \frac{P}{kh}\left(\frac{6}{h} + \frac{12e}{h^2}\right) e + \frac{P}{kh}\left(4 + \frac{6e}{h}\right) \tag{40}$$

-38-

For intermediate cases, i.e., cases for which $1 \leq \beta h \leq 3$, the approach (as mentioned earlier) suggested by Den Hartog is to interpolate between these two results. Applying this advice,

$$\delta_{A'} = K_{\beta h} (\delta_{A'_{inf}} - \delta_{A'_{rigid}}) + \delta_{A'_{rigid}} \qquad (41)$$

Also,

$$\delta_A = K_{\beta h} (\delta_{A_{inf}} - \delta_{A_{rigid}}) + \delta_{A_{rigid}}, \qquad (42)$$

$$\theta_A = K_{\beta h} (\theta_{A_{inf}} - \theta_{A_{rigid}}) + \theta_{A_{rigid}} \qquad (43)$$

and

$$\delta_B = K_{\beta h} (\delta_{B_{inf}} - \delta_{B_{rigid}}) + \delta_{B_{rigid}} \qquad (44)$$

where

$$K_{\beta h} = \begin{cases} 0, & 0 \leq \beta h \leq 1 \\ (\beta h - 1)/2, & 1 < \beta h < 3 \\ 1, & 3 < \beta h \end{cases} \qquad (45)$$

Since the end use of the calculations made according to the above relationships is to determine the net effect on the total strain measurement bias, a useful parameter is the additive component of strain bias in inches/inch per pound of force exerted on the pin by the clip strain gage. Since there are two pins which deflect (at the loading point) through a distance $\delta_{A'}$, the additive bias is given by

$$\frac{\Delta \epsilon}{P} = \text{"DELTA STRAIN BIAS } \div \text{ P"}$$

$$= \frac{2(\delta_{A'})/P}{L_o} \qquad (46)$$

Where L_o is the total distance between pins, i.e., the gage length of the clip gage. (All calculations performed used a fixed value of 0.400 for L_o.)

-39-

The manipulations required to combine Equation (46) with the results of the earlier analyses of sample bending deflection to calculate the total strain measurement bias is deferred until a later subsection of this report.

Appropriate calculations to evaluate Equations (41), (42), (43), and (46) were programmed on a programmable calculator in accordance with the relationships developed above. Selected results (e = 0.050") are shown in Figure 11. It can be seen that the interpolated result for δ_A, transitions very smoothly from the rigid beam result to the infinite beam result as βh goes from 1 to 3. The behavior of this model of the steel pin in the propellant specimen appears, in a general sense, to be quite satisfactory. Figure 12 provides a physical illustration of the pin deflection as described by the model. This figure shows the predicted vertical deformation of the pin treated as a "rigid beam," an "infinite beam," and as an intermediate case ("interpolated result"). As noted on the figure, the particular results shown are for E_f = 1000 psi; the calculated values of βh and βe are, respectively, 1.735 and 0.174. (Actually, the calculator program provides only the deflections at points A and A' and the slopes at point A for the three deflection curves. The remainder of Figure 12 was constructed by interpolating δ/δ_A from Figure 9 for βe = 0.174 to obtain the infinite-body curve, then manually interpolating between this curve and the rigid-body "curve" for βh = 1.735.) The basis of Den Hartog's discussion of the effects of removing the part of the beam which lies outside the foundation (see 3.2.2.1) is clearly evident in Figure 12.

3.2.4   Re-examination of Foundation Stiffness.

The earlier discussion of foundation stiffness (3.2.2) cited a very simple expression for the foundation stiffness. This subsection concerns itself with several factors which were examined in detail to obtain a final estimate of the effective foundation stiffness (a particularly important factor being the interference between two opposed points or distributed loads acting within the medium or foundation). This subsection also examines the manner in which the sample bending deformation and the localized deformations of the pin and surrounding propellant interact to produce the total motion of the pin.
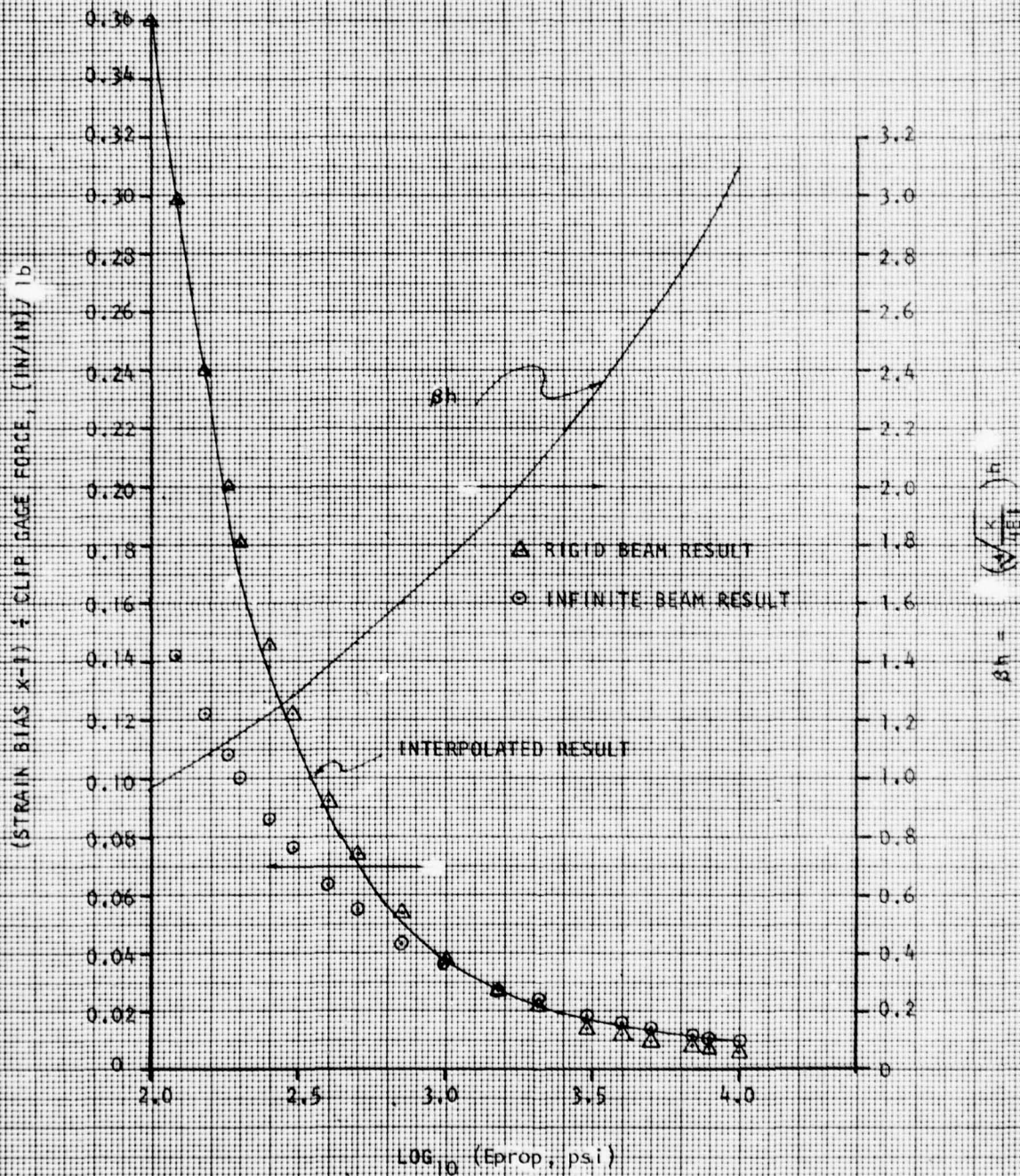
-40-

Figure 11. Strain Bias as a Function of Propellant Modulus
Produced by Deflection of Mounting Pins (Eccentri-
city = 0.050 in.; Gage Length = 0.400 in; Sample
Bending Ignored.)

-41-
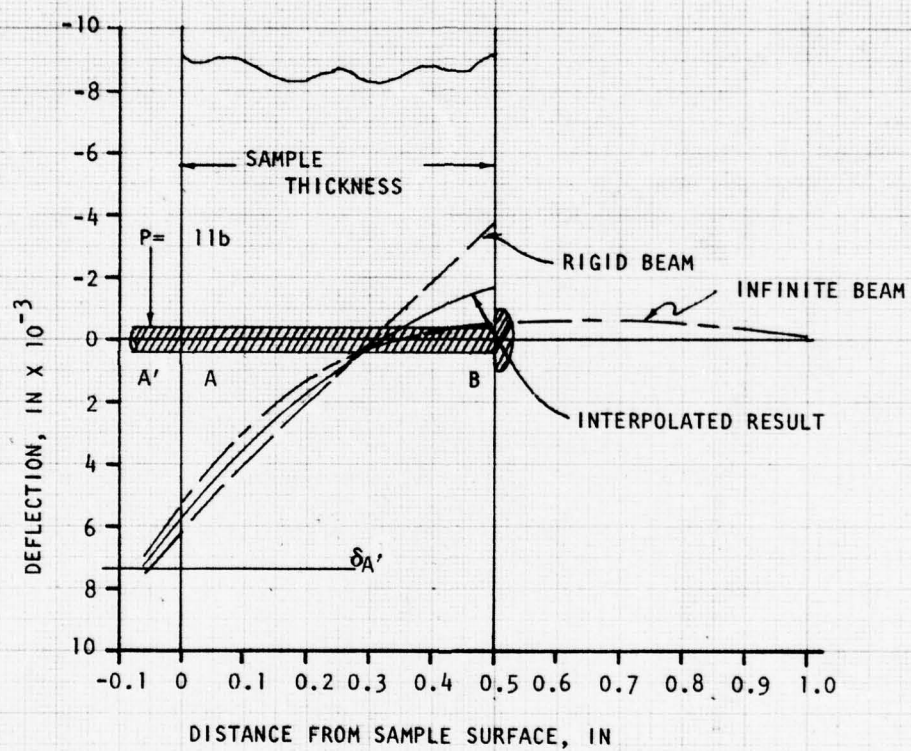
Figure 12. Predicted Total Deflection of Mounting
Pins Ignoring Sample Bending (Propellant
Modulus = 1000 psi).

3.2.4.1 Deflection Under Highly Localized Loads.

The deflection, produced by a concentrated (point) load P acting at the surface of a semi-infinite medium, which exists at a particular point in the medium (r, z, θ) is given by (Reference 4, p. 402):

$$w = \frac{P}{2\pi E_f} \left[(1 + \nu) \, z^2 \, (r^2 + z^2)^{-3/2} + 2 \, (1 - \nu^2)(r^2 + z^2)^{-1/2} \right] \quad (47)$$

where the force acts in the positive z direction at the origin of coordinates and the medium has an elastic modulus E and a Poisson's ratio ν. Consider the deflection (see Figure 13(a)) of a point on a hemispherical surface of radius a, centered at $r = z = 0$. For Poisson's ratio = 0.5, it can be shown that Equation (47) results in

$$w \bigg|_{surf} = \frac{1.5 \, P}{2\pi E_f} \left[\frac{1}{a} (\cos^2 \theta + 1) \right] \quad (48)$$

Two quantities are of interest: $\overline{w} \big|_{surf}$ or the deflection averaged over the hemispherical surface; and $\overline{w} \big|_{arc}$ or the deflection averaged over an arc in a plane perpendicular to the hemisphere's base. Integration of Equation (48) (with the proper substitutions) results in

$$\overline{w} \bigg|_{surf} = \frac{\int_0^{\pi/2} \int_0^{2\pi} w \big|_{surf} \, a d\phi d\theta}{2\pi a^2} = \frac{P}{\pi E_f a} \quad (49)$$

and

$$\overline{w} \bigg|_{arc} = \frac{\int_0^{\pi/2} w \big|_{surf} \, a d\theta}{\pi a/2} = \frac{9P}{8\pi E_f a} \quad (50)$$

whence

$$\overline{w} \bigg|_{arc} = 1.125 \, \overline{w} \bigg|_{surf}.$$

The average deflection for a circular area of radius a loaded by a uniform pressure p is given as (Reference 4, page 409):

$$\overline{w}_{press} = \frac{0.54 \, P \, (1-\nu^2)}{E_f a}$$
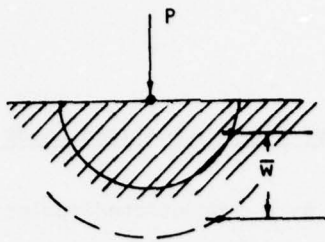
(a) COMPUTE AVERAGE DEFLECTION OVER A CIRCULAR ARC
(RADIUS a= PIN DIA ÷ 2) PRODUCED BY A CONCENTRATED
FORCE P.
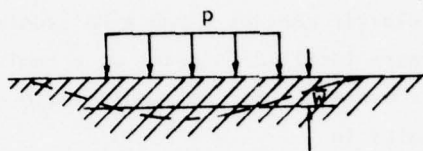
(b) COMPUTE AVERAGE DEFLECTION OVER CIRCULAR AREA OF
RADIUS a UNDER UNIFORM PRESSURE $p = P/(\pi a^2)$
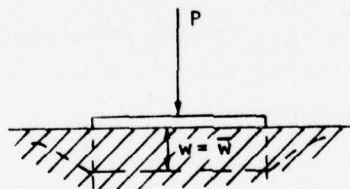
(c) CALCULATE DEFLECTION UNDER A RIGID DIE OF RADIUS
a LOADED BY A CONCENTRIC FORCE P.

Figure 13. Approaches to Determination of
Foundation Stiffness Under a
Highly Localized Load

-44-

This result applies to Figure 13(b).

Use of Equations (49) and (50) result in:

$$\bar{w}\Big|_{surf}\Big/\bar{w}_{press} = 0.786 \tag{51}$$

and

$$\bar{w}\Big|_{arc}\Big/\bar{w}_{press} = 0.884. \tag{52}$$

The deflection for the rigid die (Figure 13(c)) under a load P is given by (Reference 2, page 323):

$$\bar{w}_{rigid} = \frac{P(1-\nu^2)}{2aE_f}$$

Again using Equations (49) and (50) and taking $\nu = 1/2$,

$$\bar{w}\Big|_{surf}\Big/\bar{w}_{rigid} = 0.849 \tag{53}$$

$$\bar{w}\Big|_{arc}\Big/\bar{w}_{rigid} = 0.955 \tag{54}$$

It appears that, for the same total force, the technique of averaging the deflections due to a point load over the arc of radius a produces nearly the same result as obtained for the deflection of a rigid die of the same radius and a result close to that for a circular area of radius a under a uniform pressure.

Timoshenko and Goodier show that Equation (47), when integrated for the case of Figure 13(b), produces the following results along the loaded surface (Reference 4, pages 403 - 409)

$$w_{max} = \frac{2(1-\nu^2) pa}{E_f} = \frac{2(1-\nu^2) P}{\pi E_f a} \tag{55}$$

$$\bar{w} = \frac{0.54 P (1-\nu^2)}{E_f a} = \frac{0.54\pi pa (1-\nu^2)}{E_f} \tag{56}$$

-45-

$$w = \frac{4 \, (1-\nu^2) \, pr}{\pi E_f} \left[F_1 \left(\frac{a}{r}, \frac{\pi}{2} \right) - \left(1 - \frac{a^2}{r^2} \right) F_2 \left(\frac{a}{r}, \frac{\pi}{2} \right) \right] \tag{57}$$

for $a < r < \infty$, and

$$w = \frac{4 \, (1-\nu^2) \, pa}{\pi E_f} \left[F_1 \left(\frac{r}{a} \right) \right] \tag{58}$$

for $0 \leq r \leq a$

where F_1 denotes an elliptic integral of the first kind and F_2 denotes an elliptic integral of the second kind. Equations 57 and 58 were normalized with respect to w_{max} (Equation (55)) and the values of this normalized deflection were plotted to produce Figure 14. The deflection produced by an equivalent point load (Equation (47)) is also shown in Figure 14. It is noticeable that the two curves are almost indistinguishable for r/a greater than 3. Another noticeable feature is the rapidity with which the local deflections die out. Before drawing any conclusions, however, the effects of an opposing load, coaxial with the load of interest but acting at a distance L_o along the axis, must be considered. As a first step, the deflection at points on the z axis (see inset, Figure 14) can be found by integrating Equation (47), with the result

$$w \bigg|_{r=0} = \frac{P}{E_f} \left[z^2 \, (1+\nu) \left(\frac{1}{z} - \frac{1}{\sqrt{a^2 + z^2}} \right) + 2 \, (1-\nu^2) \left(\sqrt{a^2 + z^2} - z \right) \right]. \tag{59}$$

It is easily demonstrated that this equation produces the same value of $w = w_{max}$ for r = 0, z = 0 as is given by Equation (55). Taking $\nu = 1/2$ and normalizing with respect to w_{max},

$$\left(w / w_{max} \right)_{r=0} = \sqrt{1 + \left(\frac{z}{a} \right)^2} - \frac{(z/a)^2}{\sqrt{1 + \left(\frac{z}{a} \right)^2}} \tag{60}$$

Equation (60) is plotted in Figure 15, along with the normalized deflection produced along the z axis by an equivalent point load. Note that, as in Figure 14, the point and distributed loads produce essentially identical
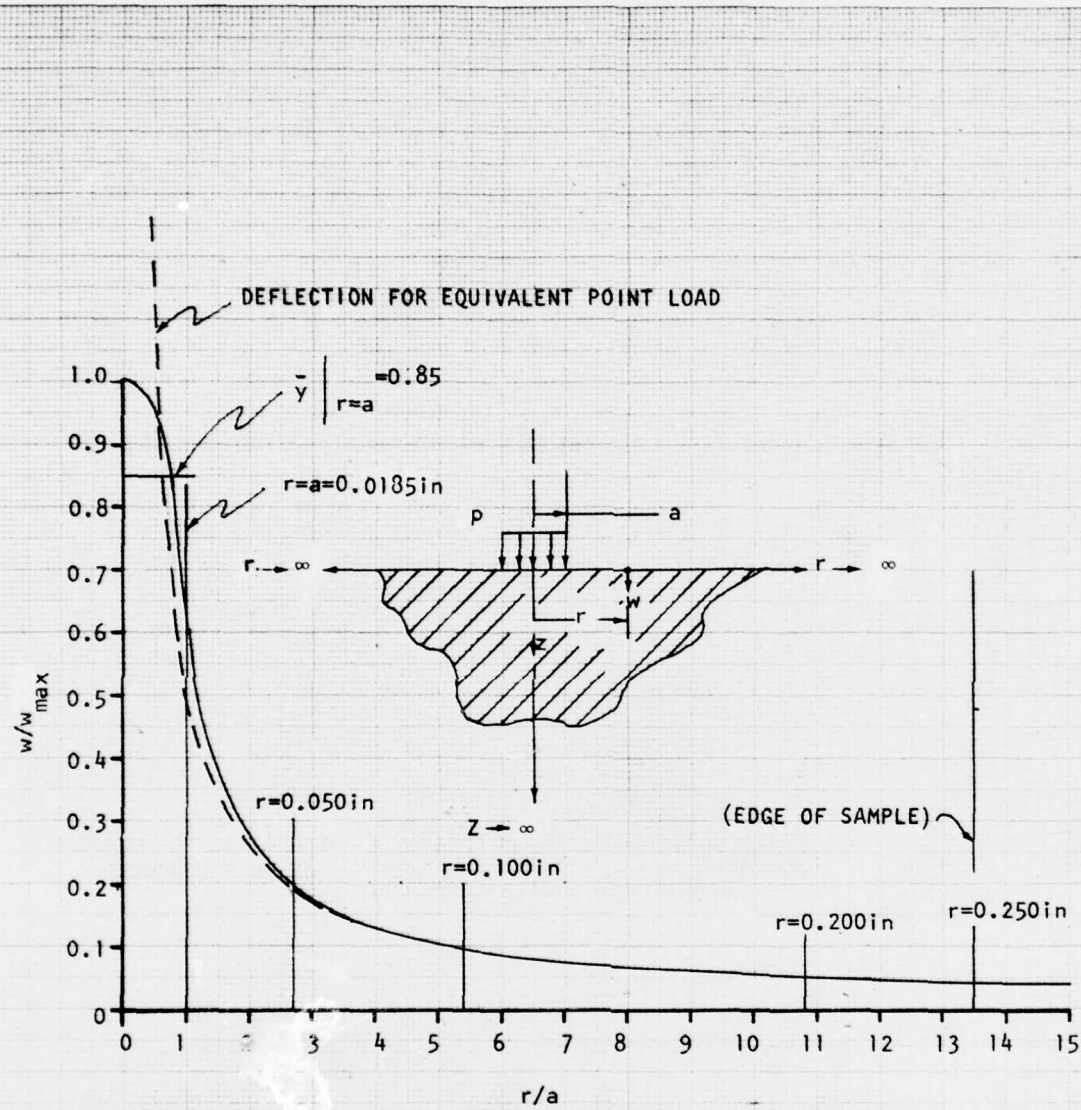
-46-

Figure 14. Deflection Along Free Surface of a
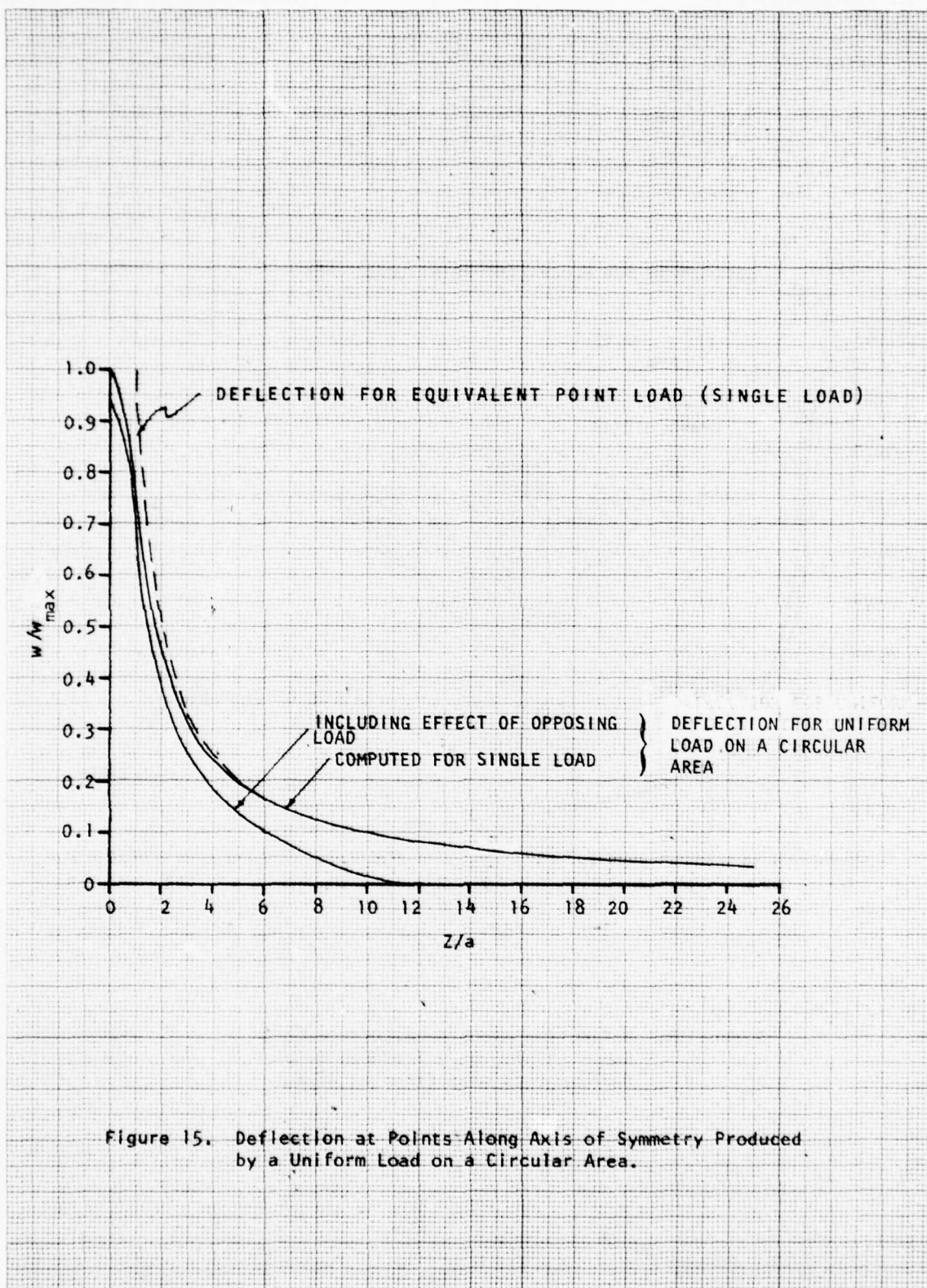Semi-infinite Body Produced by a
Uniform Load on a Circular Area

Figure 15. Deflection at Points Along Axis of Symmetry Produced by a Uniform Load on a Circular Area.

results at a characteristic dimension $\frac{z}{a} \cong 3$ and beyond. Figure 15 also
shows the results of superposing the deflections for two distributed loads:
one acting downward at $z = 0$ and one acting upward at $z = L_o = 0.4$, or
$z/a = L_o/a = 0.4/0.0185 = 21.62$, i.e.:

$$\left. \frac{w_{net}}{w_{max}} \right|_{r=0} = \left(\left. \frac{w}{w_{max}} \right|_{\substack{r=0 \\ z=0}} - \left. \frac{w}{w_{max}} \right|_{\substack{r=L_o \\ z=0}} \right)$$

Comparing the deflection curve for the two opposed load distributions with
that for the single load distribution, it appears that the deflection under
each load is decreased by the presence of the opposing load. The effective
stiffness of the medium, in other words, is increased by the interference
between the two loads.

Taking advantage of the rapid convergence between the distributed-load and
point-load deflection curves as z/a increases (Figure 15), the distributed-
load deflection at the loaded surface (Figure 14) was corrected for the
presence of an opposing distributed load at $z/a = L_o/a$ by substituting an
equivalent point load for the distributed opposing load. The result is
shown in Figure 16. Also shown in Figure 16 is the normalized average
deflection of the uniaxial specimen, computed by integrating the strain
given by Equation (2) over the length L_o. ($P' = 2P$ was substituted for P
in Equation (2) to account for the use of a semi-infinite body model rather
than an infinite body model in the above analyses. Notice also that
Figure 16 attributes the final result to the infinite body rather than to
the semi-infinite body. As discussed in 3.2.1, this procedure is valid
only for a Poisson's ratio of 1/2.)

Comparing Figures 15 and 16, it can be seen that the average deflection over
the loaded area is reduced from 0.85 w_o to 0.799 w_o by the interference
effect of the second load. This represents an increase of 6 percent in the
effective stiffness of the medium. It is also apparent that the interference
from the second load causes the deflection curve to "damp out" somewhat more
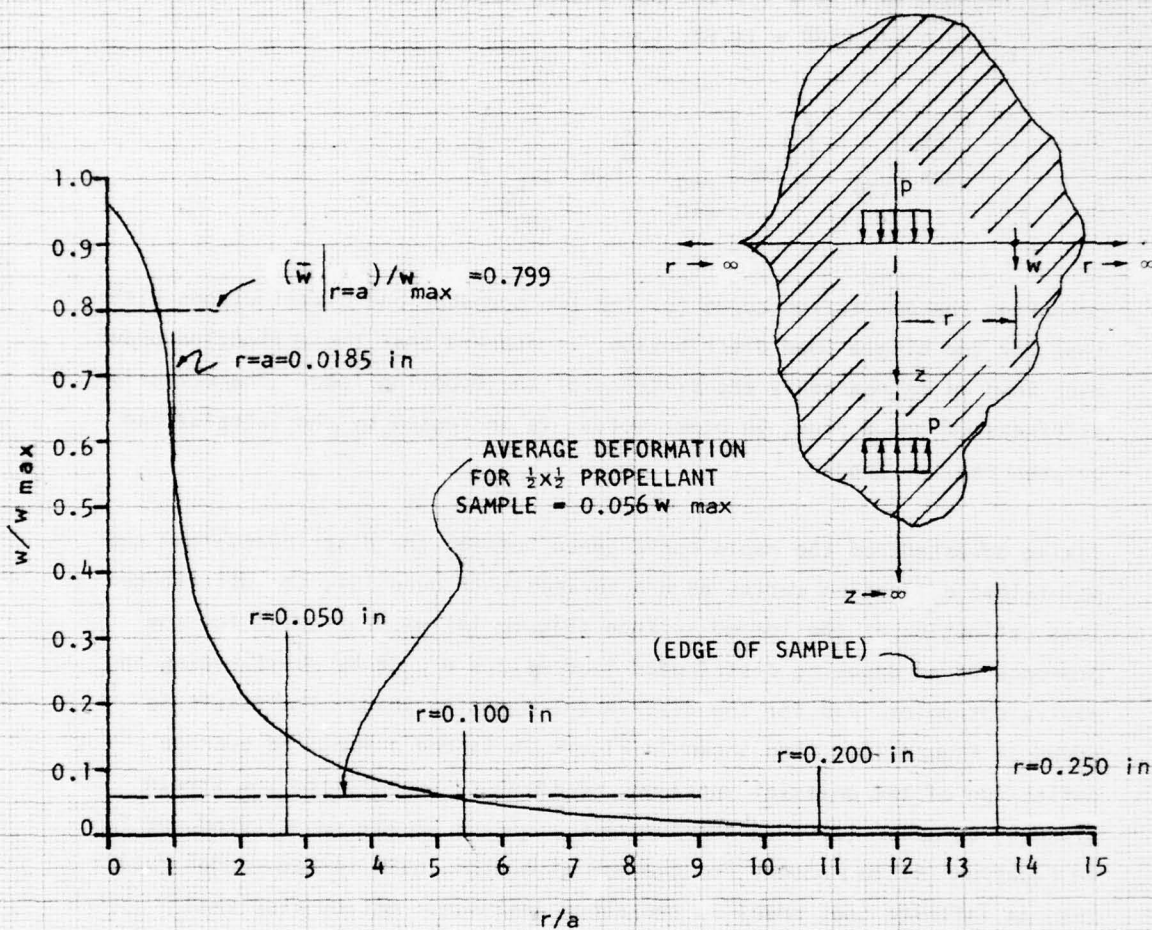
-49-

Figure 16. Deflection Along Loaded Surface of an Infinite Body Produced by Opposing Uniform Loads on Circular Areas (Valid for $\nu = \frac{1}{2}$).

rapidly as r/a increases. These results indicate that the effects of this interference must be considered in the analyses of the mounting pins.

Figure 16 provides a basis for assessing the importance of "edge effects" on the validity of the infinite medium model for analyzing the interaction of the pin with the finite sample. It is evident in Figure 16 that the deflection is negligible for values of r/a greater than 5. We can therefore infer, in an argument parallel to the one Den Hartog uses for the infinite beam (see 3.2.2), that material beyond r/a = 5 could be physically removed with little effect on the average deflection. In fact, it would appear qualitatively that removal of all material to the right of a plane tangent to r/a of, say, 2 or 3 would still have little effect on the average deflection or effective medium stiffness. However, the impact of removing material would rapidly increase for smaller values of r/a and would certainly be significant as the plane approached r/a = 1. We can therefore conclude that the infinite-medium result applies accurately for a localized load provided the loaded area is at least two to three times its own radius distant from a free surface, but that the infinite-medium result underpredicts the deflections when the loaded area is closer to the surface. This conclusion will be of use in the following subsection of this report.

One final useful observation can be made based on Figure 16. The normalized deflection curve depicts the local deflections of an infinite medium under a highly localized load. However, nearly identical localized deflections must occur within a finite sample under the same load, provided it is sufficiently large that edge effects can be ignored (as discussed above). These conditions are satisfied for the 1/2-inch by 1/2-inch propellant sample, as is evident from Figure 16. Based on St. Venant's principle (Reference 5, page 117) we would expect the localized effects of the concentrated load to be merely a perturbation on the average sample behavior. In other words, if we consider the deflection in the finite sample to be given by the sum of two components,

$$w = w_{uniaxial} + w_{local} \tag{61}$$

-51-

where $w_{uniaxial}$ is given by Equation (2), we would expect that

$$\bar{w} = \bar{w}_{uniaxial} = \overline{w \; uniaxial} + \bar{w}_{local}$$

or

$$\bar{w}_{local} = 0.$$

However, numerically averaging the deflection curve of Figure 16 produces the result

$$\bar{w}/w_{max} \bigg|_{r=0.25} = 0.0349$$

while the uniaxial deflection for the 1/2 x 1/2 sample was computed as

$$w_{uniaxial}/w_{max} \bigg|_{z=0} = 0.056$$

It appears, then, that the deflection calculated for the infinite medium is more nearly equal to the total local deflection of the sample than to the component w_{local}. In fact, the component of deflection w_{local} is approximately given by

$$w_{local} = w_{inf\ medium} + w_{uniaxial} \tag{62}$$

This result will be utilized in the following subsection.

3.2.4.2   Deflection Under Distributed Localized Loads.

Since the major part of both the localized and the average deformation of the sample is in flexure rather than axial deformation, a foundation stiffness derived from response to a distributed bending moment appears to be appropriate. The simplest load of this type is the triangularly-distributed line load of Figure 17(a). Rewriting Equation (47) (in the differential form) in terms of the variables shown in Figure 17 and substitution of $\nu = 1/2$ results in the differential equation for deflection within a semi-infinite medium:

-52-
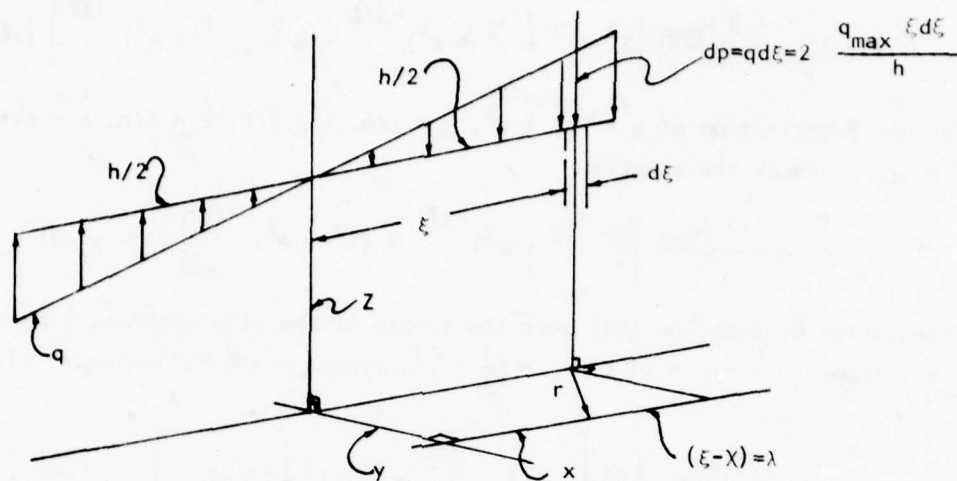
(a)   Triangular Load Distribution and Geometry
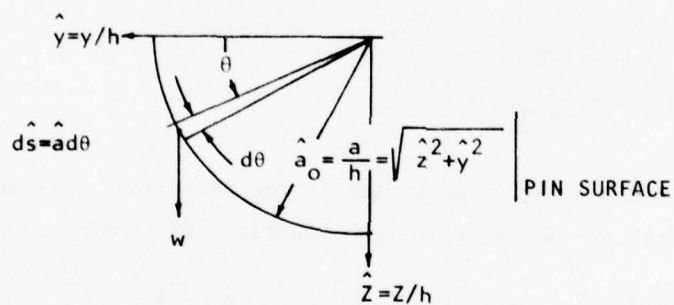
(b)   Integration Contour for Calculation of $\bar{w}_o$

Figure 17.   Nomenclature for the Analysis of Deflections Under a Triangular Load Distribution

-53-

$$dw = \frac{1.5\ q_{max}}{\pi E h} \left[z^2 \left(\lambda^2 + y^2 + z^2\right)^{-3/2} + \left(\lambda^2 + y^2 + z^2\right)^{-1/2} \right] (\lambda + \chi)\ d\lambda.$$

Further substitution of $a = \sqrt{y^2 + z^2}$, $\hat{\chi} = \chi/h$, $\hat{y} = y/h$, $\hat{z} = z/h$, $\hat{a} = a/h$ and $\hat{\lambda} = \lambda/h$ produces the equation

$$dw = \frac{1.5\ q_{max}}{\pi E} \left[\hat{z}^2 \left(\hat{\lambda}^2 + \hat{a}^2\right)^{-3/2} + \left(\hat{\lambda}^2 + \hat{a}^2\right)^{-1/2} \right] (\hat{\lambda} + \hat{\chi})\ d\hat{\lambda} \quad (63)$$

Integration of Equation (63) over the length of the clip gage mounting pin, i.e., from $\hat{\lambda}_1 = -\left(\hat{\chi} + \frac{1}{2}\right)$ to $\hat{\lambda}_2 = \left(\frac{1}{2} - \hat{\chi}\right)$, produces the following result:

$$w = \frac{1.5\ q_{max}}{\pi E} \left\{ \hat{z}^2 \left[\frac{-1}{\sqrt{\hat{\lambda}^2 + \hat{a}^2}} \right]_{\hat{\lambda}_1}^{\hat{\lambda}_2} + \hat{z}^2\ \frac{\hat{\chi}}{\hat{a}^2} \left[\frac{\hat{\lambda}}{\sqrt{\hat{\lambda}^2 + \hat{a}^2}} \right]_{\hat{\lambda}_1}^{\hat{\lambda}_2} + \left[\sqrt{\hat{\lambda}^2 + \hat{a}^2} \right]_{\hat{\lambda}_1}^{\hat{\lambda}_2} \right.$$

$$\left. + \left[\hat{\chi}\ \ell n \left(\hat{\lambda} + \sqrt{\hat{\lambda}^2 + \hat{a}^2} \right) \right]_{\hat{\lambda}_1}^{\hat{\lambda}_2} \right\} \quad (64)$$

If we now define $w_o = w \bigg|_{\substack{\hat{\chi}\ =\ 1/2 \\ \hat{a}\ =\ a_{pin}/h\ =\ \hat{a}_o}}$, i.e., the value of

w at the end of the pin and lying on a surface in the propellant corresponding to the pin's surface, it can be shown from Equation (64) that

$$w_o = \frac{1.5\ q_{max}}{\pi E} \left[\left(\hat{a}_o^2 \sin^2\theta\right) k_1 + k_2 \right] = k \left[\left(\hat{a}_o^2 \sin^2\theta\right) k_1 + k_2 \right] \quad (65)$$

where θ is defined in Figure 17(b). Integrating Equation (65) with respect to $ds = \hat{a}_o d\theta$ from $\theta = 0$ to $\theta = \pi/2$ and dividing by $(\pi \hat{a}/2)$ yields the following average value for $\overline{w}_o$:

$$\overline{w}_o = k\ (2\hat{a}^2) \left[\frac{k_1}{4} + \frac{k_2}{2\hat{a}^2} \right]$$

-54-

Evaluation of k_1 and k_2 from Equation (64) with $\hat{a}$ = (.0185)/(0.5) = 0.037, $\hat{\lambda}_1$ = -1, and $\hat{\lambda}_2$ = 0 yields the result

$$\overline{w}_o = 1.2635 \, k = 1.2635 \left(\frac{1.5 \, q_{max}}{\pi E h} \right)$$

and Equation (64) becomes

$$w/\overline{w}_o = 0.7915 \left\{ \hat{z}^2 \left[\frac{-1}{\sqrt{\hat{\lambda}^2 + \hat{a}^2}} \right]_{\hat{\lambda}_1}^{\hat{\lambda}_2} + \hat{z}^2 \left[\frac{\hat{\chi}}{\hat{a}^2} \frac{\hat{\lambda}}{\sqrt{\hat{\lambda}^2 + \hat{a}^2}} \right]_{\hat{\lambda}_1}^{\hat{\lambda}_2} + \left[\sqrt{\hat{\lambda}^2 + \hat{a}^2} \right]_{\hat{\lambda}_1}^{\hat{\lambda}_2} \right.$$

$$\left. + \left[\hat{\chi} \, \ell n \left(\hat{\lambda} + \sqrt{\hat{\lambda}^2 + \hat{a}^2} \right) \right]_{\hat{\lambda}_1}^{\hat{\lambda}_2} \right\} \qquad (66)$$

Equation (66) was programmed on a programmable calculator and calculations were performed both for a single triangular load distribution and for two opposed triangular load distributions separated along the z-axis by a distance of L_o = 0.4 inches. The results are shown in Figures 18, 19, and 20. The influence of the second line load (compare Figure 18(a) with Figure 18(b)) is quite similar to that found for interacting highly localized loads in the previous subsection; i.e., deflections are slightly reduced. Figure 19 shows the variation in deflection along the (imaginary) "pin surface" at the extreme end of the pin axis. There is, of course, significant distortion of this surface as the medium deflects under the line load, although this distortion is considerably less than the distortion of a circular arc around a point load (this comparison is shown in Figure 19). Since it was shown in the preceding subsection that the average deflection over the circular arc produced by the point load closely duplicated the deflection under an equivalently-loaded rigid die, averaging deflections over this imaginary "pin surface" should provide a good estimate of the deflection under a rigid die of width 2a and length h, subjected to a load equivalent to that in Figure 17(a). The calculated deflections along the "pin surface" for four values of θ from 0° to 90° are plotted in Figure 20. As noted from Figure 19, there is distor-

-55-
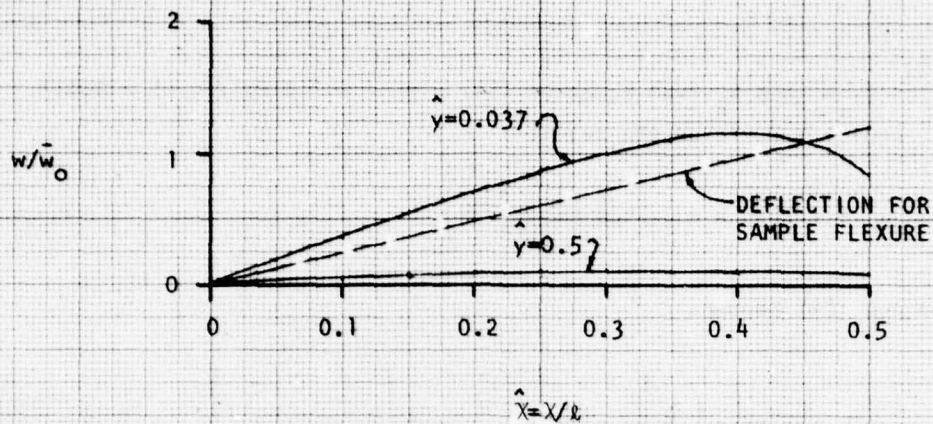
(a) Deflections at $\hat{z}=0$ Due to Single Triangular Distribution
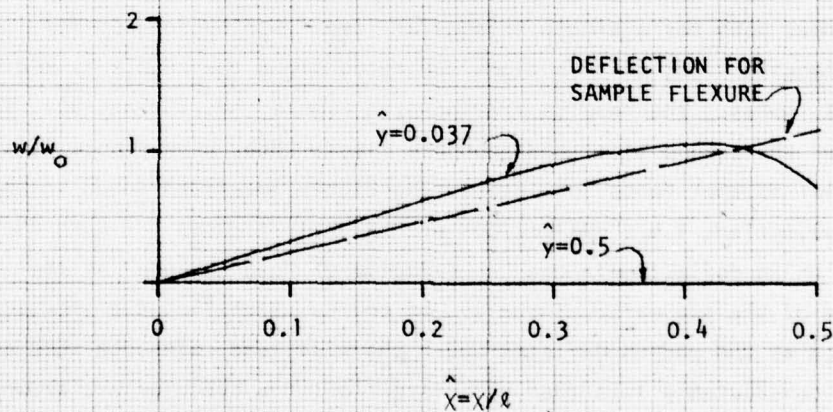
(b) Deflections at $\hat{z}=0$ Due to Two Opposed Triangular Distributions

Figure 18. Deflections Produced in an Infinite Medium by
the Triangular Load Distribution of Figure 17(a)

-56-
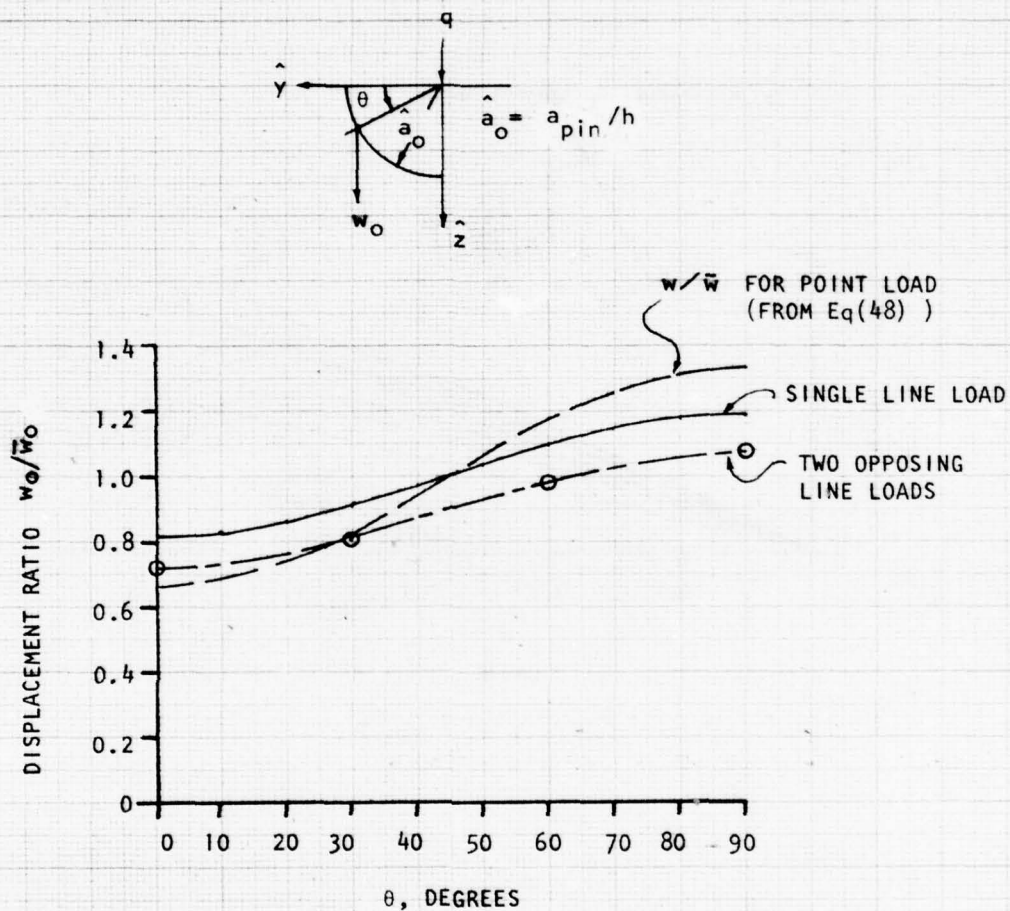
Figure 19. Deflection Distribution Along an Arc of Radius a_o (at $x=\frac{1}{2}$) Produced by the Triangular Load Distribution of Figure 17(a).
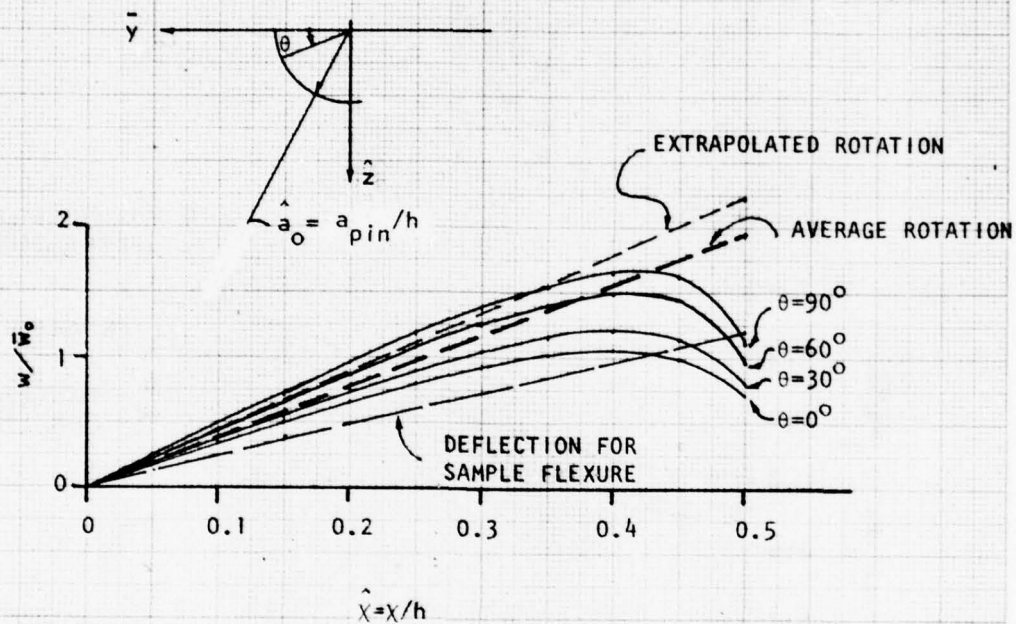
-57-

Figure 20. Deflections on a Cylindrical Surface of Radius $\hat{a}_o=0.037$ Produced by the Triangular Load Distribution of Figure 17(a).

for the intended use. Thiokol attempted to

tion of each cross section of the "pin" as it deflects. There is also a
substantial bending deformation which would not occur with a rigid die.

One approach to the desired stiffness calculation is to calculate the average
rotation over the length of the "pin" and take this value as the "rigid die"
deformation. This calculation was performed by averaging the four deformations
at each cross section, computing $(\overline{w}/\overline{w}_o)/\hat{\chi}$, and averaging these values to
compute a rotation. In the course of these calculations, it was found that
the deflected shapes of the cross sections were very nearly geometrically
similar: $(w/\overline{w}_o)/\hat{\chi}$ had almost exactly the same shape at each cross section.

While the above approach (which yields the line labeled "average rotation"
in Figure 20) is straightforward, it neglects the "edge effects" discussed
in the preceding subsection of this report. As noted in the discussion of
Figure 16, these effects begin to be important as the distance from the free
surface decreases below two to three times the radius of the loaded area.
The corresponding values of $\hat{\chi}$ in Figure 20 are

$$\hat{\chi}\Big|_{\frac{r}{a} = 2} = 0.5 - 2\,(.037) = 0.426$$

$$\hat{\chi}\Big|_{\frac{r}{a} = 3} = 0.5 - 3\,(.037) = 0.389$$

It appears, therefore, that the "edge effects" would begin to reduce the
localized stiffness of the medium (i.e., to increase the localized deflections)
at approximately the point for which the deflection curves of Figure 20 begin
to "bend over." Furthermore, the localized effective stiffness would be
expected to drop to about half the value in the center of the sample at the
edge of the sample (i.e., the deflections would double). The net effect would
be to approximately negate the departure of the deflection curves in Figure 20
for χ/h greater than 3. Based on this reasoning, and on the observed similarity
in the cross-sectional shapes, the maximum deflection for stiffness calculation

-59-

purposes was determined as follows:[2]

(1) From Figure 20, it was determined that $w_o = \bar{w}_o$ when $\theta \simeq 65°$

(2) This value of θ was used to calculate $(\bar{w}/\bar{w}_o)_{x = 0.2}$

(3) This value of $\bar{w}/\bar{w}_o$ was then used to extrapolate $\bar{w}/\bar{w}_o$ to $\hat{x} = 0.5$, obtaining $(\bar{w}/\bar{w}_o)_{max} = 2.22$

The value thus obtained is considerably higher than the "average rotation" value of 1.90 (see Figure 20).

3.2.4.3 Effective Foundation Stiffness.

The preceding subsection provides a calculated deflection distribution produced in a semi-infinite medium by the triangular load distribution of Figure 17(a). If we take the deflection as an effective linear distribution, the foundation stiffness is given by the definition of k:

$$k = q/w = \frac{2\, q_{max}}{\bar{w}_{max}} = \frac{2\, q_{max}}{(\bar{w}/\bar{w}_o)\,(\bar{w}_o/k)\,k}$$

Where the factor 2 is applied to q_{max} to obtain the stiffness for an infinite medium instead of a semi-infinite medium. From the preceding subsection, $(\bar{w}/\bar{w}_o) = 2.20$, $(\bar{w}_o/k) = 1.2635$, and $k = (1.5\, q_{max})/(\pi E_f)$. Substitution of these values into the above equation produces the result

$$k = 1.494\, E_f \tag{67}$$

----

2. In retrospect, step (1) of this procedure was based on an erroneous assumption that unsymmetrical distortion was responsible for w_o not being equal to $\bar{w}_o$ at $\theta = 45°$. Actually, as is evident in Figure 19, the shift in $\bar{w}/\bar{w}_o$ is simply the result of interference from the opposing line load. The resulting value of $(\bar{w}/\bar{w}_o)_{max}$ is about 10 percent too high (a small error in view of the uncertainties involved).

-60-

For comparison, values of k can be calculated for the highly localized loads analyzed in 3.2.4.1. Define the load per unit length for the circular areas of Figure 13 as $q = P/\ell$ where P is the total load and ℓ is the length of an equivalent square (i.e., a square having the same area as the circle). Then

$$q = \frac{P}{\sqrt{\pi}(a)}$$

and, for the average deflection produced by a point load acting within an infinite medium, we have, from Equation (50)

$$\overline{w} = \frac{1}{2} \left(\overline{w} \Big|_{\text{semi-infinite medium}} \right) = \frac{1}{2} \left(\frac{9P}{8\pi E_f a} \right) = \frac{1}{2} \left(\frac{9}{8\sqrt{\pi} E_f} \right) q$$

so

$$k = q/\overline{w} = \frac{2 \, (8\sqrt{\pi}) \, E_f}{9} = 3.151 \, E_f$$

(point load, deflection averaged over arc of radius a).

Similar calculations result in the following stiffness values:

Uniform pressure on a circular area: $k = 2.786 \, E_f$

Deflection of a rigid circular die: $k = 3.009 \, E_f$.

The selected technique (Equation (67)) of calculating stiffness of the medium therefore results in a stiffness about half that for a highly localized load on a circular area. However, the selected stiffness is very close to the value obtained for a square area loaded by a uniform pressure.

3.2.4.4 Adjustment for Sample Flexural Deformation.

The triangular load distribution of Figure 17(a) is statically equivalent to a pure bending moment given by

-61-

$$M_\ell = 2 \int_0^{h/2} \frac{2\, q_{max}}{h} \xi^2 d\xi = \frac{q_{max}\, h^2}{6}$$

acting on the semi-infinite body of the analysis. The moment acting on an infinite body (the propellant sample) is twice this value, or

$$M_o = 2M_\ell = \frac{q_{max}\, h^2}{3} \; .$$

From the analysis of 3.1, the bending moment in the sample gage length is, since $R_1 \equiv 0$, (Equations (3) and (5))

$$M = -M_1 + R_1 z + M_o = -M_1 + M_o$$

where (Equation (4))

$$M_1 = -\frac{M_o}{\ell^2}\left[2\ell a - \ell^2\right]$$

substitution of the above expression for M_o yields

$$M = \frac{-2\, M_o\, a}{\ell} = \frac{-2\, q_{max}\, h^2 a}{3\ell}$$

and the surface bending strain in the center section of the sample is given by

$$(\Delta\epsilon_z)_{bending} = \frac{Mh}{2E_f I} = \frac{-q_{max}\, h^3 a}{3E_f I \ell}$$

The surface axial deflection at $z = a$ (see Figure 1) is given by

$$(w_{max})_{sample} = \frac{-L_o}{2}(\Delta\epsilon_z)_{bending} = \frac{q_{max}\, h^3 a\, L_o}{6E_f I \ell}.$$

where a factor of -1 is incorporated because a negative strain produces a positive value of w.

-62-

Recognizing that $I = h^4/12$,

$$(w_{max})_{sample} = \frac{2 \, q_{max} \, a \, L_o}{E_f h \ell}.$$

and, since $\overline{w}_o = 1.2635 \, (1.5 \, q_{max})/(\pi E_f)$,

$$\left[(w_{max})_{sample}/\overline{w}_o\right] = \frac{2 \, \pi \, a \, L_o}{(1.2635)(1.5) \, h \ell}$$

substituting $a = 1.80$ inches, $L_o = 0.4$ inches, $h = 0.5$ inches, and $\ell = 4$ inches produces the final result

$$\left[(w_{max})_{sample}/\overline{w}_o\right] = 1.193$$

This sample bending displacement is shown in Figures 18 and 20.

If we apply the same logic as in 3.2.4.1 the displacement in the z direction is given by

$$w = w_{sample} + w_{local} \tag{68}$$

where w_{sample} is the bending deflection of the sample treated as a beam, and

$$w_{local} = w_{inf \ medium} - w_{sample} = (w_{inf \ medium}) \, c \tag{69}$$

where

$$c = \frac{w_{inf \ medium} - w_{sample}}{w_{inf \ medium}}$$

and, substituting computed values for the deflections,

$$c = \frac{2.22 - 1.193}{2.22} = 0.463 \tag{70}$$

3.2.5   Added Bias in Strain Gage Measurement.

The preceding discussion provides the groundwork for computing the effect of
local deflections on the measurement bias produced by clip gage/sample inter-
action. The bias due to local deflections is considered as an additive effect
which is superimposed on the bias predicted by modeling the sample as a beam.
As shown in 3.2.4.4, the local component of deflection of the sample under a
triangular line load is considerably less than the deflection of an infinite
medium under the same load. The logical application of this result would be
to apply the calculated reduction factor (Equation (70)) to the pin deflec-
tions calculated earlier (in 3.2.3). Examination of Figure 12, however,
reveals a basic conflict with this concept. The rigid beam model, as shown
in Figure 12, produces a pin deflection curve which closely resembles the
deflection of a beam cross section under bending loads. The motion of the
pin is simply a magnified version of the cross-sectional deformation. However,
it is obvious in Figure 12 that this observation is not true for the infinite
beam model: the beam itself undergoes no rigid body motion, either in rotation
or vertical deflection. It therefore is apparent that the rigid body motion
of the pin produced by deformation of the sample as a beam must be added to
the deflection shown for the infinite beam in Figure 12 to obtain the total
motion of the pin. Conversely, the local component of the pin deflection is
equal to the deflection given by Figure 12 without the reduction factor of
Equation (70).

The calculator program used to generate Figure 11 was modified to apply the
reduction factor of Equation (70) to the "rigid beam" deflections and slopes;
the computed deflections and slopes for the infinite beam model were left
unchanged. The deflections and slopes were then interpolated by the calculator
program in the same way as in Figure 11. The results for an eccentricity of
0.050 inches are shown in Figures 21 and 22. As before, the interpolation
yields results that appear reasonable.

Figure 23 shows the bias in the strain measurement produced by local deforma-
tions alone, for several values of propellant modulus, as a function of eccen-
tricity. These results were calculated (by the calculator program discussed
above) according to Equation (46).
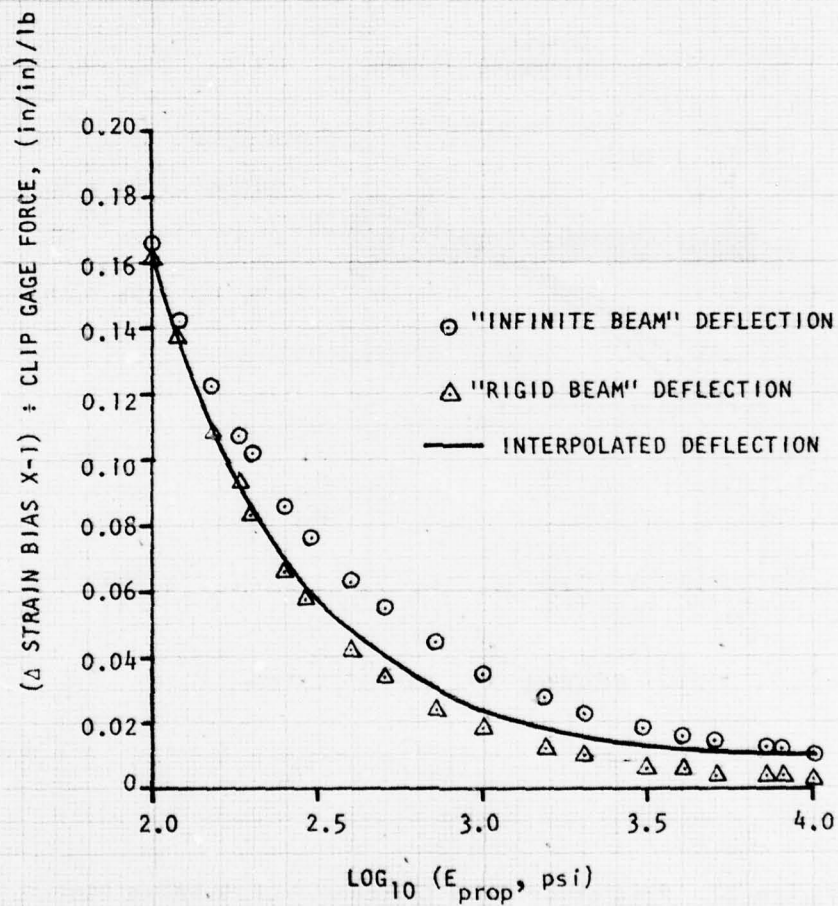
-64-

Figure 21. "Local Component" of Strain Bias (as a Function of Propellant Modulus) Produced by Local Deflection of Mounting Pins (Eccentricity=0.050 in.; Gage Length=0.400 in.)
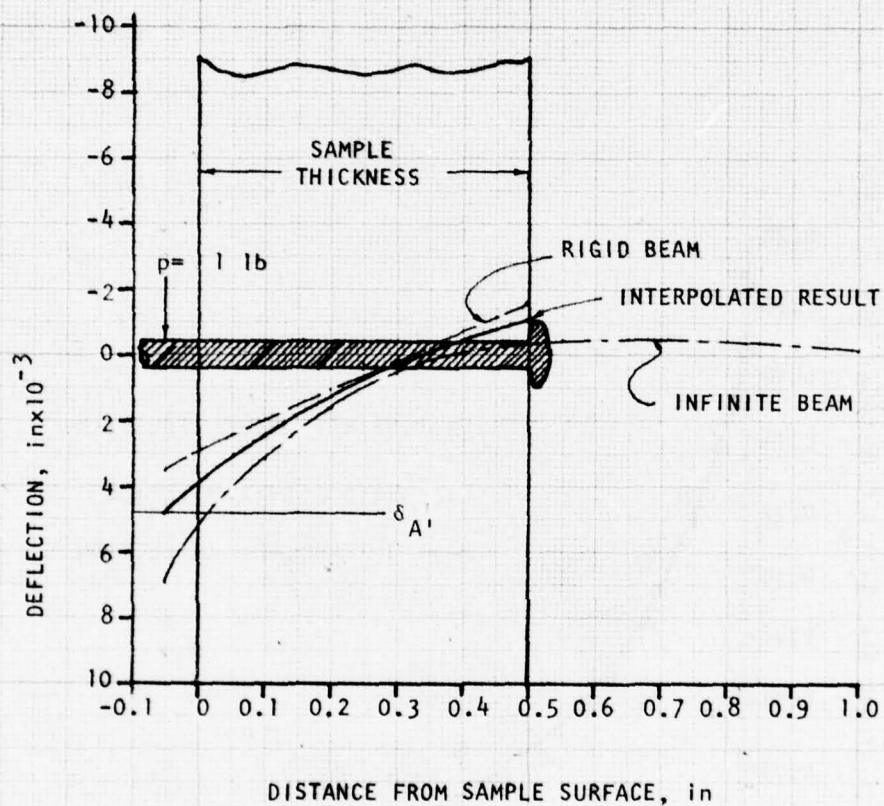
Figure 22. Predicted "Local Component" of Mounting Pin
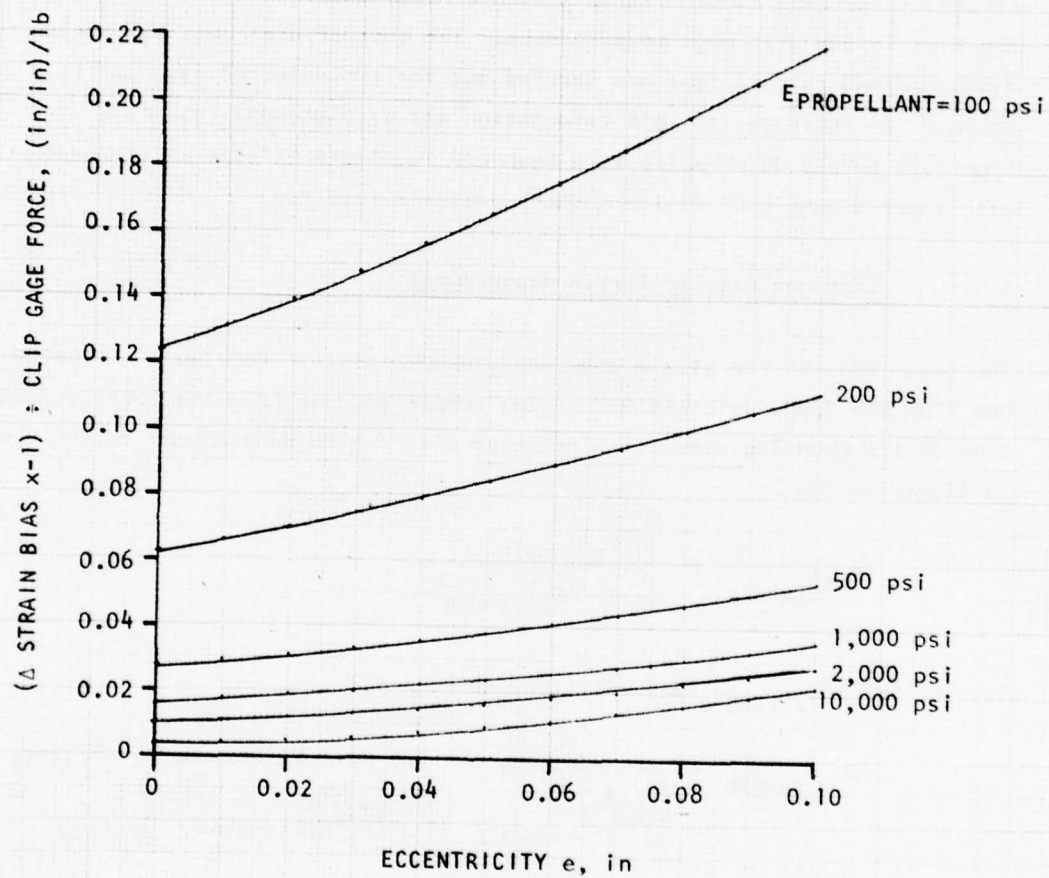Deflection (Propellant Modulus = 1000 psi).

Figure 23. Predicted Strain Bias Caused by Local Deflection of Mounting Pins (h=0.50 in, L_o=0.40 in)

3.3   Net Gage-Sample Interaction.

In 3.1 and 3.2 of this report, analyses were conducted to estimate the separate contributions to bias in clip strain gage measurements on a uniaxial tensile specimen caused by sample deformation (as a beam) and by local deformation of the clip gage mounting pins. The analyses in the present subsection combine these separate contributions to obtain the net bias in the clip gage measurements. The appropriate equations are developed and calculations are carried out for two selected gage stiffnesses. In addition, the pin deformation and displacement resulting from both sample deformation as a beam and localized effects is compared with three-dimensional finite element analysis results.

3.3.1   Combined Bias In Strain Measurement.

The total bias in the strain gage measurement results from two contributions: one from the "beam deformation" of the sample and one from the local deformation of the mounting pins. The relative bias due to sample beam deformation is (Equation (9a)):

$$(e_{RE})_{sample} = \frac{-(\Delta\epsilon_z)_{sample}}{\epsilon_o + (\Delta\epsilon_z)_{sample}}$$

Solving for $(\Delta\epsilon_z)_{sample}$ and substituting $\epsilon_o = 0.1$,

$$(\Delta\epsilon_z)_{sample} = \frac{\epsilon_o}{\left[\frac{1}{(-e_{RE})_{sample}} - 1\right]} = \frac{0.1}{\left[\frac{1}{(-e_{RE})_{sample}} - 1\right]} \tag{71}$$

As discussed in 3.1.1, this strain bias corresponds to a force P_o (the clip gage reaction force at 10 percent gage strain). For the same force P_o, the strain bias due to pin deformation is:

$$(\Delta\epsilon_z)_{pin} = P_o \left(\frac{\Delta\epsilon_z}{P}\right)_{pin}. \tag{72}$$

-68-

The net strain bias is therefore

$$(\Delta\epsilon_z)_{net} = (\Delta\epsilon_z)_{sample} + (\Delta\epsilon_z)_{pin} \qquad (73)$$

and the strain experienced by the sample when the gage strain is $\epsilon_o = 0.1$ is

$$\epsilon_{sample} = \epsilon_o + (\Delta\epsilon_z)_{net}.$$

Finally, the net relative bias in the strain gage measurement is

$$(e_{RE})_{net} = \frac{\epsilon_o - \epsilon_{sample}}{\epsilon_{sample}} = \frac{0.1}{\epsilon_{sample}} - 1 \qquad (74)$$

To calculate the combined measurement bias, the calculator program used to generate the results in 3.1 was modified slightly to allow calculation of $(e_{RE})_{sample}$ for fixed values of P_o and varying modulus; the calculator program for the pin deflection analysis was used to calculate the term $(\Delta\epsilon_z/P)_{pin}$ for the same modulus; and a new calculator program was written to carry out the calculations of Equations (71), (72), (73), and (74).

The results for two selected values of P_o are shown in Figures 24 and 25. Each set of computations was carried out for an eccentricity of zero and an eccentricity of 0.050 inches.

The value of P_o used in Figure 24 was 0.322 lb (corresponding to a spring constant of k = 8.05 lb/in at the fixed gage length of 0.4 inches). This corresponds to the calculated stiffness of Thiokol's early experimental clip gage, which was residual hardware from the Simulated Air Launch Environment (SALE) program (Reference 7). This gage is the "baseline" gage in 3.4. It appears that this gage would produce a measurement bias that would be unacceptable for most engineering purposes over the entire range of propellant modulus considered.[1] Since the gage was considered too stiff

1. Thiokol reported (Reference 6) a negative bias of approximately 35 percent for the baseline gage used on a propellant sample at room temperature in low rate tests. This is consistent with Figure 24.
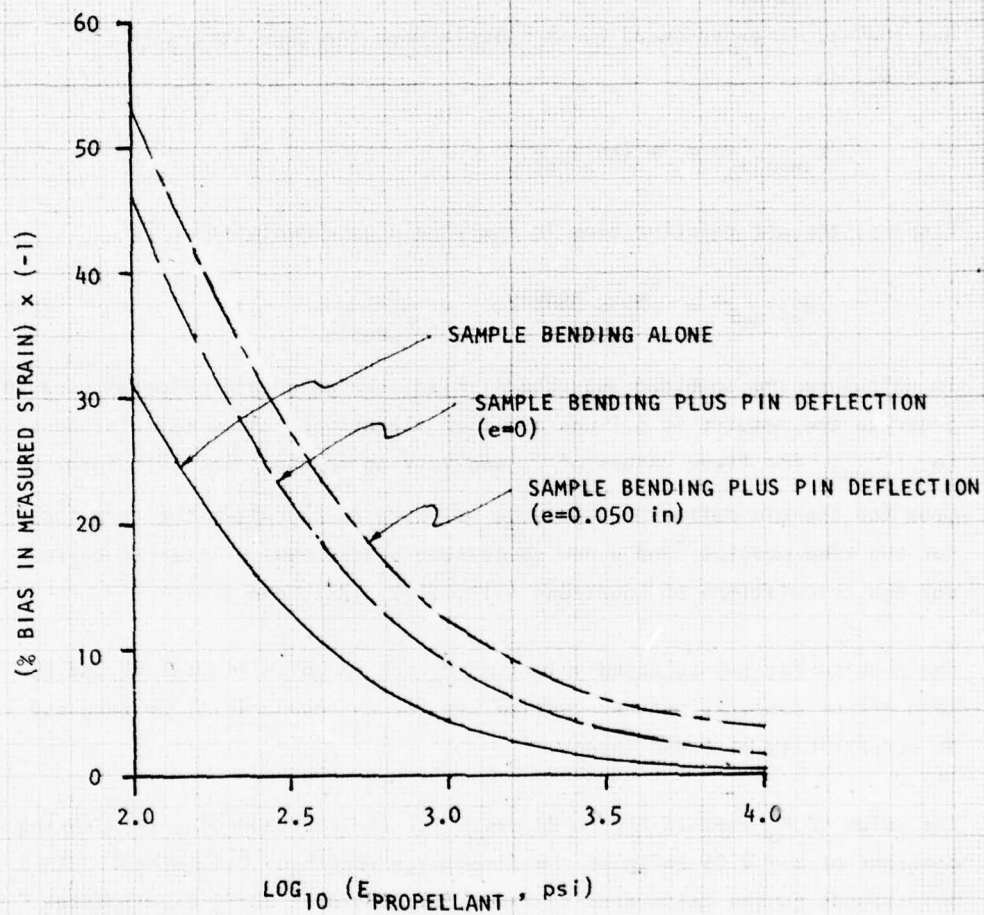
Figure 24. Expected Strain Measurement Bias for Baseline
Gage, Used on Tensile Specimen of Figure 2
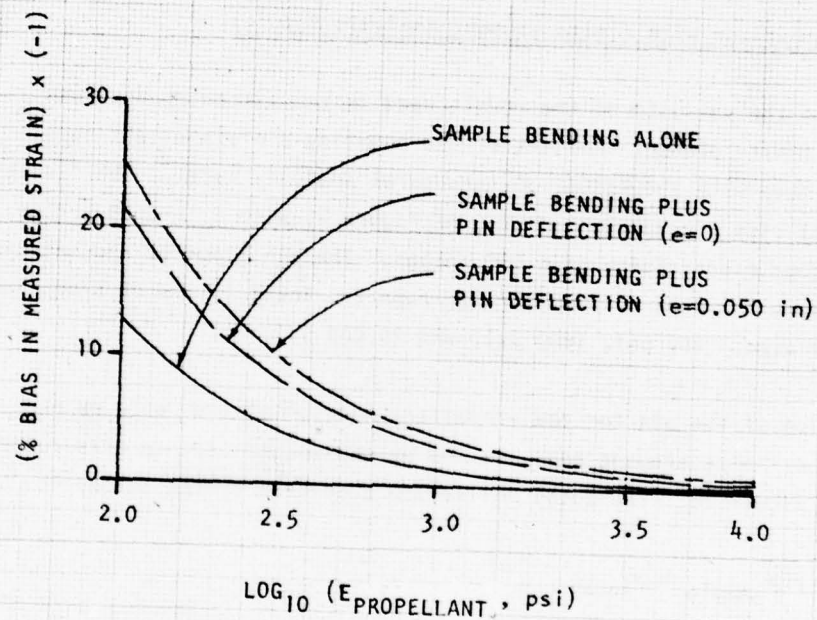(L_o=0.40 in).

Figure 25. Expected Strain Measurement Bias for a Clip Gage With a Spring Constant of 2.56 lb/in., Used on Tensile Specimen of Figure 2 (L_o=0.40 in)

for the intended use, Thiokol attempted to develop a much more compliant
gage. The final prototype gage produced had a stiffness of 2.56 lb/in
and a gage length of 0.40 inches. Figure 25 shows the predicted measurement
bias for this gage. Comparison of Figures 24 and 25 reveals that the 68
percent reduction in gage stiffness reduces the measurement bias by a
factor of roughly 50 percent at 100 psi and somewhat more at the higher
values of propellant modulus. The remaining measurement bias, however,
is still much larger than would be acceptable for most engineering purposes.

3.3.2   Comparison With Finite Element Analysis Results.

As a check on the validity of the models used in the preceding analyses,
independent finite element analyses of the mounting pin/propellant sample
system were made with the TEXGAP-30 structural analysis code.[1] The finite
element model used the sample geometry of Figure 1, with $L_o = 0.40$ inches
and a clip gage eccentricity of 0.050 inches. The pin diameter and material
properties were the same as used in this report. Three values of propellant
modulus were used: 200 psi, 1000 psi, and 20,000 psi.

The deflection of the pin for the propellant modulus of 1000 psi, as pre-
dicted by the finite element analyses and by the models used in this report,
is shown in Figure 26. The total deflection predicted by the latter is

$$w = w_{sample} + w_{local}$$

where

$$w_{sample} = \frac{L_o}{2} \left[(\Delta\epsilon_z)_{axial} + (\Delta\epsilon_z)_{bending} \right]_{sample} = \frac{L_o}{2} (\Delta\epsilon_z)_{sample}$$

Modifying Equation (7) to account for the loading eccentricity e,

---

1. These analyses were performed by Capt. J. Hildreth in the process of
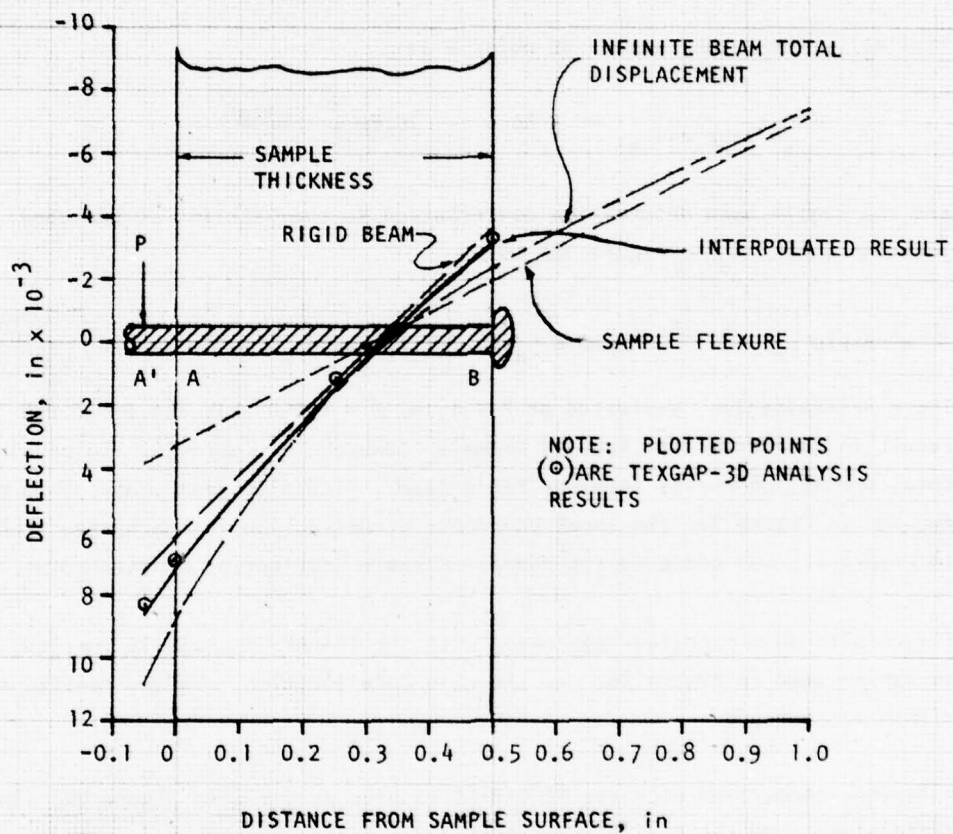checking out the new code on AFRPL's CDC 6400 computer system.

Figure 26. Predicted Total Deflection of Mounting Pins Including Both Sample Bending and Local Deflection (Propellant Modulus = 1000 psi).

The "beam" strain at the sample surface nearest the clip gage (point A in Figure 26) is

$$(\Delta\epsilon_z)_{sample}\Big|_A = 3.60\ \frac{P}{E} + 10.80\left(\frac{P}{E}\right)\left(\frac{h+2e}{h}\right)$$

Similarly, the "beam" strain at point B is

$$(\Delta\epsilon_z)_{sample}\Big|_B = 3.60\ \frac{P}{E} - 10.80\ \frac{P}{E}\left(\frac{h+2e}{h}\right)$$

and the sample beam deformation contribution to the "strain" at the gage location (point A' in Figure 26) is

$$(\Delta\epsilon_z)_{sample}\Big|_{A'} = (\Delta\epsilon_z)_{sample}\Big|_A + \left[(\Delta\epsilon_z)_{sample}\Big|_A - (\Delta\epsilon_z)_{sample}\Big|_B\right]\left(\frac{2e}{h}\right).$$

These relationships, evaluated at $P = 1$ lb, $E = 1,000$ psi, and $e = 0.050$ inches, result in the deflection labeled "Sample Flexure" in Figure 26. To obtain the total deflection curves labeled "Rigid Beam", "Infinite Beam", and "Interpolated Result" in Figure 26, the local component of deflection for each case (shown in Figure 22) was added to the "Sample Flexure" deflection at each point.

The results show excellent agreement with the TEXGAP-3D analysis results, as can be seen in Figure 26. At the clip gage location, the two results agree within 2.5 percent.

A further comparison with the TEXGAP-3D results is given in Figure 27. The deflections from the finite element analyses were converted to a relative bias in strain measurement by the equation

$$e_{RE} = \frac{-\Delta\epsilon_z}{0.1 + \Delta\epsilon_z}$$

where

$$\Delta\epsilon_z = \left(w'_A\Big|_{P = 1\ lb}\right)(P_o)\left(\frac{L_o}{2}\right).$$

-74-
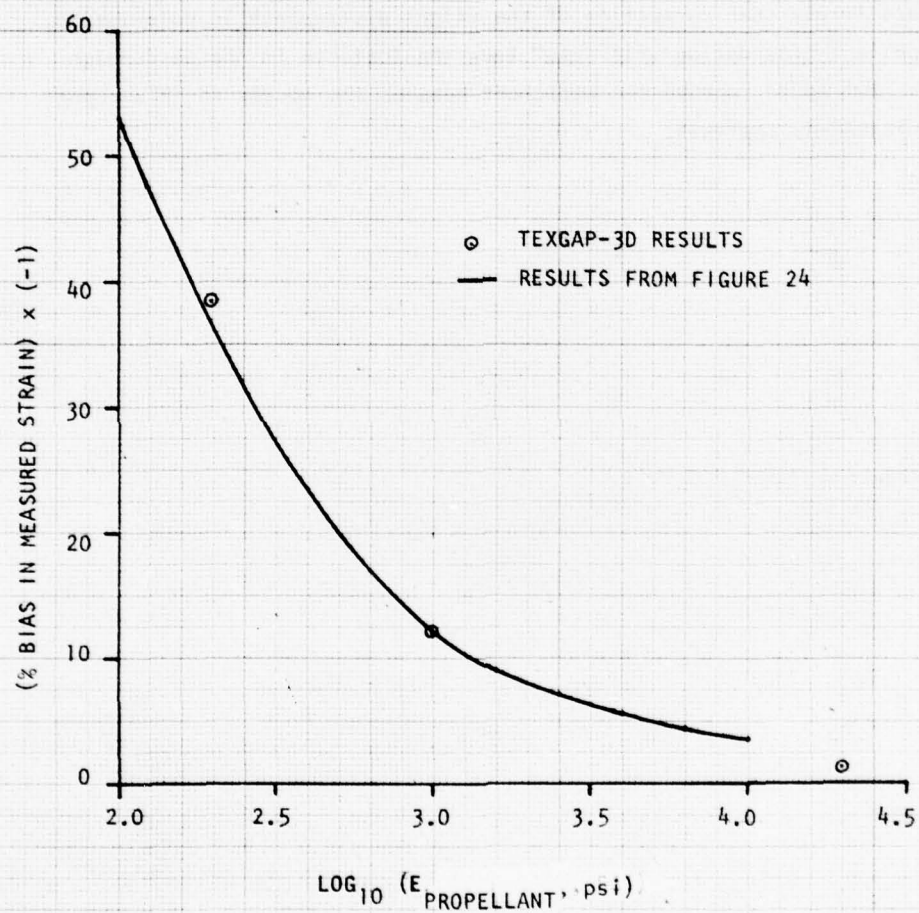
Figure 27. Comparison of Strain Measurement Bias from Figure 24 with Bias Predicted from TEXGAP-3D Analysis Results

Using $P_o = 0.32219$ lb and $L_o = 0.4$ lb, the three points plotted in Figure 27 were obtained, showing satisfactory agreement with the results obtained from the models used in this report over the wide modulus range considered. It appears likely that correction of the slight discrepancy in calculating the propellant "foundation stiffness" (see the footnote to the discussion of Figure 20) would improve the agreement between the models in this report and the TEXGAP-3D analysis.

3.4 Clip Gage Structural Behavior.

The analyses in this subsection were conducted to estimate the stiffness
and relative sensitivity of clip strain gages and then to use these results,
in combination with those of 3.1, to explore trade-offs between measurement
bias and gage output. As discussed at the beginning of section 3, the
analyses of the present subsection were completed before the importance of
the local deflections near the mounting pins was realized and before the
analyses of 3.2 and 3.3 were performed. Except where otherwise noted,
therefore, the strain measurement bias as used in this subsection includes
the sample beam deformation component only. Based on the results of 3.3,
the measurement bias actually expected would be roughly twice the bias
based on sample beam deformation alone.

3.4.1 Structural Model.

The deflection analysis of the clip gage structure was based on simple
elastic beam theory. In contrast to the propellant sample analyzed in
the preceding subsections, the basic structure of the clip gage (see
Figure 28) is composed of a material which can be regarded as being
linearly elastic with practically no error. The gage structure is fabri-
cated from Beryllium copper foil with Young's modulus of 18.5×10^6 psi
(Reference 8). The strain sensors themselves were not modeled in the present
analysis; the actual gages can therefore be expected to be somewhat stiffer
than predicted. The clip gage geometry considered is shown in Figure 6.
Several different mounting techniques have been used to attach clip strain
gages to free propellant surfaces, including direct bonding to the pro-
pellant surface with an adhesive, suspension upon pins attached in various
ways to the propellant surface (as in Figure 2 and Figure 7), and combinations
of pins and adhesive bonds. For the purpose of this analysis, only the
mounting techniques similar to those of Figures 2 and 7 were considered.
The principal reason for this restriction is that other common mounting
techniques, which constrain the "feet" of the strain gage to zero rotation,
greatly increase the stiffness of the gage.

w=0.125

TOP VIEW

STRAIN GAGES

L

$(R_i)_1$

t

H

δ_X

$(R_i)_2$

δ_X

L_o

SIDE VIEW
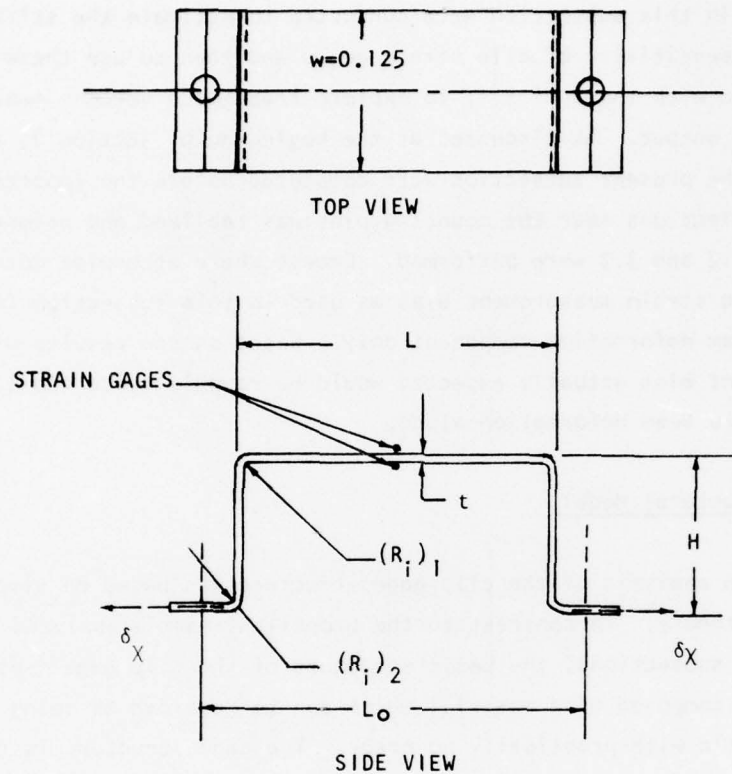
PARAMETERS USED IN ANALYSIS:

L_o ≈ VARIABLE (0.400 in FOR BASELINE)
L ≈ 0.256''
H ≈ VARIABLE (0.131 in FOR BASELINE)
t ≈ VARIABLE (0.006 in FOR BASELINE)
R_{i_1} ≈ VARIABLE
R_{i_2} ≈ VARIABLE
(0 FOR BASELINE)

Figure 28. Clip Gage Geometry Used in Deflection Analysis

-78-

To analyze the gage structure, it was divided into the four free bodies shown in Figure 29. The deflection equations for each free body were written out and the resulting total deflection and rotation at points A, B, C, and D were found by superposition. The actual calculations were performed using a calculator program written with subroutines for straight and curved beams and the appropriate logic for calculating beam dimensions and applied loads from the overall gage geometry. The basic calculation determines gage deflection for the unit load applied at point D (Figure 29). A subsequent calculation determines the force P_o required to obtain a strain of 10 percent over the gage length L_o.

The straight beam sections of Figure 29 are each treated as cantilevered beams with no correction for "wide beam" Poisson effect (a check was made to verify that this effect was negligible). The curved beams are treated as curved cantilevered beams with the neutral surface halfway between the inner and outer radii of the beam; the Poisson effect was again ignored. (These modeling assumptions probably cause noticeable error in the curved beam deflection itself; however, the deflections contributed by the curved beams are small relative to the total deflection, and the relative error in the total deflection is assumed to be negligible.) The "fixed" support for each cantilever beam is located at the end nearest the origin of coordinates in Figure 29. The deflection calculations are carried out first for the horizontal beam anchored at the origin of coordinates (Figure 29), producing the calculated vertical, horizontal, and rotational deflections at point A. These deflections are then considered as a motion of the "fixed" support of the curved beam AB; the rigid-body motion of the curved beam corresponding to the motion of the support plus the deflections of the curved beam are combined to determine the vertical, horizontal, and rotational motion of point B. This procedure is continued until the motion of point D is deter- mined.
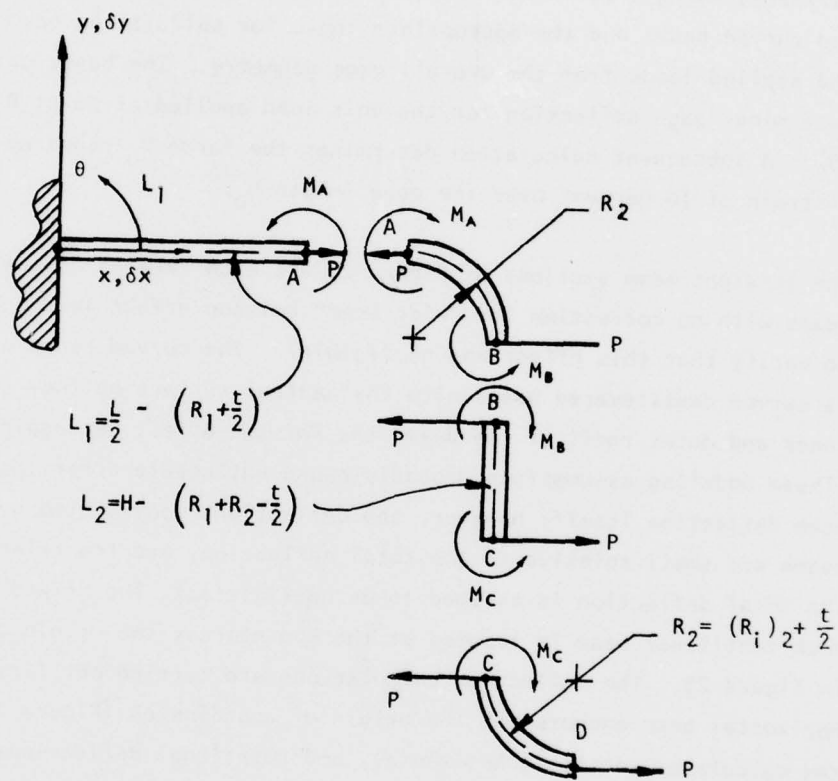
Figure 29.   Free Body System for the Clip Strain Gage

3.4.2   Analysis Results.

The results of the clip gage analyses using the model described above are discussed in the following subsections.

3.4.2.1   Effects of Gage Geometry on Stiffness and Sensitivity.

Figure 30 shows the variation of the parameter P_o (force at 10 percent gage strain) with clip gage height. Figure 31 shows the effect of changes in clip gage height on a measure of the gage output called the relative sensitivity, defined as the ratio of strain in the clip gage center section to strain in the sample gage length L_o. Figures 30 and 31 show that both the gage stiffness and relative output increase rapidly as the height decreases. These figures also show that changes in radius of the corner bends in the clip gage structure have only a minor impact on stiffness and output. It is also apparent from the two figures that changes in height and bend radius tend to preserve a direct relationship between output and gage stiffness: a decrease in stiffness is obtained at the expense of a reduction in gage output for a given strain. Finally, comparison of Figures 30 and 31 shows that a reduction in the thickness of the clip gage from 0.006 inches to 0.004 inches is predicted to change the stiffness much more than it changes the output (this is a highly desirable result). These qualitative observations provided the incentive to investigate the trade-offs between gage sensitivity and measurement bias (produced by the clip gage stiffness) which can be realized through changes in clip gage configuration.

Before examining output/accuracy tradeoffs, however, the specific results shown in Figures 30 and 31 for the "baseline configuration" will be discussed. The baseline configuration corresponds to Thiokol's Prototype Gage No. 1 and Prototype Gage No. 2 (Reference 9). These two prototype gages were actually successive modifications of a clip strain gage provided by Konigsberg Instruments, Inc. for use in the Simulated Air Launch Environment (SALE) program (AFRPL Contract F04611-73-C-0015). This particular
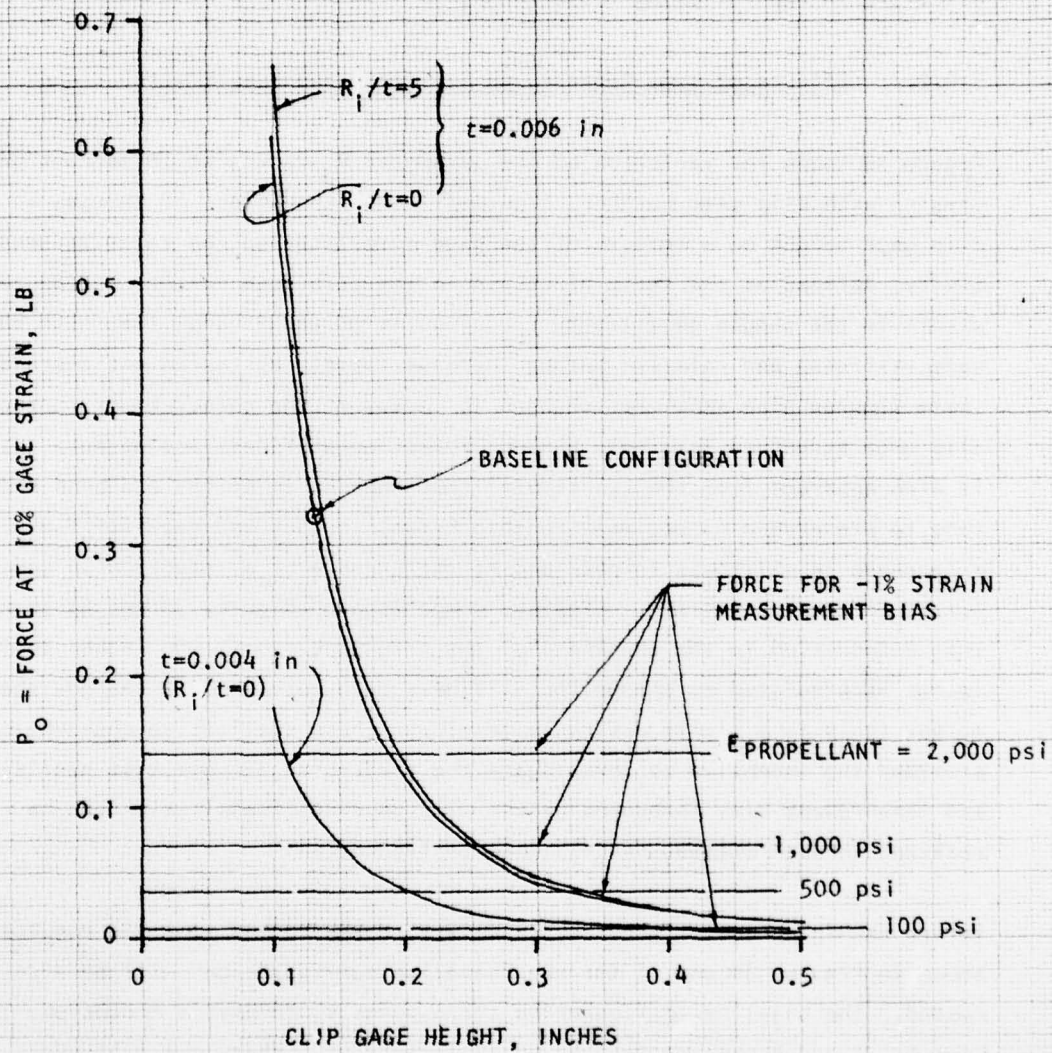
-81-

Figure 30. Effects of Variations in Clip Gage Geometry on Resisting Force at 10% Gage Strain
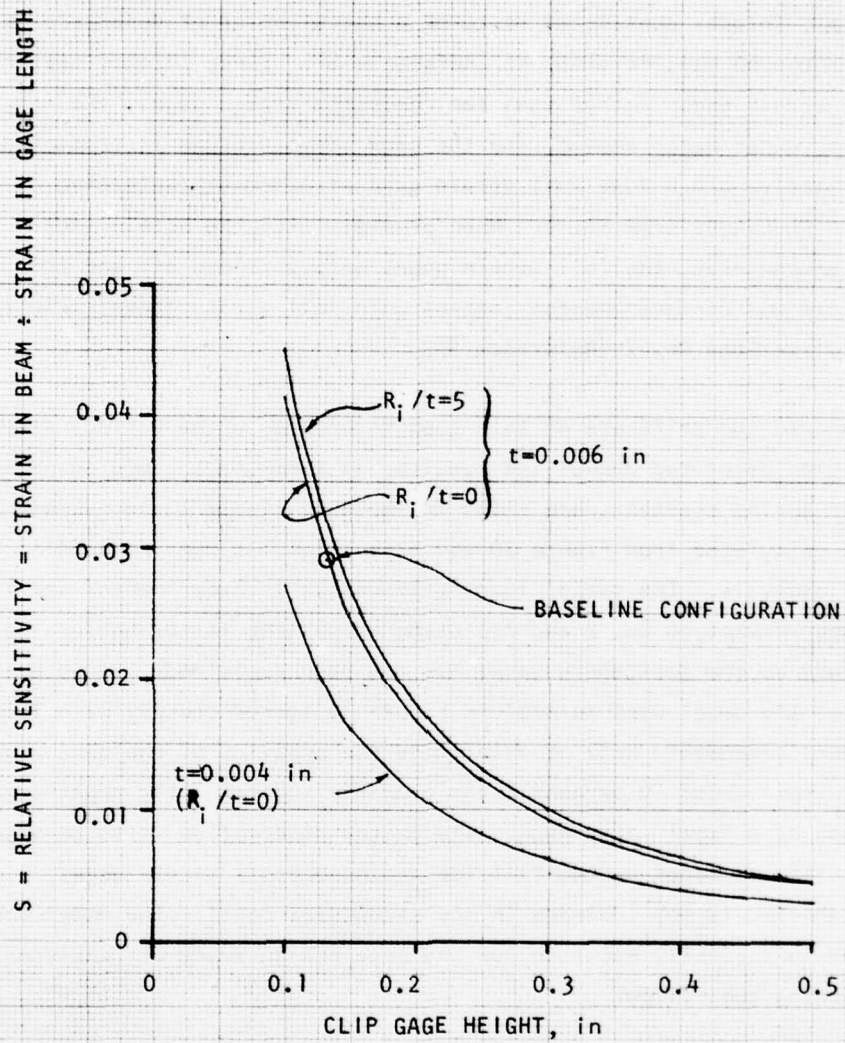
Figure 31. Effects of Variations in Clip Gage Geometry on Relative Gage Sensitivity.

clip gage was not used in the SALE program because of damage which rendered
the semiconductor strain gage bridge inoperative. Although the gage was
nonfunctional, Thiokol considered it to be a useful point of departure for
their own prototype gage development (Reference 8). Since Thiokol preferred
to use foil strain gages rather than semiconductor strain gages, the original
semiconductor gages were removed, and the gage structure was instrumented
with a four-active-arm bridge foil strain gage arrangement (Reference 8),
resulting in Prototype Gage No. 1. When problems with the strain gage
bonds were encountered, the foil strain gages were stripped off and the
gage structure was re-instrumented (again) with foil strain gages, result-
ing in Prototype Gage No. 2 (Reference 9).

Thiokol measured the stiffness of this gage structure in the various stages
of modification described above; the results, in terms of a computed gage
stiffness or spring constant, are shown in Table 1. Table 1 also shows
stiffnesses calculated from Figure 30 and from Thiokol's own independent
beam-theory analysis. The rather large differences in experimental stiff-
nesses between Prototype No. 2 and Prototype No. 1 (the latter having the
same stiffness as the Konigsberg gage) has not been explained. It is evident,
however, that the model used to produce Figure 30 agrees closely with Thiokol's
analysis, does reasonably well at predicting the behavior of the bare gage
structure (within about 10 percent), and probably substantially under-predicts
the stiffness of a "real" clip gage. The latter observation is to be expected,
since the stiffness added by the foil (or semiconductor) strain gages, wires,
and epoxy adhesive is not included in the structural model. The model does
appear to be sufficiently accurate for the gage design trade-off analyses
of the following subsection.

3.4.2.2   Sensitivity Versus Measurement Bias.

The incentive for seeking improvement in the measurement bias is readily
apparent from Figure 24 (3.3.1), which predicts a very large negative bias,
even if the effect of local deflections of the mounting pins is ignored.
Since Thiokol was using metal foil strain gages (which have a small gage

-84-

TABLE 1. STIFFNESS OF EARLY
THIOKOL PROTOTYPE GAGES (MODIFIED KONIGSBERG GAGE)

NOMENCLATURE	SOURCE OF DATA	CALCULATED STIFFNESS
Original Gage	Thiokol-Measured force at 0.030 inches extension [Reference 8]	10.3 lb/in
Gage Structure Only	Thiokol-Measured force at 0.030 inches extension [Reference 8]	7.3 lb/in
Gage Structure Only	Thiokol-Analytical prediction from beam theory [Reference 8]*	8.0 lb/in
Gage Structure Only	Figure 30*	8.05 lb/in
Prototype Gage No. 1	Thiokol-Measured force at 0.030 inches extension [Reference 6]	10.3 lb/in
Prototype Gage No. 2	Thiokol-Measured force at 0.030 inches extension [Reference 9]	8.0 lb/in

---

*Based on gage length of 0.400 inches

factor compared to semiconductor strain gages), it was apparent that the sacrifice in output to achieve decreased gage stiffness (hence decreased measurement bias) must be minimized. The trade-off studies discussed below were therefore undertaken to acquire the insight needed to assess and guide Thiokol's attempts to develop clip strain gages and mounting techniques which would allow measurements of acceptable accuracy for the purposes of the Improved Properties program.

Viewed in an overall sense, the problem is simply posed. The strain at the strain gage location must be relatively increased while the overall stiffness of the clip gage is relatively decreased. Optimally, this would be accomplished by making all parts of the transducer except the measurement section as rigid as possible and by maximizing the strain in the measurement section for a given bending stiffness of the measurement section. Given a design concept that accomplsihes these objectives, the bending stiffness of the gage could then be reduced to the desired level (or to the level which produces the minimum acceptable electrical output). A few additional practical considerations would, of course, be present (e.g., elastic instability, gage durability in routine handling and use, and vibration characteristics under dynamic loads).

Rather than attempting to provide this "ultimate solution", however, it was considered more practical to observe the limitations imposed by Thiokol on their experimental development. These were, in essence:

(a) Retain the same (gage structure) material;
(b) Retain the foil strain gages (as opposed to semiconductor gages);
(c) Keep the gage "simple to manufacture."

Three potential techniques for reducing the gage measurement bias are explored in Figure 32: reducing the gage thickness, increasing the gage height, and decreasing the gage length (L_o in Figure 1). The two curves in Figure 32 labeled t = 0.004 and t = 0.006 were obtained by cross plotting
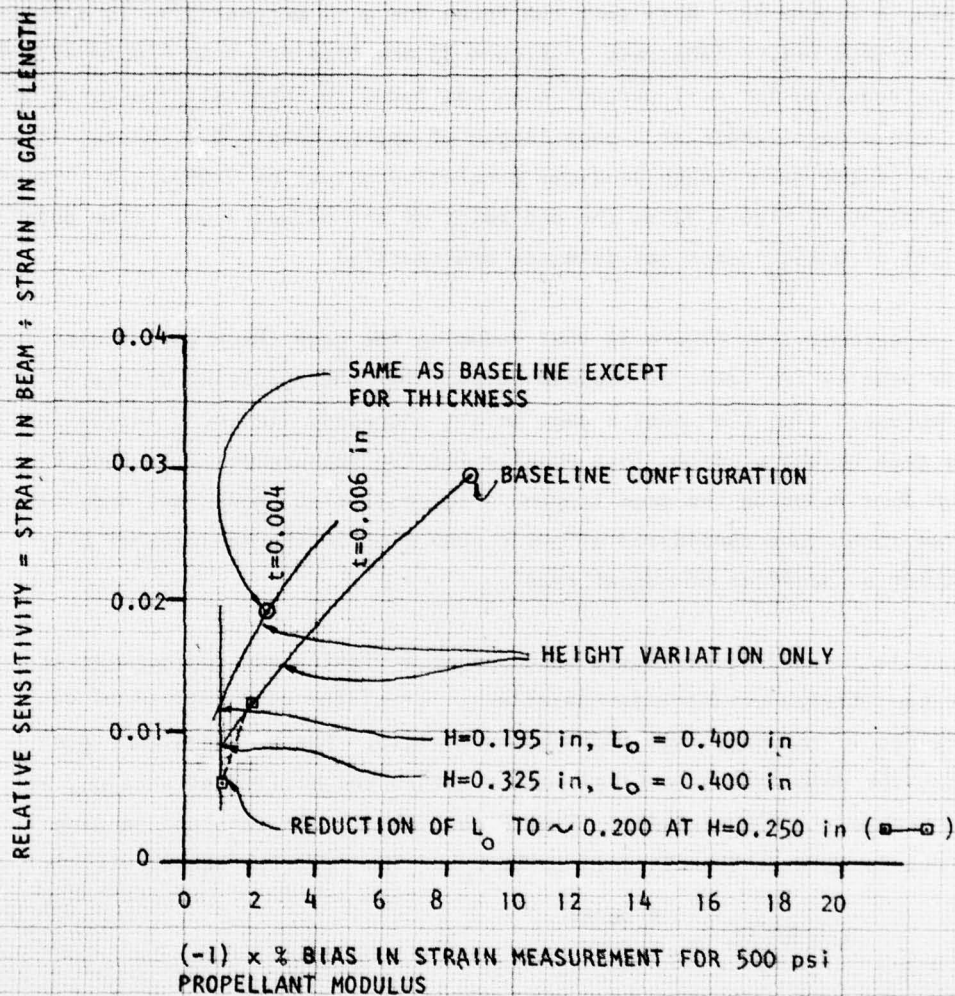
-86-

Figure 32. Possible Changes in Gage Geometry to Reduce Measurement Bias

the relative sensitivity for a given value of H (from Figure 31) against the relative bias (from Figure 3) corresponding to the value of P_o produced by that value of H (from Figure 30). The dashed line representing the effect of a reduction in gage length was obtained in a similar manner, as shown in Figure 33. Note that the force for a -1 percent bias is a function of the gage length (the data in Figure 33 are obtained from Figure 4). The force required for a -1 percent bias was found to intersect the curve of P_o versus gage length at a gage length of approximately 0.2 inches; this value of the gage length produces a relative output of 0.059. This value is plotted in Figure 32 as the end point of the dashed line. (The gage height of 0.250 inches was selected arbitrarily).

It is evident from Figure 32 that reducing the gage thickness results in less penalty (in terms of reduced output) for the resulting decrease in measurement bias than does a gage height increase. In turn, increasing the gage height produces less penalty for the measurement bias reduction than does reducing the gage length. Figure 32 also shows that none of the three techniques considered allows a reduction in the measurement bias without a sacrifice of output level.

It would appear, as discussed above, that a significant improvement in the sensitivity-versus-bias characteristics of the clip gage might be obtained if the gage legs could be made rigid. For a gage with rigid legs, the deformation would all occur within the horizontal section, as illustrated in Figure 34(b). From Figure 34(a), the constant bending moment in this section is seen to be $P_o h$. The relative sensitivity is

$$S = \frac{Mc/EI}{\varepsilon_o} = \frac{P_o hc/EI}{\varepsilon_o} .$$

From Figure 34(b), the strain (for small values of θ) in the gage length L_o is
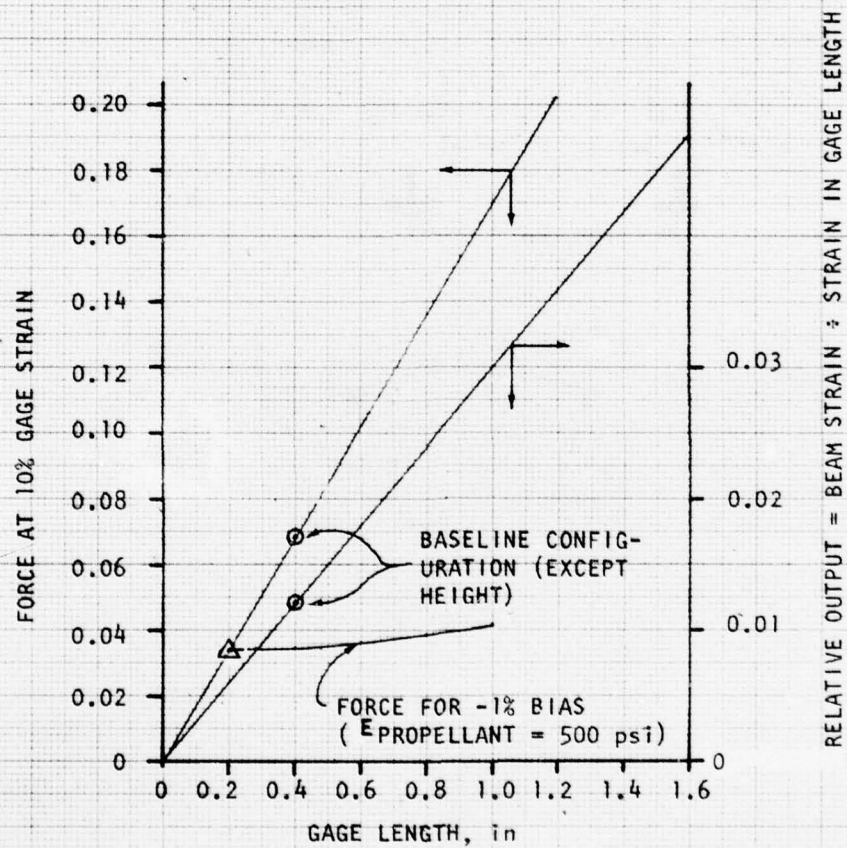
$$\varepsilon_o = \frac{2h\theta}{L_o}$$

-88-

Figure 33. Effects of Changes in Gage Length on Gage
Resisting Force and Relative Sensitivity
(Gage Height 0.250 in)

(a)

(b)
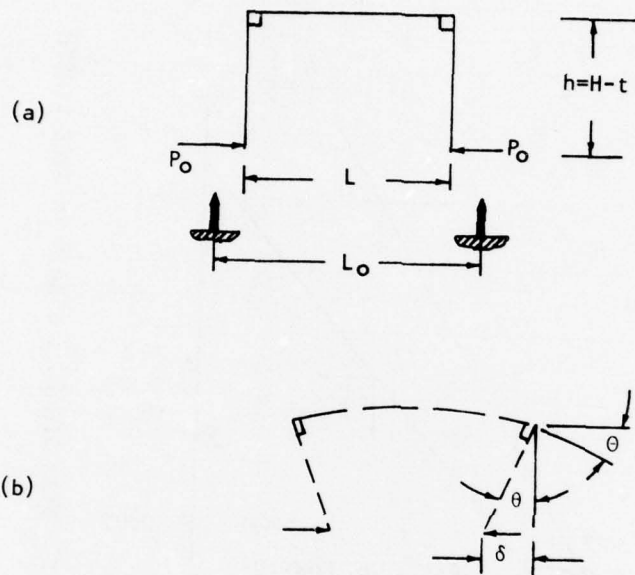
Figure 34. Gage with Rigid Legs

(a) Geometry;
(b) Deformed Shape

The deflection equation for the beam yields

$$\theta = \frac{ML}{2EI}$$

resulting in

$$\varepsilon_o = \frac{P_o h^2 L}{EIL_o}$$

so

$$S = \left(\frac{P_o hc}{EI}\right) \left(\frac{EI\, L_o}{P_o h^2 L}\right) = \frac{CL_o}{hL} = \frac{t}{2h}\ \frac{L_o}{L}$$

and

$$P_o = \frac{S(EI)\varepsilon_o}{hc} = \left(\frac{C L_o}{hL}\right) = \frac{EI\varepsilon_o}{hc} = \frac{L_o}{L}\left(\frac{E\ \varepsilon_o}{h^2}\right) I$$

or

$$P_o = \frac{L_o}{L}\ \frac{E}{h^2}\left(\frac{wt^3}{12}\right)\varepsilon_o = \left(\frac{L_o}{L}\right)(E)\frac{wt^3}{120h^2}\ \varepsilon_o.$$

If we take $\hat{t} = t/t_{baseline}$, $\hat{h} = h/h_{baseline}$, etc., then

$$\hat{S} = \frac{\hat{t}}{\hat{h}\,\hat{L}}\ \hat{L}_o \tag{75}$$

$$\hat{P}_o = \frac{\hat{w}\,(\hat{t})^3}{(\hat{h})^2\,\hat{L}}\ \hat{L}_o\ \hat{E} \tag{76}$$

and

$$\hat{S}/\hat{P}_o = \frac{\hat{h}}{\hat{w}(\hat{t})^2\hat{E}} \tag{77}$$

Equations (75) and (76) were used[1] to calculate the relative sensitivity-versus-bias curve for a rigid-leg gage having the dimensions and modulus of the baseline gage. The result is compared in Figure 35 with the sensitivity-bias characteristics of the baseline gage. As expected, the rigid-leg gage provides a higher relative sensitivity for a given measurement bias but is stiffer than a flexible-leg gage of the same dimensions. Thiokol produced a prototype gage which approached the ideal rigid-leg configuration. This gage, which was the final prototype discussed in 3.3.1, had a measured spring constant of 2.56 lb/in. This prototype was designated the "stiff-leg gage"; its configuration was basically as shown in Figure 36. Calculations show that the behavior of the stiff-leg gage was intermediate between a rigid-leg gage and a flexible-leg gage with the same dimensions, and that the stiff-leg gage provided a substantial reduction in measurement bias with only a small reduction in sensitivity compared to the baseline gage. However, the measurement bias of nearly 3 percent (neglecting bias due to local deformation, which will raise the total bias to more than 5 percent) is still far too high. (See Figure 37.)

Equations (75) and (76) were used to calculate trajectories of $\hat{S}$ versus $\hat{P}_o$ with specific parameters allowed to vary while all other parameters were held fixed. Examining the results, shown in Figure 38, demonstrates the sensitivity of a rigid-leg clip gage's output (for a given value of P_o) to the gage design parameters. It is apparent in Figure 38 that varying the gage width ($\hat{w}$) or the elastic modulus ($\hat{E}$) is the most efficient way to decrease the value of P_o (and hence the gage bias due to gage-sample interaction). Note, however, that interactive effects between the design parameters could provide more efficient combined parameter changes to reduce $\hat{P}_o$. (For instance, a decrease in $\hat{w}$ together with a decrease in L would reduce $\hat{P}_o$ while increasing $\hat{S}$.) These rigid-leg gage results provide upper bounds on $\hat{S}$-versus-$\hat{P}_o$ trends for flexible-leg gages, as illustrated by the solid (triangle and square) symbols in

---

1. The bias was determined from P_o using the techniques described in 3.3, but the local mounting pin deformation was ignored.
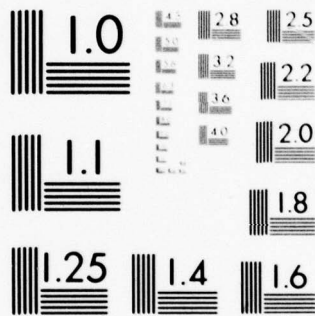
MICROCOPY RESOLUTION TEST CHART
NATIONAL BUREAU OF STANDARDS 1963-A
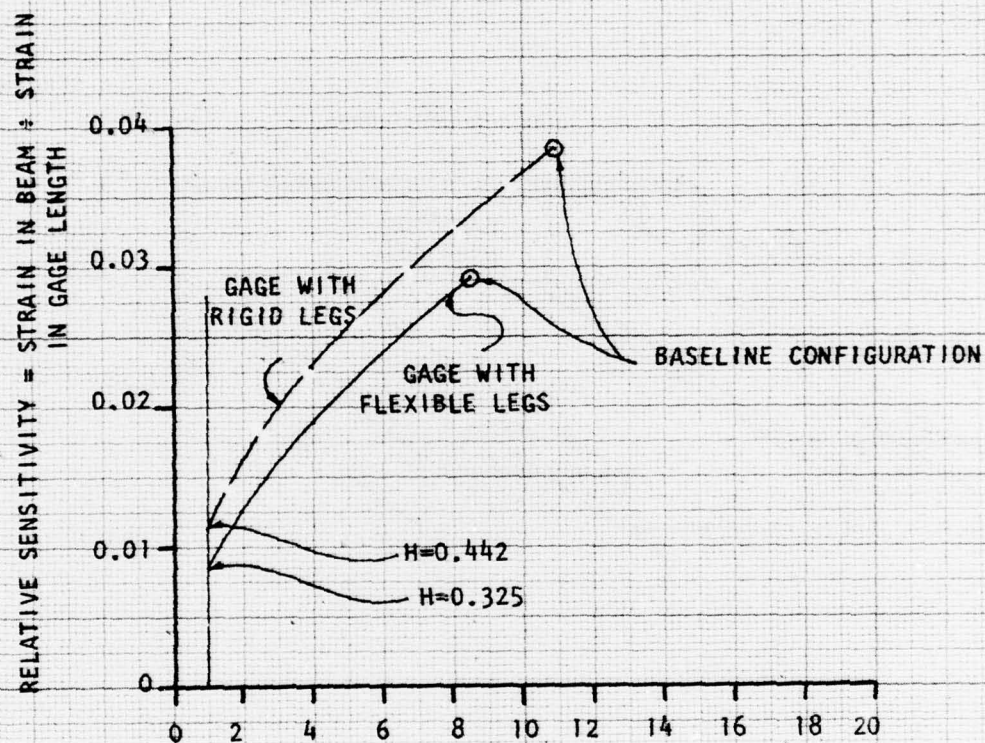
Figure 35. Effect of Changes in Height on Gage Sensitivity and Strain Measurement Bias for the Gaged Specimen of Figure 2.

Figure 36. Thiokol "Stiff-Leg" Gage Configuration

Figure 37. Comparison of "Stiff-Leg" Gage (Sensitivity and Bias) with Baseline Gage

Figure 38. Sensitivity-vs-Stiffness Tradeoffs for Various Design Changes (Gage with Rigid Legs).

*NOTE: Solid Symbols are for Gages with Non-Rigid Legs and Same "R" as Corresponding Rigid Gage

Figure 38, which were determined from Figures 30 and 31. Note that the corresponding rigid-leg and flexible-leg points lie on lines of constant $\hat{S}/\hat{P}_o$; this is always true for gages with the same center section geometry and materials.
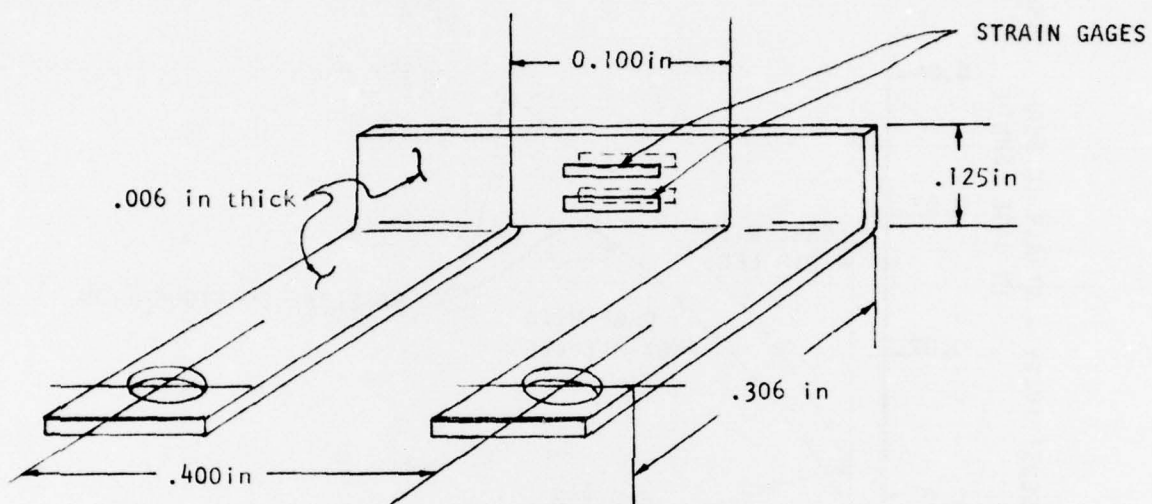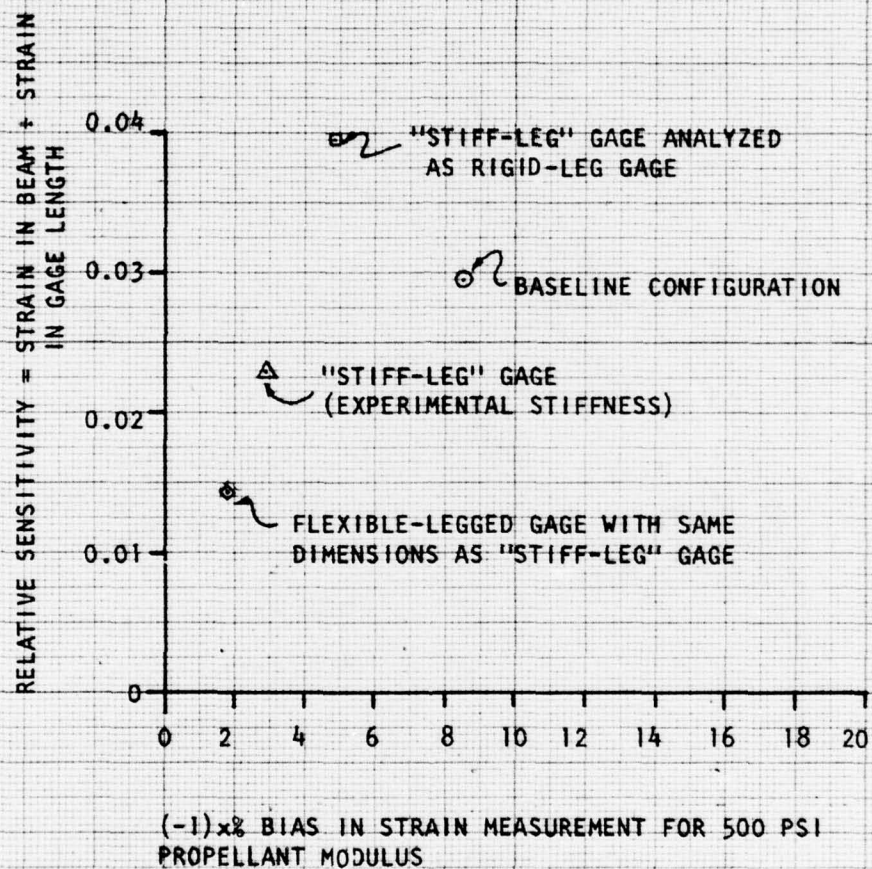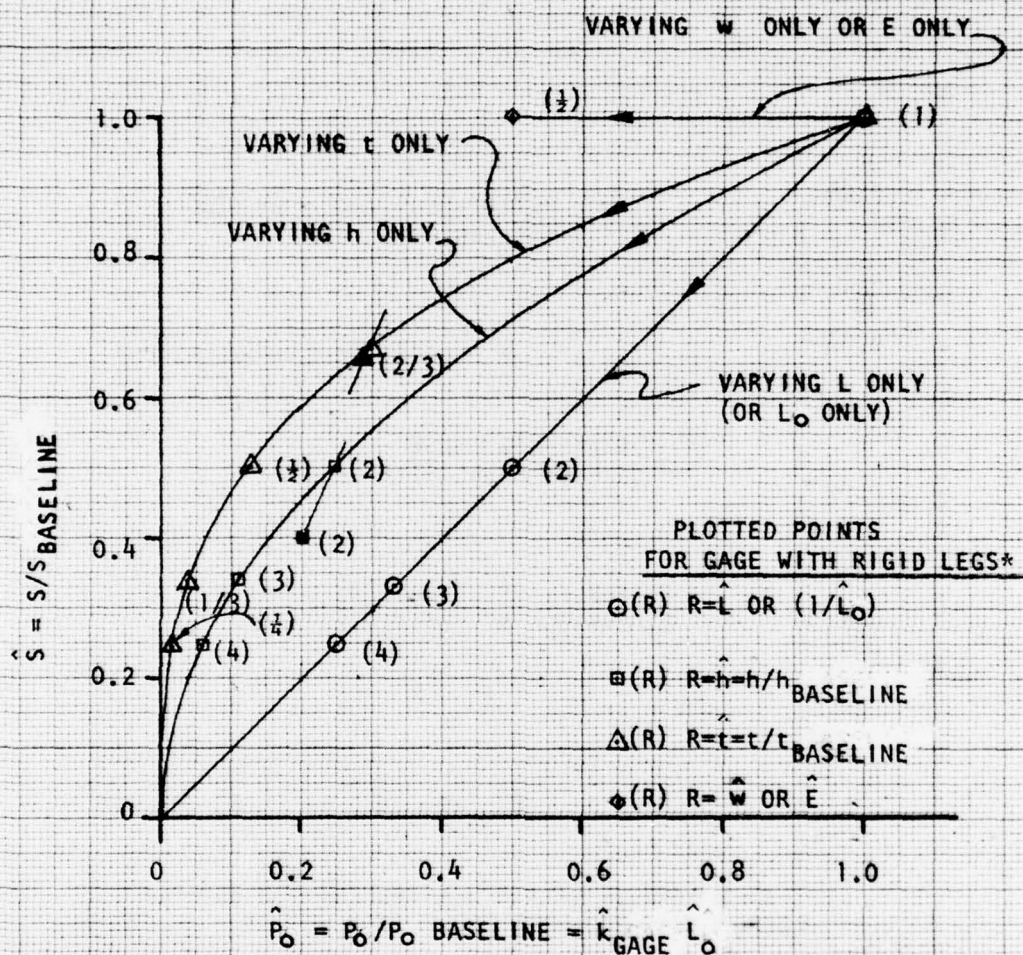
Based on these results from the idealized rigid-leg gage model, a number of potentially achievable changes to the gage structure were analyzed using the realistic model to provide an idea of the potential for improvement. The results are presented as curves A through F in Figure 39. (In considering the impact of these results, recall that the strain measurement bias shown neglects local pin deformation, so that the actual total bias would be about twice that shown. Also, the bias at 100 psi modulus would be nearly five times the bias at 500 psi modulus, while propellant modulus values greater than 500 psi would reduce the bias in a roughly proportional relationship). Curve A shows the effects obtainable by increasing the height of the baseline gage, holding all other parameters constant. Curve B shows the effects obtainable by changing the gage material to a titanium alloy and duplicating the geometries considered in curve A; curves C and D show the effects obtainable with an aluminum alloy and a magnesium alloy, considering the same geometries as in curve A. Note (from Table 2) that the range of moduli available in this group of materials is from 18.5×10^6 psi down to 6.5×10^6 psi. Further improvements are shown when the foil thickness is reduced to .004 inch and the width to 0.100 (curves E for the original beryllium bronze material and F for the magnesium alloy). Finally, the effects of changing to the magnesium alloy, adopting Thiokol's "stiff-leg" configuration, reducing the thickness to .004 inch and reducing the width and length of the measuring section to 0.100 inch are shown by curve G.[2] These changes are probably achievable, although the feasibility of using magnesium alloy for the gage may be questionable (titanium and aluminum alloys have been used in propellant stress gages and strain gages respectively).

The conclusion to be derived from Figure 39 is that it is potentially possible to produce a clip strain gage, using foil strain gage sensing elements, with

2. Calculations for curve G used the rigid leg gage model with a stiffness reduction factor (obtained from results shown in Figure 37) of 0.649.
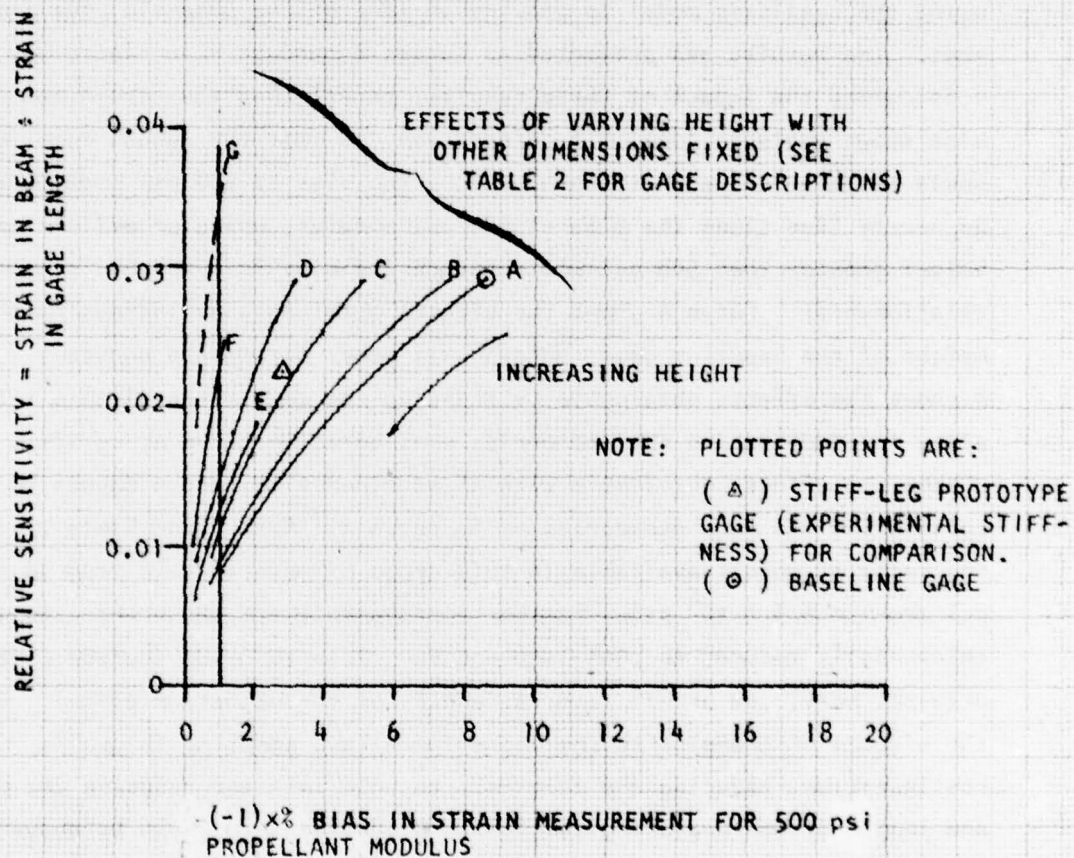
Figure 39. Effects of Gage Material and Geometry on Potential
Clip Gage Performance (Realistic Gages)

TABLE 2. GAGE PARAMETERS USED IN
CALCULATIONS OF FIGURE 39

SYMBOL	MATERIAL	E, psi*	w, in	t, in	L, in	$H_{1\%}^{**}$, in
A	BERYLLIUM BRONZE	18.5×10^6	.125	.006	.256	.175
B	TITANIUM ALLOY RC-130A	16.0×10^6	.125	.006	.256	.300
C	ALUMINUM ALLOY 24S-T6	10.5×10^6	.125	.006	.256	.288
D	MAGNESIUM ALLOY AZ31X	6.5×10^6	.125	.006	.256	.212
E	BERYLLIUM BRONZE	18.5×10^6	.100	.004	.256	.181
F	MAGNESIUM ALLOY AZ31X	6.5×10^6	.100	.004	.256	.102
G***	MAGNESIUM ALLOY AZ31X	6.5×10^6	.100	.004	.100	.161

* Data from Reference 10.
** Calculated result.
*** "Stiff-leg" gage treated as rigid-leg gage with stiffness scaled per experimental stiffness of prototype "stiff-leg" gage.

an acceptable output level (comparable to that of the Thiokol stiff-leg
prototype) and a bias of less than 1 percent at a 500 psi propellant modulus,
including local deformation effects. The bias at 100 psi propellant modulus
would be at a reasonable level of about 5 percent. The primary area of
doubt would be the usability of magnesium alloy or another low-modulus
material for the clip gage structure.

Another consideration for clip gage improvement is the use of semiconductor
strain gages instead of foil strain gages. Semiconductor gages would allow
the use of much lower values of relative sensitivity since they have up to
75 times higher gage factor than the foil gages. However, examination of
Figure 30 suggests that attempting to utilize this approach to reduce the
bias by increasing the height of a given gage structure would result in
rather long legs before much advantage is gained. This is borne out by
calculations: extending curve E (Figure 39) to a relative sensitivity
of .0037 reduces the relative bias (including local deformation effects)
to about 0.2 percent at 500 psi propellant modulus or roughly 1.0 percent
at 100 psi propellant modulus. However, the required leg length is 0.415
inch and the structure would be somewhat flimsy. The same bias level with
the gage design approach of curve G requires a leg length of 0.510 inch.
These clip gages would probably be within the limits of practicality.

3.5   Further Analysis.

The analyses in this subsection were conducted to investigate the effect of clip gage prestrain on strain measurement bias; to incorporate time-dependent propellant modulus into the bias calculations; and, finally, to compare the time-dependent results with Thiokol's experimental measurements of gage response to evaluate the theoretical calculations.

3.5.1   Effect of Gage Prestrain.

In all earlier analysis in this report, the clip gages were assumed to be attached to the sample or to the mounting pins in such a way that the gage would be in an undeformed state when the propellant sample strain over the gage length was zero. That is, it was assumed that the gage was mounted without prestrain. In actual use, however, the clip gages are almost always mounted in a prestrained condition so that reversal of the direction of the force on the strain gage does not occur. This practice avoids certain mechanical problems in the use of the gages.

Prestrain is obtained by a mismatch of dimensions between the gage mounting points (e.g., holes in the gage feet) and the sample mounting points (e.g., the mounting pins) which define the gage length for the strain measurements. For the purposes of this analysis, assume that the mounting pins are implanted in the sample a distance L_o (the nominal gage length) apart, but that the mounting holes in the gage feet are purposely spaced at a distance $L_o - d$ apart. The gage will therefore be in a prestrained condition when assembled with the propellant sample and mounting pins as in Figure 7. If the sample and pins were infinitely stiff, the prestrain would be

$$(\varepsilon_{pre})_{nominal} = \frac{d}{L_o}$$

where the subscript "pre" indicates "prestrain". Since the sample and pins are not infinitely stiff, both the sample and the gage will deform by an

amount equal to $(\Delta\epsilon_{pre})(L_o)$ because of the force required to prestrain the gage. This prestrain force is

$$P_{pre} = k_g [d - (\Delta\epsilon_{pre}) L_o]$$

where k_g is the gage stiffness or spring constant. However, the preload force is also given by

$$P_{pre} = k_s (\Delta\epsilon_{pre}) L_o.$$

Solving for P_{pre} and ϵ_{pre},

$$P_{pre} = \frac{k_s k_g d}{k_s + k_g}$$

$$\Delta\epsilon_{pre} = \frac{k_g d}{(k_s + k_g) L_o}$$

Recognizing that propellant is viscoelastic, k_s will be different for a long-term loading situation (prestrain) than for a short term loading of the sample. Define the stiffness for prestrain as $(k_s)_{pre}$. Then

$$P_{pre} = \frac{(k_s)_{pre} k_g d}{(k_s)_{pre} + k_g}$$

and

$$(\Delta\epsilon)_{pre} = \frac{k_g d}{[(k_s)_{pre} + k_g] L_o}$$

The experimental practice is to assign a strain measurement of zero to the

-102-

gage output at this condition. Therefore when a strain change $\Delta\varepsilon_{gage}$ from this condition occurs, the measured strain value is

$$\varepsilon_{meas} = \Delta\varepsilon_{gage} = \varepsilon_{gage} - \varepsilon_{gage}\Big|_{pre}$$

$$= \varepsilon_{gage} - \left[\frac{d}{L_o} - (\Delta\varepsilon_z)_{pre}\right]$$

where ε_{gage} is the actual strain $(\Delta L_o/L_o)$ of the gage. The clip gage reaction force at this condition is

$$P = P_{pre} + (\Delta P)_{\varepsilon_{meas}} = P_{pre} + k_g (\Delta\varepsilon_{meas}) L_o$$

The total "bias" strain produced by P is

$$\Delta\varepsilon_z = (\Delta\varepsilon_z)_{pre} + (\Delta\varepsilon_z)_{meas} = \varepsilon_{sample} - \varepsilon_{gage}$$

or

$$\Delta\varepsilon_z = \varepsilon_{sample} - \Delta\varepsilon_{gage} + \left[\frac{d}{L_o} - (\Delta\varepsilon_z)_{pre}\right]$$

so

$$\Delta\varepsilon_{z_{meas}} = \Delta\varepsilon_{sample} - \Delta\varepsilon_{gage} \equiv \Delta\varepsilon_{sample} - \Delta(\varepsilon_{meas})$$

since the term in brackets cancels out. Substituting for $\Delta(\varepsilon_{meas})$,

$$\Delta\varepsilon_{z_{meas}} = \frac{P}{k_s L_o} = \frac{k_g (\Delta\varepsilon_{meas})}{k_s}$$

or

$$\Delta\varepsilon_{z_{meas}} = \frac{k_g}{K_s} \left[\varepsilon_{sample} - \Delta\varepsilon_{z_{meas}}\right]$$

or

$$\Delta\varepsilon_{z_{meas}} = \frac{k_g}{k_s + k_g} \cdot \varepsilon_{sample}$$

Now the gage stiffness in the terminology of 3.1 is

$$k_g = \frac{P_o}{\varepsilon_o L_o} \equiv \frac{\Delta P_o}{\Delta\varepsilon_o L_o}$$

and the sample stiffness is (for the geometry of Figure 1)

$$k_s = \frac{E}{14.40 L_o}$$

so the relative measurement bias becomes

$$e_{R\varepsilon_{meas}} = \frac{-[\Delta P_o / (\Delta\varepsilon_o L_o)]}{\frac{E}{14.40 L_o} + \frac{\Delta P_o}{\Delta\varepsilon_o L_o}} = \frac{-14.4 \, \Delta P_o}{\Delta\varepsilon_o E + \Delta P_o} .$$

We are therefore led to the conclusion that prestrain does not affect the measurement bias in the usual method of clip gage usage.[1]

3.5.2 Incorporation of Viscoelastic Propellant Behavior.

All previous analyses in this report have treated the propellant sample as a linear elastic body. Time-dependent effects will now be incorporated into the analytical model by including consideration of viscoelastic propellant response.

Thiokol's characterization of the TP-H8260 propellant used in clip gage experiments under the Improved Properties program provided the relaxation modulus data shown in Figure 40. The calculator programs discussed in

———————————

1. However, a viscoelastic analysis shows short term effects (see Figure 49).
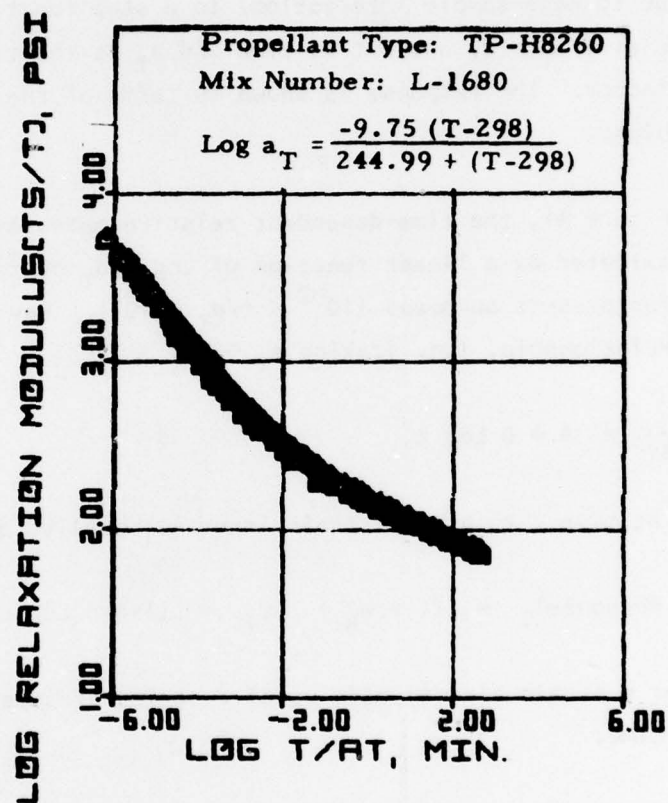
-104-

Figure 40. Thiokol Propellant Relaxation Modulus Data (Ref. 11)

3.3.1 were used to calculate the strain measurement bias for the Thiokol stiff-leg gage (described in Figure 36) at selected time intervals, using the stress relaxation modulus given at each time by Figure 40. These calculations included both the bias due to sample beam deformation and the bias due to local deformation of the mounting pins. Calculations were carried out for two loading eccentricities: e = 0 and e = 0.050 in. The results, shown in Figure 41, give the time-dependent response of the clip gage (due to gage-sample interaction) to a step function strain applied to the sample at $t/a_T = 0$, where t is time and a_T is the time-temperature (WLF) shift factor. The response is shown in terms of the relative strain measurement bias.

As shown in Figure 41, the time-dependent relative measurement bias is closely approximated by a linear function of Log t/a_T over the range of interest for present purposes ($10^{-2} \leq t/a_T \leq 10^2$). Having this approximate relationship, i.e. (taking $a_T \equiv 1$)

$$-e_{R\epsilon} = A + B \text{ Log } t,$$

the response at time t to a step strain input $\Delta\epsilon_i$ applied at time $(t_o)_i$ is

$$(\Delta \text{ Response})_i = (1 + e_{R\epsilon}) \Delta\epsilon_i = (1-A-B \text{ Log } t) \Delta\epsilon_i.$$

Therefore, for a strain history made up of a series of superposed step functions in time,

$$\sum_{i=1}^{n} \Delta \text{ Response} = \sum_{i=1}^{n} \left[1-A-B \text{ Log } (t-t_o)_i\right] \Delta\epsilon_i \, \delta_i \qquad (78)$$

where

$$\delta_i = 1 \text{ for } (t-t_o)_i \geq 1$$
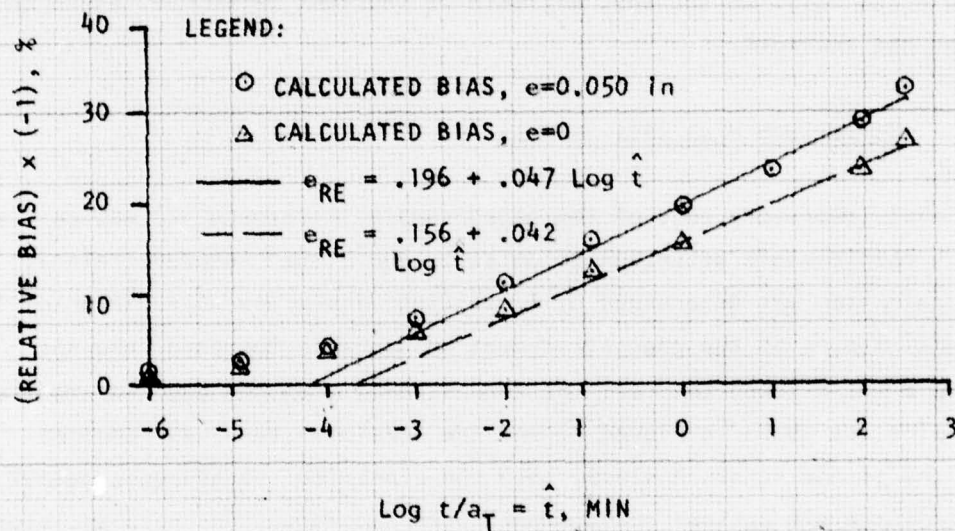
$$\delta_i = 0 \text{ for } (t-t_o)_i < 1$$

-106-

Figure 41. Time-Dependent Response of Thiokol "Stiff-Leg" Gage Using Viscoelastic Propellant Response.

A calculator program was written to carry out the calculation of Equation (78) for a series of five-step functions of arbitrary levels occurring at equal time intervals (response is output at time increments of $(t-t_o)/10$; $(t-t_o)$ is assumed to be equal to five units of time).

Using the calculator program, the response to the applied strain history is shown in Figure 42. This strain history was selected to agree with that used by Thiokol in a laboratory gage calibration test on a gaged uniaxial propellant sample (Reference 12). The strain increments correspond to Thiokol's reported data; the time interval between steps (5 minutes) and the interval between strain application and gage data acquisition (5 minutes) were selected based on the best estimate of the test personnel, since this data was not recorded.

3.5.3   Comparison With Test Results.

The Thiokol laboratory test of the gaged sample (Reference 12) was carried out with considerable attention to detail. The "true" sample strain at each strain step was determined by travelling-microscope observation of the mounting pins at the gage attachment points with the gage removed. The sample was allowed to "rest" at zero strain, then the gage was mounted on the pins (as shown in Figure 7) and the strain history was repeated. During the second strain history, both the electrical strain gage output and the pin-to-pin optical measurements were recorded. The results, plotted in Figures 43 and 44 (solid symbols), were determined by averaging five individual observations of each data point.

Interestingly, two factors which are observable in Figure 43 produced a false sense of security in earlier, less thorough tests. The first is the increased strain in the gage length of the sample; the second is the discrepancy between the gage electrical output and the actual strain imposed on the gage. Both factors produced errors which compensated in part for the inherent bias due to the gage/sample interaction.
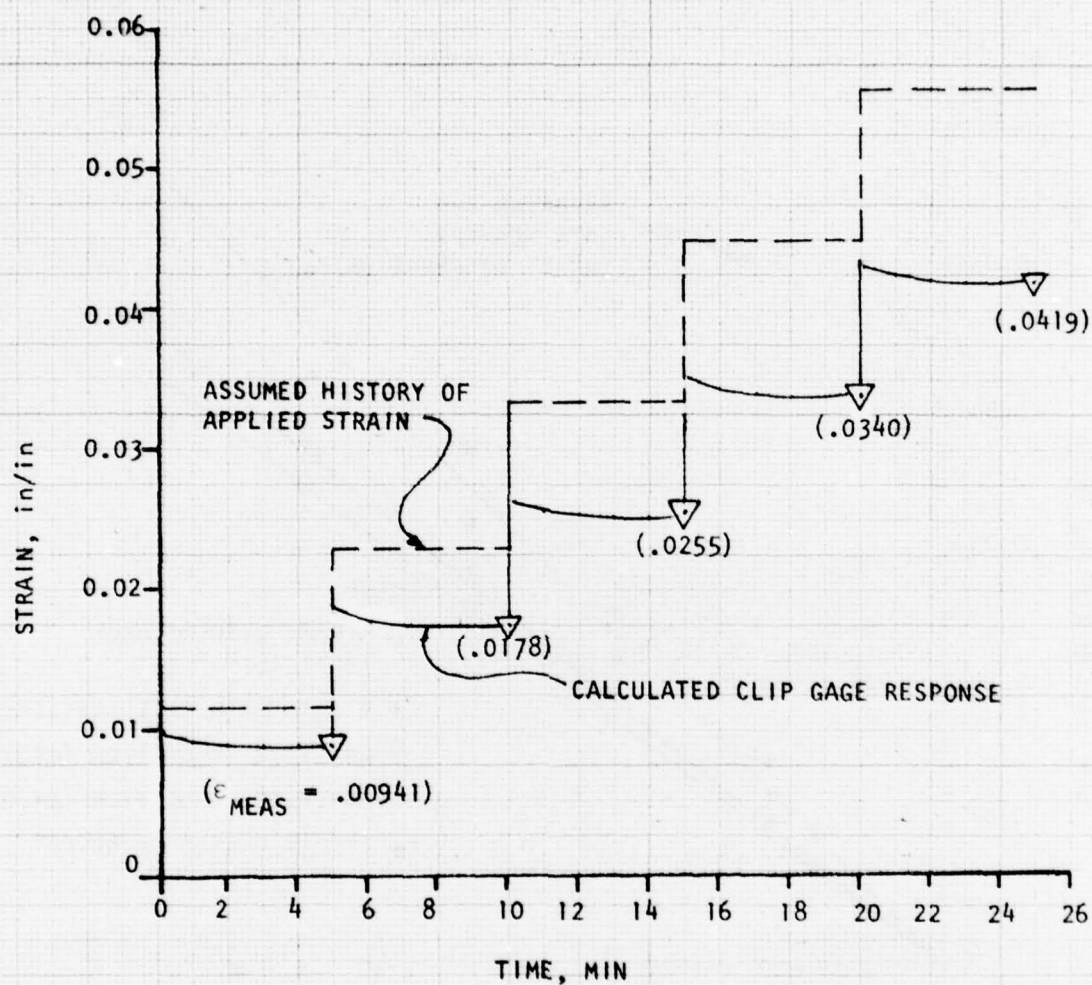
-108-

Figure 42. Time-Dependent Clip Gage Response During Calibration Test (Thiokol "Stiff-Leg" Gage with e=0.050 in).
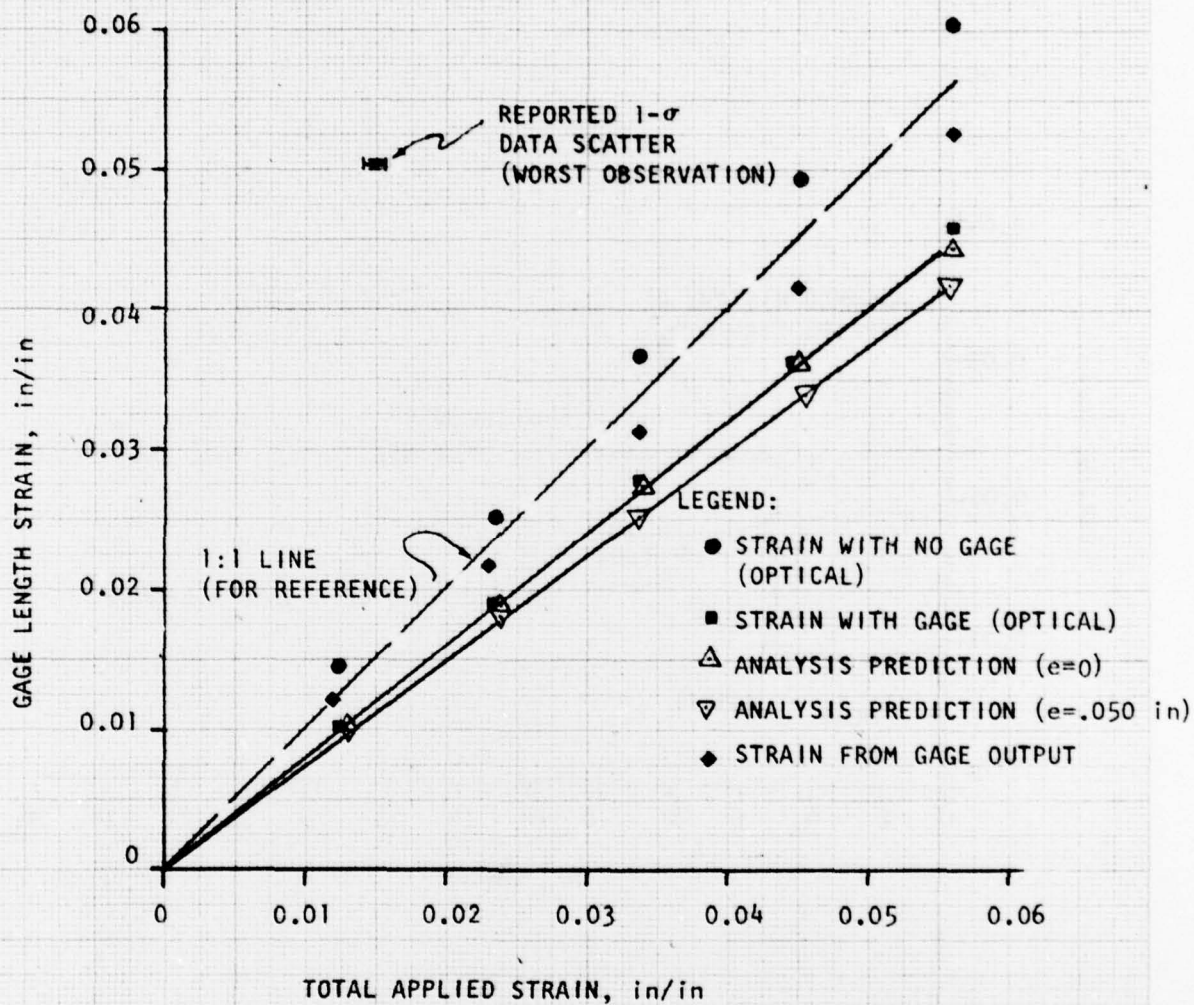
Figure 43. Comparison of Thiokol Calibration Experiment Data
With Analysis Predictions (Driving Strain = Total
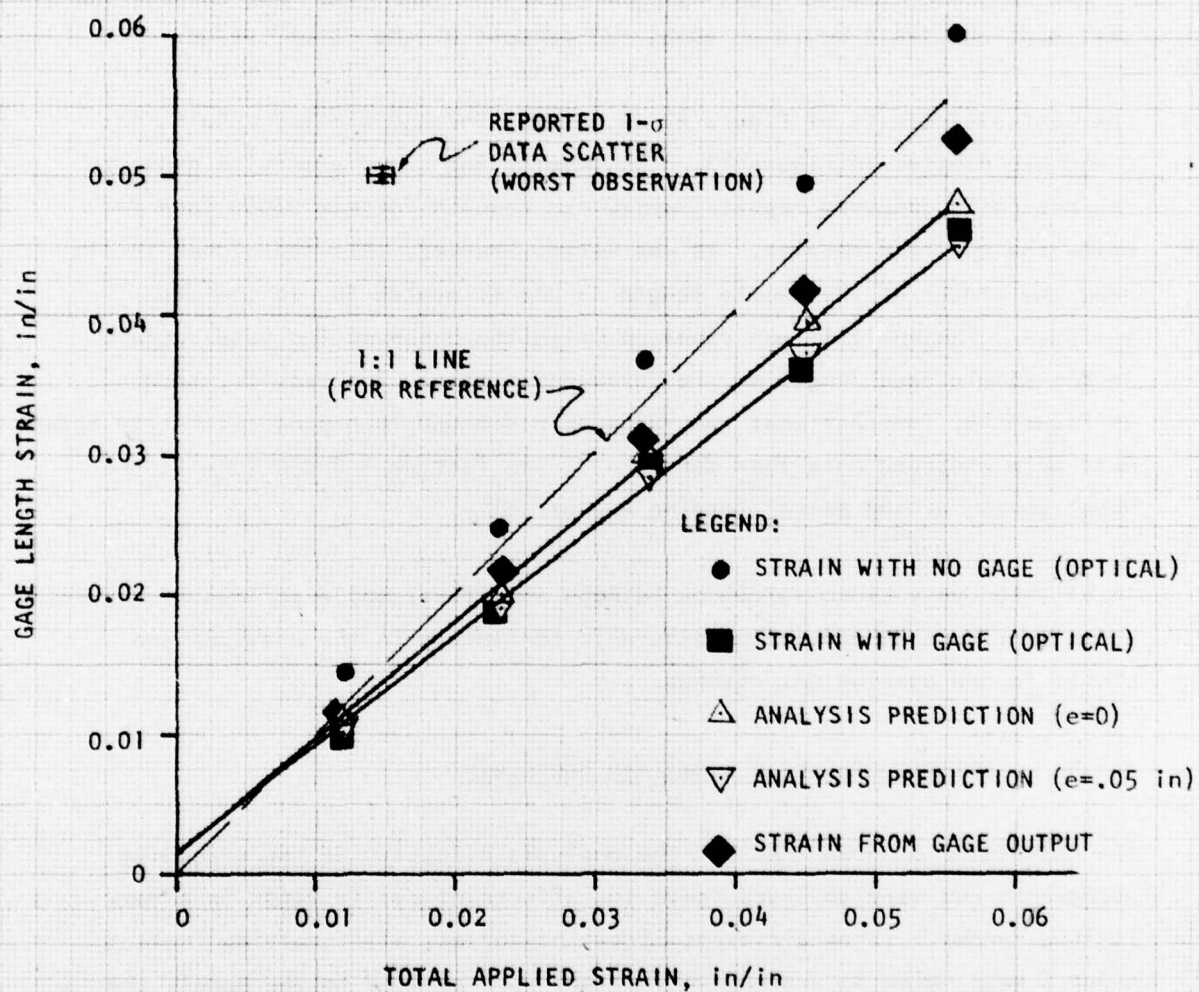Applied Strain) (Ref. 12).

Figure 44. Comparison of Thiokol Calibration Experiment Data With Analysis Predictions (Driving Strain = Gage Length Strain with No Gage) (Ref. 12).

(The error introduced by the increased strain in the gage length was present because this data was not observed in the earlier tests.) To illustrate, ignoring these two factors would lead to an estimate of the measurement bias, at 5.6 percent applied strain, of about -7 percent of the "true" value. Considering the two factors leads to the conclusions that (1) the in-situ calibration of the gage does not agree with its original calibration; and (2) in the absence of this compensating error, the measurement bias at 5.6 percent applied strain would be about -23 percent of the "true" value.

The analysis results of Figure 42 (e = 0.050 in) and similar results for e = 0 are plotted in Figure 43. The results for e = 0 are quite close to the optically observed results, while the results for e = 0.050 inch fall below the observed results. It was noted, however, that the higher strain near the center of the sample length is not accounted for in the gage analysis. The analysis was repeated using the observed (no gage) strain in the sample gage length as the "driving" strain. The results, shown in Figure 44, indicate that the value of e = 0.050 inch produces better agreement with observed data than does e = 0. In fact, e = 0.050 inch is the "best guess" of the actual loading eccentricity.

In all, the very close agreement between analytical and experimental results shown in Figure 44 provide considerable confidence in the analyses and thence in the conclusions reached.

3.5.4   Effects of Cyclic Loads And Prestrain.

The calculator program used for the analysis discussed in the preceding paragraphs was used to investigate the effects of cyclic loads in a very limited manner. Three different strain histories, all involving cycling about a mean value in a stepwise fashion, were applied to the model; the results are shown in Figures 45 to 48. In Figure 46, note that the hysteresis is reduced by selecting a longer interval between application of strain and data acquisition; however, this does not always reduce the measurement bias.
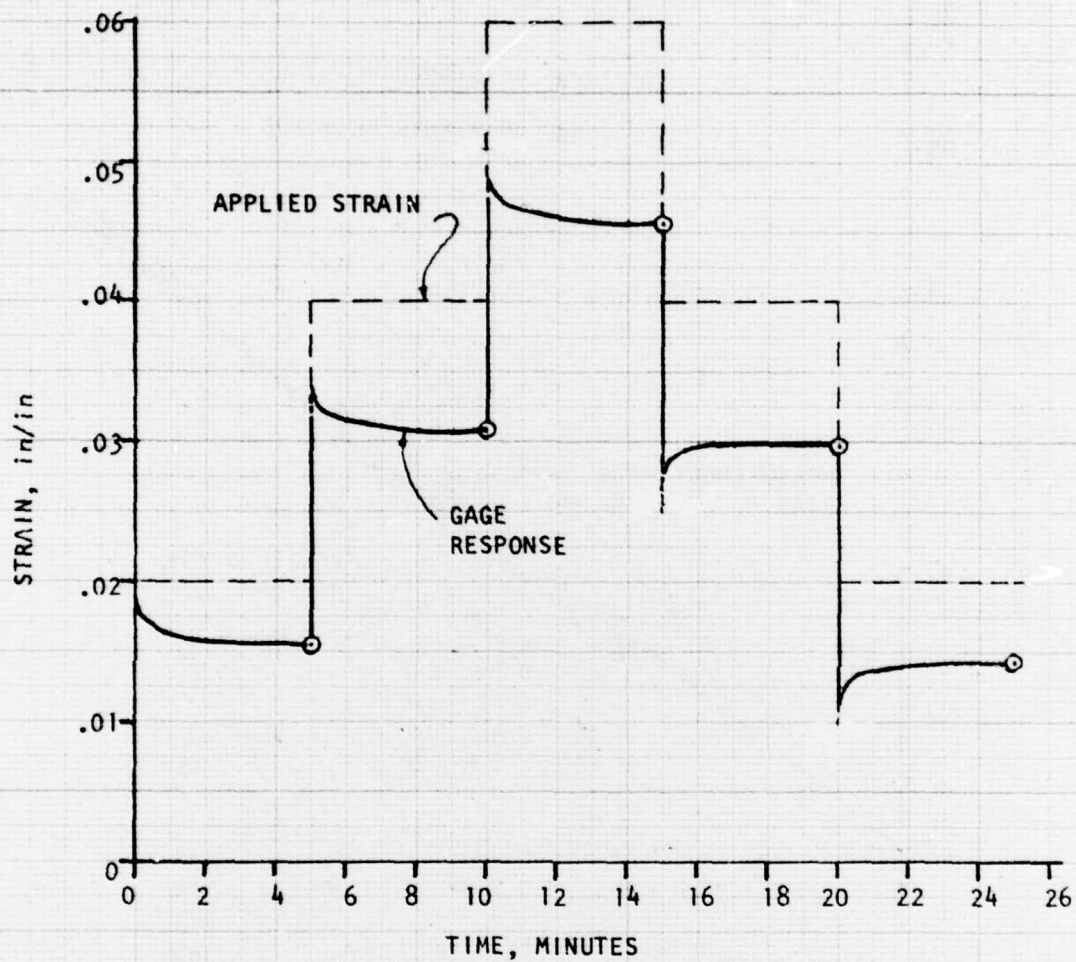
Figure 45. Time-Dependent Response to Varying Strain History No. 1
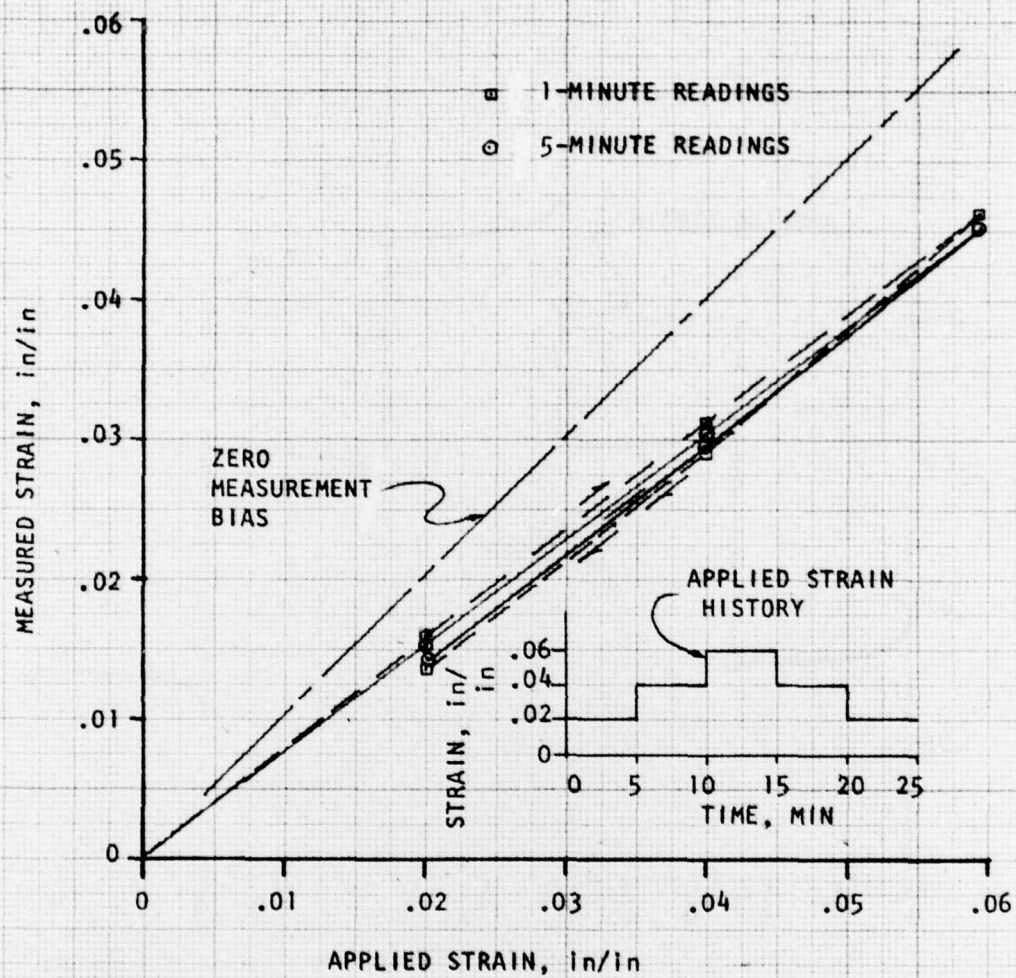
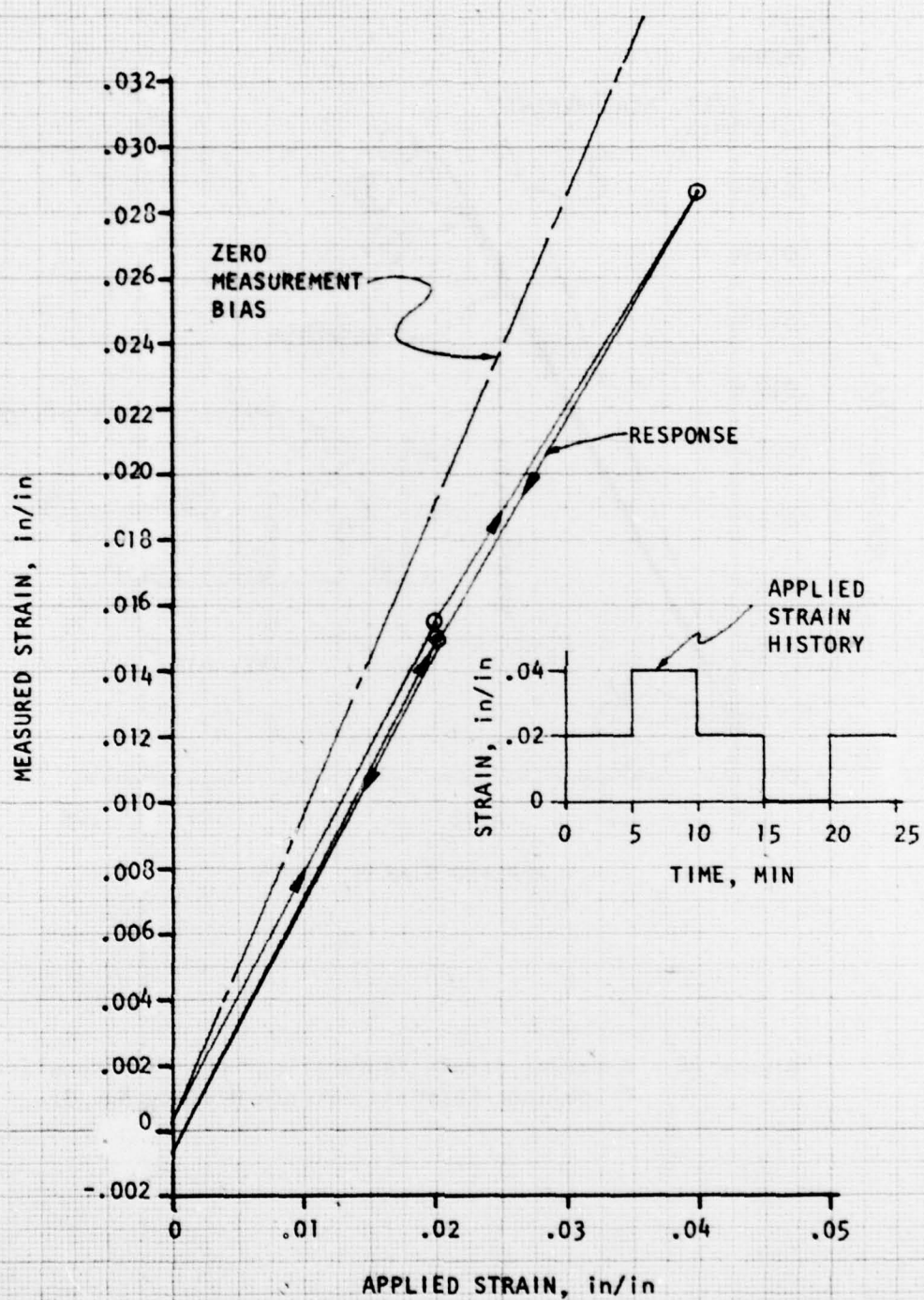Figure 46. Hysteresis Due to Viscoelastic Propellant Response
(Strain History No. 1)

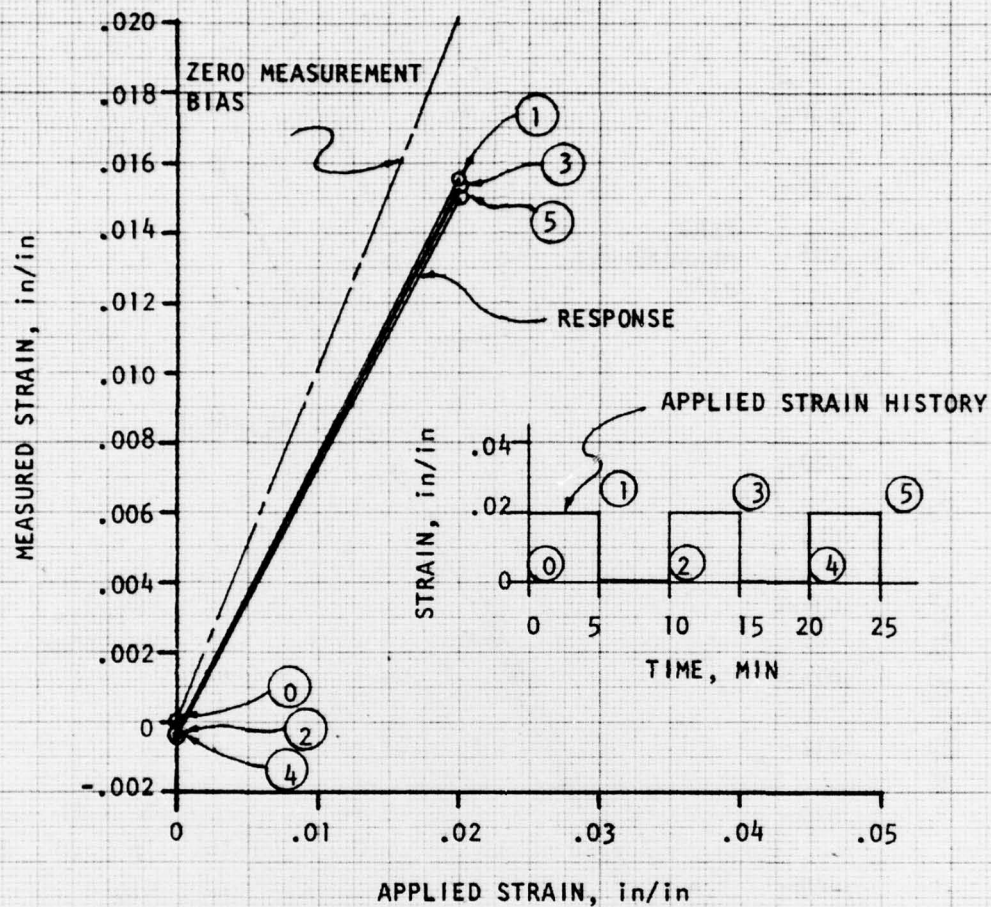Figure 47. Hysteresis Due to Viscoelastic Propellant Response (Strain History No. 2)

Figure 48. Apparent Strain "Ratcheting" Due to Viscoelastic Propellant Response (Strain History No. 3).

An even more interesting effect is seen in Figure 48. This is a strain "marching" or "ratcheting" effect, which closely resembles results obtained in certain instrumented motor tests (References 13 and 14). Whether the viscoelastic effects of gage/propellant interaction seen in Figure 48 has any bearing on the instrumented motor results, which were interpreted as real phenomena, is unkown. However, some investigation of this point may be worthwhile.

To investigate the effects of prestrain on gage measurement bias, the following scenario was utilized:

a. At time $t_1 - t_o$, a step prestrain (0.01 in/in was used in the analysis) is applied to the sample.

b. At time t_1^+, a step strain of magnitude $\Delta\varepsilon$ is applied in the same direction as the prestrain.

c. At time t (in the analysis, $t = t_1 + 5$), the strain sensed by the gage is recorded. The strain sensed by the gage at time t_1^- (i.e., just before application of the strain $\Delta\varepsilon$) is subtracted from the recorded value to obtain the measured strain corresponding to $\Delta\varepsilon$. For a linear viscoelastic sample material, this is entirely equivalent to the clip gage usage described in 3.5.1.

In order to carry out the calculations for prestrain times greater than 20 minutes, the time variable t in the calculator program described in 3.5.3 was replaced by $\theta = (t/n)$ which required that the value of A (see Equation (78)) be replaced by A + B Log n and that the time value output be multiplied by n.

-117-

The results of the prestrain analysis are shown in Figure 49. Evidently
a relaxation time of an hour or so is ample for all prestrain effects to
disappear in gage response at 5 minutes after loading. Calculations for
gage response at 0.1 minutes after loading show negligible prestrain
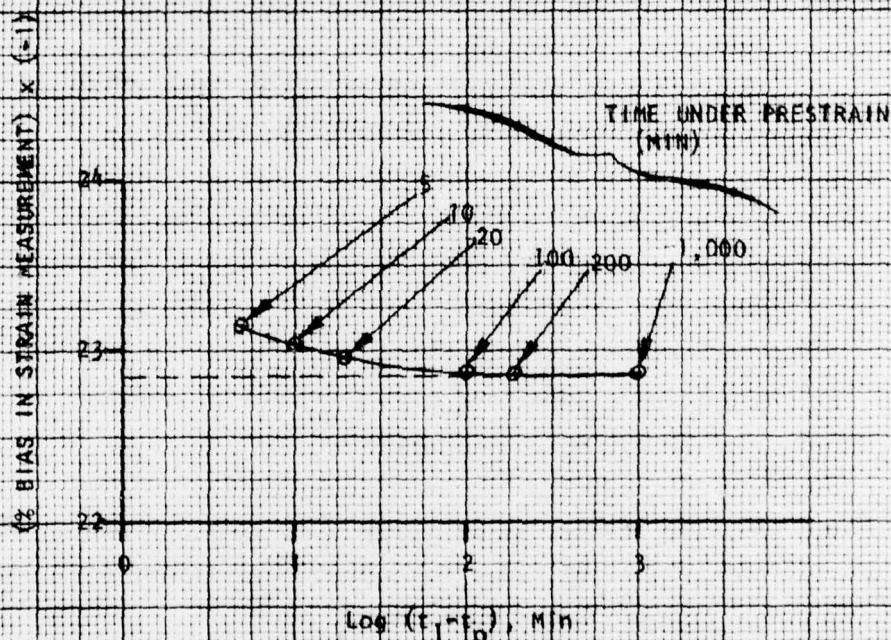effects even after only 5 minutes of relaxation.

Figure 49. Short Term Effects of Clip Gage Prestrain Due to Viscoelastic Propellant Response. (Prestrain Applied at Time t_j; Strain Applied at Time t_i; Data Acquired at Time τ; Calculations for Thiokol "Stiff-Leg" Gage With $e=.050$ in.)

4.   CONCLUSIONS AND RECOMMENDATIONS.

4.1   General Conclusions.

This report covers extensive analyses of the effects of gage/propellant
interaction on the accuracy of propellant strain measurement using clip
strain gages. The analyses directly address strain measurement on uniaxial
tensile specimens of a particular configuration used in the AFRPL/Thiokol
Improved Properties program. However, as discussed below, the conclusions
are true for other applications as well.

The following general conclusions are supported by the analysis results:

        a.   At least some state-of-the-art clip strain gages are too
                stiff for accurate measurement of solid propellant strain.
                The starting point of Thiokol's gage development efforts
                was a clip gage structure supplied by Konigsberg Instruments
                and originally intended for use on the AFRPL/Thiokol SALE
                program. This structure was stiff enough to introduce
                enormous measurement bias. Even Thiokol's best effort at
                producing a compliant gage induced a strain bias of more
                than 20 percent of the measured strain.

        b.   Drastic changes in clip gage materials and design could
                potentially eliminate or reduce measurement bias due to
                gage/propellant interaction.

        c.   The strain gage/propellant interaction problem can be
                analyzed with acceptable accuracy. The model used in the
                analyses in this report agrees extremely well with both
                3-D finite element analyses and with experimental measure-
                ments.

-120-

4.2   Impact on the Improved Properties Program.

As a result of early predictions of the analyses discussed in this report and Thiokol's confirming laboratory tests of gaged propellant samples, a decision was made to abandon clip strain gages as a measurement tool in that program. Alternate techniques were developed for measurements allowing the determination of propellant Poisson's ratio (these techniques are discussed in Reference 1).

4.3   Implications For Other Applications.

A careful examination of the considerations involved (see 3.2.4.4) in combining the bias due to local mounting pin deformation with that due to sample "beam deformation" leads to the (perhaps surprising) conclusion that the gage-propellant interaction effects are very nearly the same for a clip gage mounted on a semi-infinite slab as for a clip gage mounted on a uniaxial sample. This conclusion applies equally well to a clip gage mounted on the bore surface of an instrumented motor. It is clear, therefore, that action is needed to provide acceptable means of experimental propellant strain measurement.

4.4   Recommendations.

Experimental measurements of stress and strain are necessary for understanding of propellant mechanical behavior, both in simple laboratory samples and in actual rocket motors. The tools and techniques for making these measurements must be developed, or the lack of such aids will eventually become an obstacle to further improvements in theoretical modeling of propellant behavior as well as experimental investigation. Effort should continue to understand gage/propellant interaction for stress gages as well as strain gages. Emphasis on the development of more compliant strain gages for propellant is strongly recommended. Innovative approaches (such as the use of conductive polymers or gage structures fabricated from silicon with integral strain gages) should be considered along with more conventional approaches such as those discussed in 3.4.2.

It is also recommended, because of the excellent agreement with experimental results, that consideration be given to the use of the analysis techniques discussed in this report for correcting strain gage data for gage/propellant interaction effects. This would provide a short term substitute for the more desirable, long-term solution of developing "noninteracting" gages.

REFERENCES

1. Kruse, R. B., J. M. Nelson, and R. J. Vellacot, "Improved Solid Propellant Mechanical Properties Measurement for Structural Analysis Input, Interim Report - Phases I and II", AFRPL-TR-78-44, Thiokol Corporation/Huntsville Division, June 1978.

2. Roark, R. J., Formulas for Stress and Strain, 4th Ed., McGraw-Hill, 1965.

3. Briar, H. P., K. W. Bills, Jr., and R. A. Schapery, "Design and Test of the Operational In-Situ Gage for Solid Propellant Surveillance," AFRPL-TR-76-36, Aerojet Solid Propulsion Company/Texas A&M University, June 1976.

4. Timoshenko, S. P. and J. N. Goodier, Theory of Elasticity, 3rd Ed., McGraw-Hill, 1970.

5. Den Hartog, J., Advanced Strength of Materials, McGraw-Hill, 1952.

6. R & D Contract Status Report, AFRPL Contract F04611-76-C-0041, Thiokol Corporation/Huntsville Division, May 1977.

7. Personal Communication From J. Nelson, Thiokol.

8. R&D Contract Status Report, AFRPL Contract F04611-76-C-0041, Thiokol Corporation/Huntsville Division, April 1976.

9. R&D Contract Status Report, AFRPL Contract F04611-76-C-0041, Thiokol Corporation/Huntsville Division, June 1976.

10. Hoyt, S. L., Metal Data, Reinhold Publishing Corporation, 1952.

11. R&D Contract Status Report, Contract F04611-76-C-0041, Thiokol Corporation/Huntsville Division, February 1977.

12. R&D Contract Status Report, Contract F04611-76-C-0041, Thiokol Corporation/Huntsville Division, September 1977.

13. Burton, J. D., and W. H. Miller, "Minuteman STV Data Reduction," AFRPL-TR-73-113, Rockwell International Corporation/Rocketdyne Division, February 1974.

14. Burton, J. D., W. H. Miller, and J. L. Trout, "ALIVE Instrumented Motors Status Report," JANNAF Operational Serviceability and Structures and Mechanical Behavior Working Groups Combined Annual Meeting, CPIA Pub No. 264, May 1975.